Project No. 09-810

Experimental Study and Computational Simulations of Key Pebble Bed Thermo-mechanics Issues for Design and Safety

Reactor Concepts R&D

Dr. Akira Tokuhiro
University of Idaho

In collaboration with:
Idaho National Laboratory

Madeline Feltus, Federal POC
Josh Cogliati, Technical POC

NEUP Nuclear Energy University Programs
U.S. Department of Energy

Nuclear Energy University Programs (NEUP)

Final Report on

Experimental Study and Computational Simulations of Key Pebble Bed Thermo-mechanics Issues for Design and Safety

Project Number: 09-151(810)
Initiative: Gen IV

November 2013

Report Prepared by: Akira Tokuhiro[a] Mie Hiruta[a]

PIs: Akira Tokuhiro[a], Karl Rink[a], Gabriel P. Potirniche[a],
Joshua J. Cogliati[b], Abderrafi M. Ougouag[b]

Student Investigators: Mie Hiruta (M.S.) [a], Maziar Rostamian (Ph.D.)[a],
Gannon Johnson (M.S.)[a], Branden Poulsen (Ph.D.)[b]

[a] Department of Mechanical Engineering, University of Idaho
[b] Idaho National Laboratory

Abstract

An experimental and computational study, consisting of modeling and simulation (M&S), of key thermal-mechanical issues affecting the design and safety of pebble-bed (PB) reactors was conducted. The objective was to broaden understanding and experimentally validate thermal-mechanic phenomena of nuclear grade graphite, specifically, spheres in frictional contact as anticipated in the bed under reactor relevant pressures and temperatures. The contact generates graphite dust particulates that can subsequently be transported into the flowing gaseous coolant. Under postulated depressurization transients and with the potential for leaked fission products to be adsorbed onto graphite 'dust', there is the potential for fission products to escape from the primary volume. This is a design safety concern. Furthermore, earlier safety assessment identified the distinct possibility for the dispersed dust to combust in contact with air if sufficient conditions are met. Both of these phenomena were noted as important to design review and containing uncertainty to warrant study. The team designed and conducted two separate effects tests to study and benchmark the potential dust-generation rate, as well as study the conditions under which a dust explosion may occur in a standardized, instrumented explosion chamber. The project was awarded, August 2009, started several months later and concluded September 2013, with a one-year no cost extension.

A separate effects experimental rig to investigate the frictional wear and nuclear grade graphite dust generation rate was specifically designed and constructed to operate up to PBR relevant conditions in temperature (up to 750°C) and pressure (up to 7 MPa helium). The designed apparatus performed well and generated reliable data. In addition, the estimated experimental measurement uncertainty was considered to be acceptable relative to the measured dust masses generated.

The results of 'wear tests' revealed two wear modes here defined in terms of the environmental temperature and pressure under which the graphite spheres were tested. Under higher temperatures (200°~750°C) and higher helium pressures (1~6.5MPa) we observed and quantified "large wear" with wear rate, on average of 1.37×10^{-5}g/Nm. In contrast, "lubricated wear" occurred close to room (lower) temperature, under 1 to 3 MPa of helium pressure; that is, generating an average wear rate of 1.97×10^{-7}g/Nm. Using Scanning Electron Microscope (SEM) images and X-ray diffraction (XRD) analysis of pre- and post-test graphite samples supported plausible wear mechanism contributing to the graphite dust collected. First, SEM images depicting a "flattened" and optically reflective surface corresponding to "lubricated wear" supported the smaller mass collected. The "large wear", on the other hand, revealed a degraded surface due to different frictional forces under higher temperature and pressure. Post-test XRD analysis showed that the graphite lost its three-dimensional graphitized crystalline structure, relative to the pre-test sample that maintained a well-graphitized crystalline structure. The is significant because these wear modes occur under anticipated PBR thermal hydraulic conditions. One can thus expect crystalline structure changes of graphite. However, both modes showed small masses of dust generated.

The computational modeling and simulations of the graphite surface contact mechanics, as anticipated in a PBR configuration, was carried out in order to understand the dust generation mechanism and to validate test results as practical. A methodology that encompasses finite element analysis (FEA) and micromechanics of wear was developed to address the frictional wear. In particular, the wear phenomena and change in the rate of dust generated with sliding contact length was determined. This effort was led by Rostamian with expertise on various aspects contributed by Cogliati, Ougouag and Potirniche.

This computational modeling consisted of two perspectives and approaches due to restricted computational resources. The two methods, a macroscale stress analysis and a microscale analysis of wear mechanisms, considered the phenomena at two different scales. First a set of FEA simulations considering pebble-pebble frictional contact was studies. In these simulations, the mass of generated graphite particulates due to frictional contact was calculated by incorporating FEA results into Archard's equation, which is a linear correlation between wear mass and wear length. However, our test data revealed that the wear rate of graphite decreased with sliding length. This is because the surfaces of the graphite pebbles become smoother over time, which results in a gradual decrease frictional contact and thus, the wear rate. In order to address the change in wear rate, a more detailed analysis of wear mechanisms at room temperature was developed. In this microscale study, the wear behavior of graphite at the asperity level is studied by simulating the contact between asperities of facing surfaces. By introducing the effect of asperity removal on wear rate, a nonlinear wear rate is obtained. A nonlinear wear law was thus proposed as a model to predict the effect of changing surface topology on the wear of graphite. This tribological model was validated using test data and noted as suitable where mass removal is in the form of powder formation rather than flake or chip formation.

Separate effect dust explosion tests using a custom-designed and constructed combustion chamber were performed by Poulsen and Rink. Experiments revealed that the smallest amount of graphite dust mass that can lead to explosions is three orders of magnitudes larger than the maximum amount predicted to be generated in the present work. This was based on the predicted pressures produced during the discharge of burning pyrotechnic into inert gas; subsequently used to predict the minimum explosible amount of graphite dust in an air ingress accident scenario. Therefore, it was concluded that pebble-pebble frictional contact is not a significant (enough) source of dust generation such that a subsequent explosion hazard under exposure to air/oxygen is a major safety concern. However, as there is no reliable benchmark data on the accumulated dust mass with continuing operation of the PBR, the mass accumulated has to be monitored and verified with current estimates. Finally, during the course of this project, a consensus expert opinion that 'baking' of the dust onto surfaces would also reduce the dust circulated in the primary circuit.

Technical Tasks per Awarded Proposal
Summary of Completed Work

Per the NEUP awarded proposal in 2009, the team proposed both experimental and computational scope of work investigating graphite dust generation and combustion issues of safety relevance of the graphite-moderated, gas-cooled pebble bed reactor. The SOW's objective was to broaden understanding and experimentally validate the thermal-mechanic frictional wear phenomena of nuclear grade graphite, specifically, spheres in frictional contact as anticipated in the bed under gradual movement at PBR relevant pressures and temperatures (~7MPa, 750°C). As anticipated, frictional contact generates graphite dust particulates that can subsequently be transported into the flowing gaseous coolant. Under postulated depressurization transients and with the potential for leaked fission products to be adsorbed onto graphite 'dust', there is the potential for fission products to escape from the primary volume to the containment space. Furthermore, there is the distinct possibility for the dispersed dust to combust if sufficient conditions are met.

The project consists of the following **Tasks:**

Task 1. Design and construct smaller-scale separate effects test experiments to benchmark the thermal-mechanics of dust generation and to also study the potential for dust explosion. The team will conduct tests to simulate dust generation, entrainment, and transport and will analyze how much dust is generated by a PB reactor.
Accomplishments. Based on a literature review on graphite wear studies, and communication with the INL co-PIs, we designed and constructed an experimental apparatus wherein the thermal and pressure boundaries were separate. The thermal boundary was localized inside a larger pressure boundary. After shakedown testing, experiments using nuclear grade graphite in frictional contact were carried out. We further determined that the results were reproducible. Details on the design, construction and initial experiments are contained in the following.

- Johnson, G., Rostamian, M., Rink, K., Cogliati, J., Ougouag, A., Tokuhiro, A.,"*Experimental study and computational simulations of key pebble bed reactor thermomechanics issues for design and safety*", poster presentation by Johnson at the VHTR Technology Development Office, 4th Annual Technical Review Meeting 2011, Albuquerque, NM, May 2011.
- Johnson, G., *Experimental study of nuclear graphite and graphite-steel wear in spherical frictional contact under gas-cooled reactor pressures and temperatures*, Master's Thesis, University of Idaho, 2012.

Task 2. Conduct experiments with custom-designed apparatus under GC-GCR relevant conditions. In order to preserve the experimental apparatus, experiments we conduct from lower to higher temperature and pressures in phases. While most of the tests were done using Toyo Tanso's IG-11 samples (provide), graphite spheres provided by SGL and graphite-steel tests were also conducted. Interactions with modeling and simulations (M&S) were also maintained. The accomplishments are noted below.
Accomplishments. Experiments and pre- and post-test SEM and XRD analyses of graphite samples, as well as M&S of the thermal-mechanics were done. In summary, the frictional wear can be classified into two named wear modes. With temperature or (helium) pressure at ambient or one slightly higher than ambient, the wear test resulted "lubricated friction". This was previously reported by other

investigators. The surface appearance is 'polished, reflective (shiny)'. As temperature or helium pressure becomes higher, the wear test indicated "large wear" with larger amount of graphite dust generated from frictional contact. However, both modes yielded dust generations, though in good agreement with that by Luo and Stansbury, much smaller that the only other reference, that attributed to AVR.
The transition temperature and helium pressure between these modes was determined to be 20° to 200°C and 0.1MPa to 1MPa, respectively. SEM and XRD analyses also supported identification of these two modes. In fact, SEM images and XRD analysis revealed that the crystalline structure on the wear surface changed as a result of the wear test. Both frictional movement and testing condition contributed to the change between "lubricated friction" and "large wear". Further details are noted in the following.

- Hiruta, M., *Experimental study of dust generation from nuclear grade graphite spheres in frictional contact under a pressurized inert atmosphere at elevated temperatures*, Master's Thesis, University of Idaho, 2013.
- Hiruta, M., Rostamian, M., Johnson, G., Tokuhiro, A.,"*Experimental study of graphite dust generation under VHTR/PBR conditions"*, poster presentation by Hiruta at the VHTR Technology Development Office 6th Annual Technical Review Meeting 2013, Idaho Falls, ID, May 7-9, 2013
- Rostamian, M., Johnson, G. , Hiruta, M., Potirniche, G. P., Cogliati, J.J., Ougouag, A.M., Tokuhiro, A., *Computational and experimental prediction of dust production in pebble bed reactors, Part I* Nuclear Engineering and Design, Volume 263, Oct. 2013, 500-508.
- Hiruta, M., Rostamian, M., Johnson, G. , Potirniche, G. P., Ougouag, A.M., Bertino, M., Franzel, L., Tokuhiro, A., *Computational and experimental prediction of dust production in pebble bed reactors, Part II* Nuclear Engineering and Design, Volume 263, Oct. 2013, 509-514.

Task 3. Develop a model of the frictional contact wear phenomena and run simulations such that the dust generation rate is estimated and compared to experiments per above Tasks.
Accomplishments. A coarser mesh finite element analysis (FEA) model and a finer mesh micromechanics model were developed to study the dust generation phenomena of two graphite surfaces in frictional contact. In particular, the phenomenon of wear and a change in the rate of dust generation with relative sliding length (of the contact point(s) was investigated. Due to restrictions on access to computing resources[1], all work was done on conventional desktop PCs.
Of the limited literature in this area, a simple linear wear mode; called the Archard Wear Model served as a reference. In this model, the wear volume is related to the material properties and the sliding distance of two materials in frictional contact. By performing FEA analysis (ABAQUS) at a macro-level, the normal forces on wear were determined over a short sliding distance, for brittle materials. In order to account for the nonlinear wear rates of the material FEA analysis considered the near-surface micromechanics, where asperities or surface 'roughness' serve as contact points. Primarily, 3D spherical asperities were considered to be modeled using the implicit module. "ABAQUS Explicit" was used to model the asperities in contact and revealed that asperities undergo very high deformations. In fact, as the material reaches a total strain of 0.05, the elements are removed from the surface. The material removed was then used to estimate the dust generation rate.

The wear coefficient obtained from the reference, non-linear Archard Model was compared to the experimental results. Except for recognized accumulation of dislodged particulates that were not modeled, the non-linear model predicted the dust generation rate in a satisfactory manner. The

[1] As Maziar Rostamian was considered a foreign national from a sensitive country, access to high performance computing was not provided by the local FFRDC.

generation rate is at least two orders of magnitude less than the estimated mass concentration needed for combustion. Further details are contained in the following.

- Rostamian, M., *Computational prediction of dust production in graphite moderated PBR*, Ph.D. Thesis, University of Idaho, 2012.
- Rostamian, M., Arifeen Sh., Potirniche P. G., Tokuhiro A*., Initial Analysis of Pebble Contact in Pebble Bed Reactors*, Transactions of the American Nuclear Society, 2010, 103 1028-1031.
- Rostamian, M., Arifeen Sh., Potirniche P. G., Tokuhiro A., *Initial prediction of dust production in pebble bed reactors*, Journal of Mechanical Sciences, 2011, 2 189-195.
- Rostamian, M., Potirniche P. G., Cogliati J. J., Ougouag A. M., Tokuhiro A., *Computational prediction of dust production in pebble bed reactors*, Nuclear Engineering and Design, Volume 243, 2012, 33-40.
- Rostamian, M., Johnson, G. , Hiruta, M., Potirniche, G. P., Cogliati, J.J., Ougouag, A.M., Tokuhiro, A., *Computational and experimental prediction of dust production in pebble bed reactors, Part I* Nuclear Engineering and Design, Volume 263, Oct. 2013, 500-508.
- Hiruta, M., Rostamian, M., Johnson, G. , Potirniche, G. P., Ougouag, A.M., Bertino, M., Franzel,L., Tokuhiro, A., *Computational and experimental prediction of dust production in pebble bed reactors, Part II* Nuclear Engineering and Design, Volume 263, Oct. 2013, 509-514.

Task 4. Develop a model and conduct experiments to study the energy transfer mechanism from the burning (combusting) pyrotechnic to the surrounding gas to predict the minimum amount of graphite dust which can cause combustion in a gas-cooled reactor during a depressurization accident.
Accomplishments. Both experimental work and computational simulations were carried out under this Task. In order for graphite dust combustion to take place the literature reports that five to six conditions have to be met. One of the conditions is the combustant density or mass concentration [kg/m^3]. Based on this Task and experiments, a higher concentration of graphite dust is needed than that generated from the above Tasks. Furthermore, discharge of the combusting pyrotechnic without diffusing the thermal condition must be maintained. The task introduces a semi-empirical model capable of predicting the transient pressure produced during the discharge of burning pyrotechnic into inert gas. The conditions are not favorable for dust combustion. Further details are contained in the following.

- Poulsen, B., *Prediction of isochoric inert and reactive gas behavior during pyrotechnic initiator actuation*, Ph.D. Thesis, Moscow, ID, University of Idaho, 2011.
- Poulsen, B. L., Rink, K.K., *Modeling the energy release characteristics of ZPP based initiators*, Presented by Poulsen, 49th AIAA Aerospace Sciences Meeting Including the New Horizons Forum and Aerospace Exposition, Orland, FL, Jan 4-7, 2010.
- Poulsen, B. L., Rink, K.K., *Modeling the energy release characteristics of THPP based initiators*, Presented by Poulsen46th AIAA /ASME/SAE/ASEE Joint Propulsion Conference and Exhibit, Nashville, TN, July 25-28, 2010.

Table of Content

1. Introduction

The pebble bed reactor (PBR) is a graphite-moderated, high-temperature gas-cooled reactor (HTGR). As the PBR features a unique online refueling capability, the PBR reduces shut-down time and facilitates operational efficiency. Thus the bed slowly moves relative to the pressure vessel. The bed is thus comprised of thousands of billiard-sized graphite-matrix spheres (~6cm DIA) as fuel elements. Each pebble contains the tristructual-isotropic (TRISO) nuclear fuel particles. Both fresh and assayed pebbles are inserted at the top of the RPV and gradually traverse to the bottom of the reactor where they are extracted. They are exposed to pressurized helium coolant at temperatures ranging from 650°C to 950°C. As the pebbles traverses, graphite dust is generated from frictional wear and thus dust is circulated and a candidate for release under a postulated depressurization and subsequent air ingress accidents. If the dust is laden with fission products from fuel failure and/or the dust is under high concentration [mass/unit volume], combustion thereof is a design safety issue. Powers (XXXX) ranked this and other safety issues of the PBR. Graphite dust generation and transport was indeed identified as a safety concern under the German AVR project (Moorman, 2009). However, the phenomenon of dust generation was never closely examined experimentally and computationally. We thus proposed this as part of the current scope of work.

Thus per the awarded proposal (2009), Task 1 was to design and construct an experimental apparatus to investigate the frictional wear generated nuclear grade graphite 'dust'. Following, Task 2 was to conduct experiments to measure the dust generation rate and to estimate the kinetic friction at PBR relevant temperatures and pressures. Task 3 consisted of computational modeling and simulations (M&S) of the thermal-mechanics of graphite dust generation at room temperature were also done. Due to limited computational resources, we took both a 'macro-' and 'micro-mechanic' approach to frictional wear of graphite and introduced a nonlinear wear model for graphite (Rostamian, 2012). Results of our M&S showed good agreement as compared to that reported by Luo (2005) and Cogliati (2011). This model's empirical constants were determined from experimental data; it subsequently predicted results in satisfactory manner. Since high temperature properties of graphite other than its module of elasticity, are not available, high temperature M&S were not conducted. However, given these and related properties, simulations can be done at higher temperatures. Finally, Task 4 was to evaluate the thermal-chemical conditions required for graphite dust to explode/combust as postulated under the depressurization and air-ingress accident scenario wherein graphite dust and fission products could escape out of the RPV.

This report provides details of the design and construction of experiments, as well as the experiments performed to assess the dust generation rate of nuclear grade graphite in frictional contact. The report also describes the modeling and simulation work on the frictional contact mechanics.

2. Design and Construction of Experimental Apparatus

This chapter describes the design and construction tasks of the experimental apparatus intended to study the frictional contact wear and thus the graphite dust generation. Details on the combustion experiment is contained in Chapter 5.

The pebble bed reactor uses a nuclear fuel encased in a random configuration of (smaller) spherical fuel particles. The fuel sits in a 'pebble bed' inside a cylindrical vessel with graphite spheres that serve as the moderator. The coolant (helium) flows through the bed. In this configuration, the reactor is not only capable of online refueling (thus reducing outage time, boosting operational efficiency) but can operate at high output temperatures so that both electricity and process heat can be provided. However, this unconventional, 'moving bed' core design creates specific modeling and design challenges in terms of safety in design review and licensing. Also to offer additional economic competitiveness, PBRs are intended to be placed in a (air-filled) confinement building, not containment buildings. Thus reactor vessel integrity during postulated accidents is of paramount importance. In fact, as small probability (~$1X10^{-6}$ or less) of a fuel failure is taken into a design basis accident (DBA) , the possibility of fission product laden graphite dust particles is a possibility. During a depressurization DBA and subsequent air ingress progression, Powers (200X) noted the possibility of graphite dust combustion (within the air-filled confinement) that would exacerbate the accident. Thus the thermal-mechanics of the moving bed, especially the frictional contact wear and graphite dust generation was identified as needing further study. Besides the bed itself, dust can also be generated via graphite-steel contact within the reactor's fuel handling system. The range of relevant phenomena must be studied at reactor relevant conditions – foremost temperature and pressure (~up to 750°C, 7MPa)

This chapter contains details of the design and construction of the experimental rig, shakedown testing, benchmarking of the apparatus against past published data, and initial results from the intended testing matrix. Further details are provided in the theses by Johnson and Hiruta.

2.1 Literature reviewing for graphite wear test

2.1.1 Experimental Graphite Wear Rate

Since nuclear grade graphite material has specific performance requirements, there is limited accessible tribological data on them relative to non-nuclear grades. However, there is accessible data for (non-nuclear grade) graphite tribology. Since it is difficult to conduct experiments while a graphite-moderated gas-cooled reactor is operating, data gathered through graphite tribological studies on similar types of graphite using various test conditions was examined.

Recent studies of graphite wear are mostly published by researchers at Tsinghua University in Beijing. These include studies on the wear rates of graphite matrix on alumina and Toyo Tanso's IG-11 graphite. They note that the wear rate of graphite can vary by four orders of magnitude depending on the materials used and the experimental conditions. This suggests that graphite wear changes in time and both the initial and ongoing environmental conditions.

The tribological data to date is insufficient to provide definitive characterization of nuclear graphite under reactor condition. Previous graphite wear studies conducted on non-nuclear grade graphite investigated the effect of the graphite wear phenomena with respect to mechanical tools and casings made of steel or other metals. As well, previous wear studies using older nuclear grade graphite such as ATJ, PGX, H-204, and H-359, have been used for comparison with the non-nuclear graphite studies that focused on the wear phenomenon against steel. The most recent study of nuclear grade graphite wear was conducted using IG-11 are those reported by Sheng (2003) and Luo (2005).

2.1.2 Graphite Wear Parameters

There is no consensus in the tribological community on all the parameters that affect the wear rate in tribology. Therefore, the effective parameters which we experimentally considered were the following parameters: temperature, cover gas, sliding speed and distance, and surface roughness as documented. While we acknowledge other parameters such as gas adsorption, we did not have a means to measure this in-situ. Further, some surface phenomena such as adsorption have been studied previously.

Several different studies have shown the effect of temperature on graphite wear. However, owing to other influencing factors, there is no clear trend with temperature in general. A recent study by Luo (2005) showed an increase in graphite wear with temperature. Their work suggested a combination of abrasive, adhesive and fatigue wear at different temperatures.

2.1.3 Wear Measurement Techniques

Most of the previous studies surveyed used idealized conditions removed from the operational conditions of the PBR. However, as data under relevant conditions is lacking we considered for example the work of Luo (2005) as a point of reference. In considering frictional contact wear, the basic relative motion of surfaces can be considered as follows: relative sliding, sliding and rotation, or co-rotation in uni-directionally and in counter-rotation. Here, as the PBR consist of a moving pebble bed, there is dynamic frictional contact at multiple contact points for a given sphere. This contact can be with both stationary spheres, co-moving spheres or against the (stationary) vessel surface. We thus designed a graphite wear experiment to study the graphite-graphite and graphite-steel relative motion and thus frictional contact wear.

2.2 Design Requirements and final design

The ability to perform both separate effects frictional wear rate tests as close as possible to the thermal-hydraulic conditions in the PBR was considered important. Thus at the onset, after review of the literature and consultation with the INL co-PIs, the target test parameters shown in Table 2-1 were selected.

Table 2-1. Design Parameters for Testing Apparatus.

Testing Parameter	Description	Source
Maximum Temperature	700 - 900°C	Reactor Outlet Temperature (INL/EXT-11-23008)
Maximum Pressure	7-9.1 MPa	Primary Loop Pressure (INL/EXT-11-23008)
Helium Environment	99.998%	HTGR standards (Li and Sheehan, 1981), Airgas Catalog
Normal Force	10-50N	Past Chinese Studies (Luo et al., 2004)
Velocity	<0.1 m/s	Cogliati, 2011
Total Distance	~500 m	Luo et al, 2005; Kadak, 2004
Contact Geometry	Sphere-Sphere Sphere-Plane	pebble-pebble contact and pebble-reflector
Number of contacts	1	Data needed for PEBBLE code to predict core dust generation
Relative motion desired	Rolling, Sliding, spinning	Data needed for PEBBLE code to predict core dust generation

One of the important parameters was the purity of helium gas as it is likely that gas atoms/molecules adsorb onto the graphite surface. . The maximum pressure selected was 1000 psi,

since this was very close to 7 MPa (1015 psi) and it was a standard value used for “commercial-off-the-shelf” (COTS) relief valves and pressure fittings. The helium environment purity was taken as 99.998% in an attempt to balance the purity versus the cost of the gas.

The simultaneous design objective to have both high temperature and environmental pressure are atypical in the ‘tribometer’ literature. However, we realized both in an unique way as follows. We employed a pressure vessel ASME-certified to high pressure; that is up to about 9 MPs. We then inserted a tribometer with the vessel and locally heated the graphite samples to temperature. By hosting the tribometer inside the pressure vessel, we could measure in real time the particulate mass generated as well as the normal force applied by the graphite samples, with only non-mechanically actuated penetrations through the pressure boundary. In fact, modular analytical balance stayed relative cool, as it was outside the local, heated zone. The conceptual design is shown in Figure 2-1. Note that the frame of the tribometer was mounted to the underside of a pressure vessel’s top flange. This frame was divided into three sections: the top tribometer section housing the electrical motors and instrumentation, the middle furnace section where the samples are held, and the bottom section for the mass measurement sub-system (Figure 2-2).

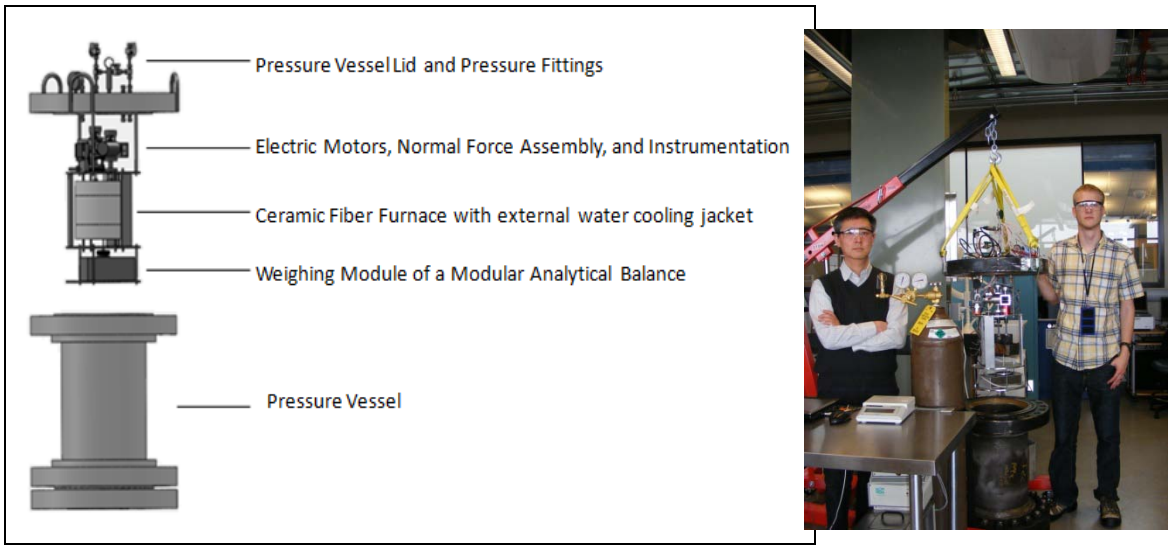

Figure 2-1. Tribometer Final Design for Major Components.

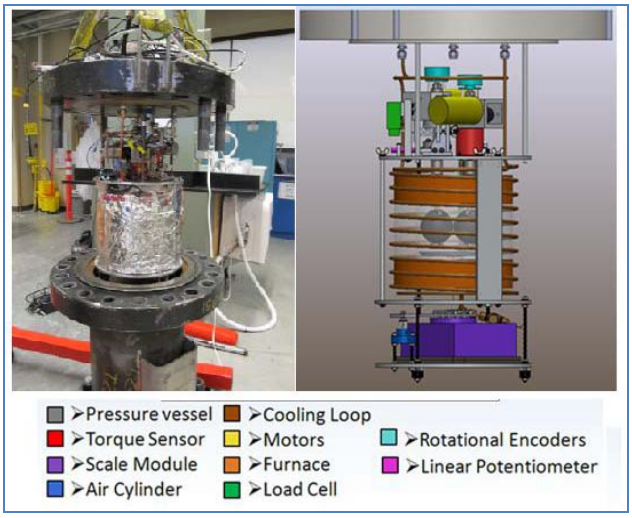

Motors, instruments

Samples, Furnace,

Mass measurement

Figure 2-2. Layout of Testing Apparatus.

2.2.1 Sample Geometry

The basic sample designs created for the testing of the apparatus for this task were as follows:

a. Graphite Disks: Machined into 2.54 cm tall disks with a 6 cm outer contour (same as the sphere).
b. Graphite Spheres: SGL machined spheres, with machines holes for mounting (6 cm outer contour).
c. Steel Cylinder: Smooth, turned 304 Stainless Steel cylinder to allow steel rotation (2.54 cm tall, 6 cm outer contour).

Having these multiple sample geometries and samples allowed for the testing of the following frictional contact configuration anticipated in the PBR: pebble to pebble as in the bed, pebble to reflector or vessel and finally pebble to fuel transfer vertical pipe contact. The basic test was conducted with sample geometry shown in Figure. 2-3. This was to simulate one point of frictional contact within the PBR core bed.

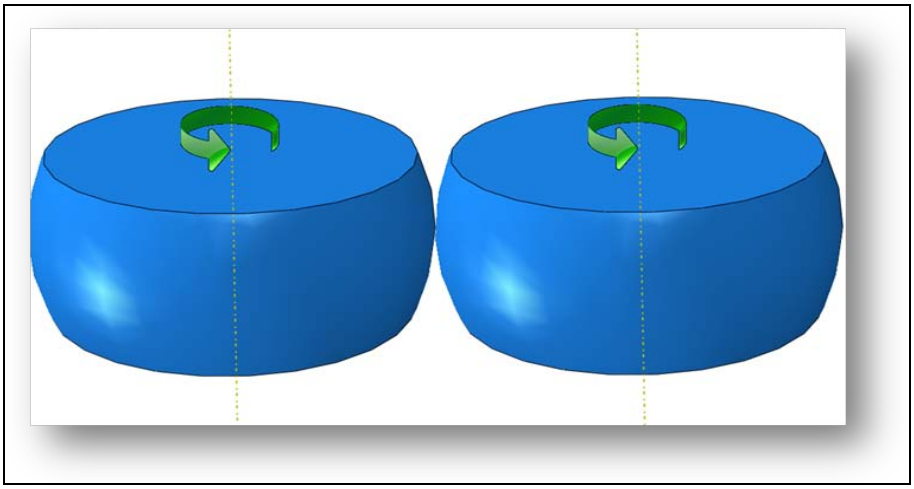

Figure 2-3. Sample Geometry and Orientation in the Tribometer (geometry a).

2.3 Materials Tested

There are four different graphite manufacturers approved by NGNP. These suppliers provided graphite for this study upon request. This project received and we acknowledge support from Toyo Tanso U.S.A., SGL, and Graphtek. Most of the tests done here used Toyo Tanso's IG-11, although SGL's MRLF-1 was also tested under limited, similar conditions. Comparisons of the material properties of these graphite are in Table 2-2.

Table 2-2. Material properties of graphite.

	IG-11	**MRLF-1**	**GR001CC**
	Toyo Tanso	**SGL**	**Graphtek**
Density (g/cm^3)	1.77	1.73	1.81
Typical Grain Size (μm)	Fine, 20	Medium, 96% <1000	Fine*
Porosity (%)	18	23	12
Shore Hardness	51	-	76

*typical grain size not available

2.4 Testing Matrix

The testing conditions and thus the test matrix were determined to minimize duty at higher temperatures. In other words, the vessel was ASME certified for higher pressure but with a temperature limit. Thus water-cooling on the outside of the heater reduced heat-up of the vessel. The highest temperature runs were strategically run after all other data runs were completed. The initial testing phase was conducted on iso-molded fine grained graphite, since this was the predominant graphite grade noted in the literature. The initial tests demonstrated the reliability of the experimental apparatus and the measurement method. Air tests at room temperature were treated as a shakedown and to help provide a base line for the main tests with helium.

Thus three different type of tests were conducted for his study, as follows: 1) test with SG-11 graphite, 2) SG-11 graphite-on-steel test, and 3) test with SGL MLRF graphite. The tests were conducted under a helium atmosphere. The testing matrix with the initial test conditions is shown in Table 2-3.

Table 2-3. Experimental Testing Matrix with Contact Force.

(1)Helium Test

Temp./Pressure	101 kPa	1 MPa	3.0 MPa	6.5 MPa
20°C		20N (2)	20N (1)	20N (1)
200°C	20N (1)	20N (3), 30N (1)	20N (2)	20N (2)
400°C	20N (1)	20N (2)		20N (1)
600°C		20N (1)		
750°C		20N (1)		

(2)Graphite-on-Steel Test

Temp./Pressure	1MPa
20°C	20N (1)
200°C	20N (1)

(3)MLRF Test

Temp./Pressure	1MPa
20°C	20N (1)
200°C	20N (1)

All the tests had a constant velocity of 0.04 m/s

(-) Number of competed tests

The largest fraction of the helium test were done using IG-11 [“(1)”above]. Other than preconditioning of the graphite samples by degassing, temperature and pressure conditions were the main parameters. The graphite-on-steel tests, “(2)” above were conducted ton compare and contrast with respect to the IG-11 tests. As noted, the graphite-on-steel test is mimics the anticipated frictional contact per fuel recirculation of the PBR core. Finally, the SGL MLRF tests, “(3)”, further compared and contrasted the IG-11 tests. Both the graphite-on-steel test and SGL MLRF test were conducted for two test conditions relative the IG-11 based reference.

2.5 Calculation of Distance, Wear Rate and Friction

In many of the previous investigations, wear and friction experiments on graphite used controlled motion of one sample against a stationary sample. When calculating the wear rate of both rotating samples, relative displacement was used. Since the apparatus here allowed both samples to rotate under varying directions, relative motion was used to calculate the wear rate. The relative distance the contact surface traversed was calculated using Equation (1).

$$D = \sum_{i=1}^{n} \frac{2\pi r}{2500} (|V1_n + V2_n|) \times t \qquad \text{Equation (1)}$$

Where:

D	Wear distance per testing segment (m)
V_1	Encoder 1 output (Hz, CW +)
V_2	Encoder 2 output (Hz, CW +)
r	nominal radius of the sample (3cm)
t	Sampling time (s)
i	Data sample
n	Total data samples per testing segment

Using this distance, the wear rate was calculated below,

$$K = \frac{W}{F_N \cdot D} \qquad \text{Equation (2)}$$

where,

K	Wear rate (g/Nm)
W	Wear mass (g)
F_N	Normal Force Applied to Sample (N)

Also, kinetic friction coefficient was calculated with reaction torque;

$$\mu_f = \frac{F_k}{F_N} = \frac{T_r}{r \cdot F_N} \qquad \text{Equation (3)}$$

Where:

μ_f	Sample friction coefficient (-)
F_k	Friction Force (N)
Tr	Reaction Torque (N-cm)

The testing segments were defined as the timed runs in between mass measurements; the motors were stopped during these measurements. The sum of the distances covered in these test segments yielded the total distance that each sample traversed in frictional contact. When calculating the total wear rate, the sum total relative contact distances corresponded to the mass collected jointly. The distance was calculated using Matlab with an 'M-file'.

The data extracted from the test was automatically stored through I/O-Tech Personal Daq56 into M-file. Each test run consisted of 1000m contact length; this corresponded to about 125,000 data points. The generated mass was from periodical mass measurement. An example of collected mass data and the data extracted from the test can be seen below.

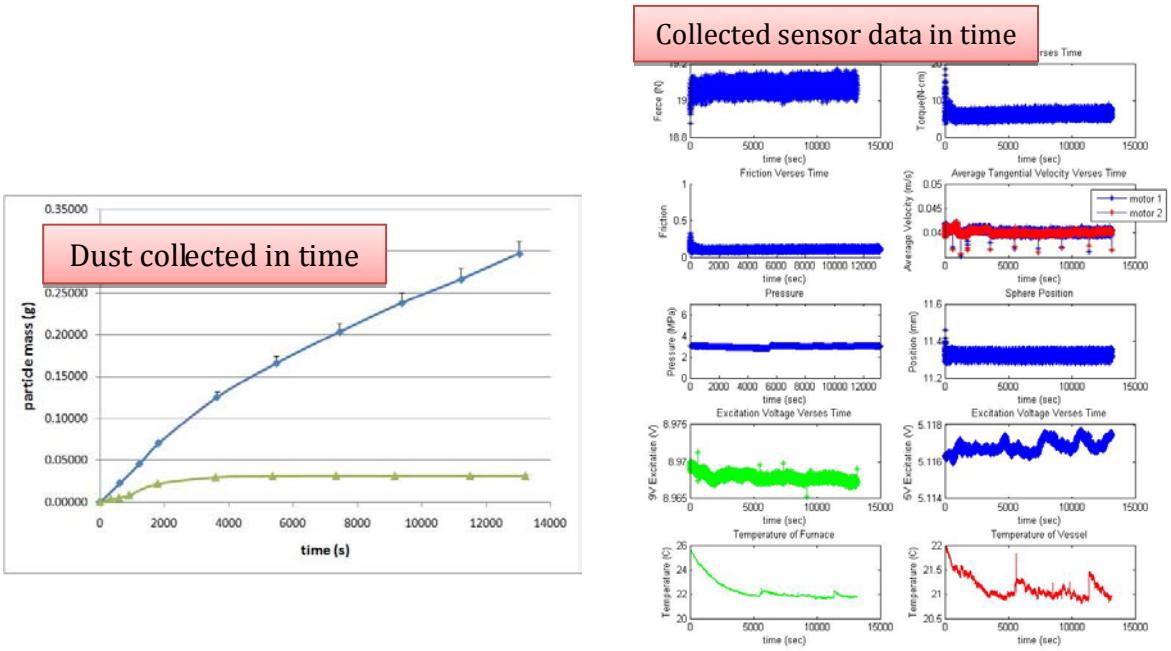

Figure 2-4. Example of Data Collected from the Test.

2.6 Apparatus shakedown overview

Shakedown tests were conduct to develop, practice and plan the experiments, as well as confirm the function of all components, hardware and software. This section summarizes the shakedown testing, the dry test runs, uncertainty quantification on mass measurement, and procedures developed during the shakedown.

The first shakedown test used wooden spheres (~6cm DIA), coated with sand using Krylon Spray adhesive. The goal of the test was to verify function of the motion control system, application of the normal load between spheres, and to test the particulate mass measurement technique. The spheres were 6.35cm in diameter and had a 3/8’ hole drilled through the center and slots on the top to mimic the actual spherical sample design. The Krylon spray was applied to the sphere at a distance of 10-12 inches in one even coat, and then rolled twice in a container of commercial, coarse un-sifted black sand obtained from a hobby store. The results of the testing using two normal forces are shown in Figure 2-5.

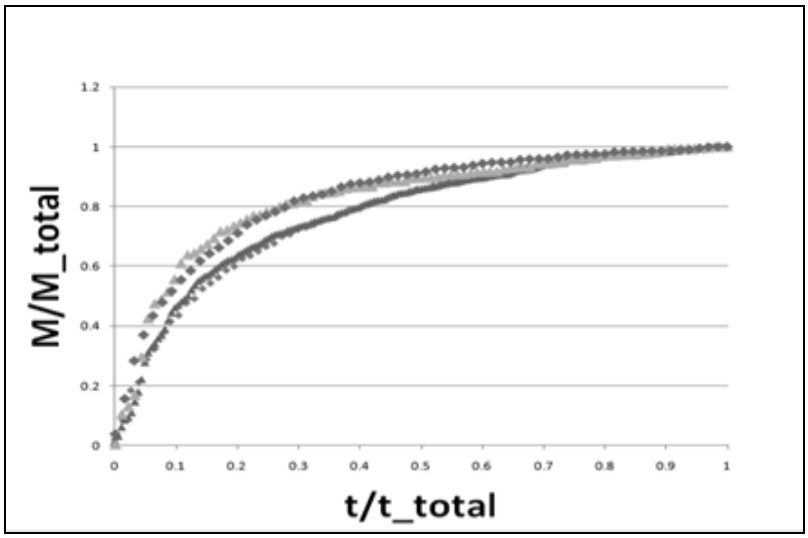

Figure 2-5. Sand Shakedown Testing, Top curves 5N, Lower Curves 1.5 N

Next to test the durability of the test apparatus, we conducted shakedown tests using non-nuclear grade graphite for up to 72 hours. During these tests we confirmed that the apparatus as well as the data logging system functioned reliably for extended lengths of time without issues. However, these tests revealed a larger than expected uncertainty associated with continual sampling of the particle mass over the entire testing period. The mass changed suddenly at certain points (0.3 to 0.6mg) and also the tare value of our scale changed over time as the collected particulate mass sat on the scale. Subsequently we ran additional tests (without spheres) to investigate these fluctuations. We found that vibration from the laboratory floor, as initiated by on/off cycle of the building's HVAC system, affected the scale during the testing period.

This problem was solved by the following changes: 1) moving the apparatus down to a basement laboratory, in another building, 2) adding vibration damping rubber below the scale and at the bottom plate supports, and 3) changing to periodic sampling instead of continuous sampling. The same tests were run again and yielded a satisfactory range in the data and standard deviations.

The last sub-system that received a full shakedown test was the furnace and cooling system. In the design phase of the apparatus, the temperature of the shafts holding the spheres within the furnace chamber could not be modeled in detail. There was not only an intricate geometry surrounding the shafts, but both radiant and natural convective heat transfer within a tight, bundled enclosure. Thus the temperatures were measured from each of the shafts and anticipated locations with less thermal tolerance. The tests were run on the Top Flange Stand in air since the wire feed-through were wired into other instruments. The hottest point outside the furnace measured was the moving shaft. At 800°C measured inside the heater, the maximum outer temperature was ~90°C at the worm gear under steady-state, while all the other locations measured were below 35°C. These temperatures were within the operational envelope of the components.

Thus, after these shakedown tests were completed the apparatus was considered then ready for actual testing. The only system not tested was pressure testing the vessel. However, the vessel had been hydro-tested (and certified) and the pressure fittings were checked with a Swagelok Gap Inspection Gage for proper installation and function. We thus felt the apparatus was ready.

2.7 Air Test Results

The first set of test runs were performed at room temperature in air with two grades of fine grained graphite including IG11 and GR001CC. The first three air test runs registered only ~50% of the ~1 to ~2 mg mass change deduced from before and after mass measurement of the spheres. In fact, upon inspection, dust particulates were found (swiping) on along the surrounding metal surfaces (before furnace was installed). Since these particles were barely visible, the particles were typically 40µm or less. Thus, the discrepancy in mass measurement was attributed to possible air currents within the configuration used.

We thus decided to check the mass of the samples themselves at interval with a separate analytical balance with a resolution of 0.1mg. The calibration of the balance was checked before each round of testing with an ASTM Class I 100 gram test weight and recalibrated as needed. This method of measuring the sample mass was more in agreement with the before/after mass measurement.

However, we found that particulates on the sample itself also needed to be removed before weighing. These particles had to be brushed off to measure the change of the graphite samples themselves. When this was done with a Mettler-Toledo balance cleaning brush, it led to a mass change on the 4th and 5th Air Tests double the ~1-2 mg change observed in the continuous run corresponding to the first two Air Tests. To test if brushing alone would change the mass of the graphite samples a simple check was conducted, the mass of fresh graphite samples was measured before and after the top surface was brushed multiple times. If a change was observed in the mass this was repeated until the mass readings were steady down to 0.1 mg.

The results revealed that the brushing did affect the overall mass by ~1 to 2 mg on average. Therefore, all subsequent tests had the fresh sample's top surface (where the furnace insulation particles were found) brushed off before being placed into the apparatus to eliminate this offset. When this was done, the average change in mass of subsequent tests closely matched the initial continuous run. The effect of the in-test brushing on Air Tests 4 and 5 compared to using pre-brushed samples is evident with the two distinct wear curves in Figure 2-6.

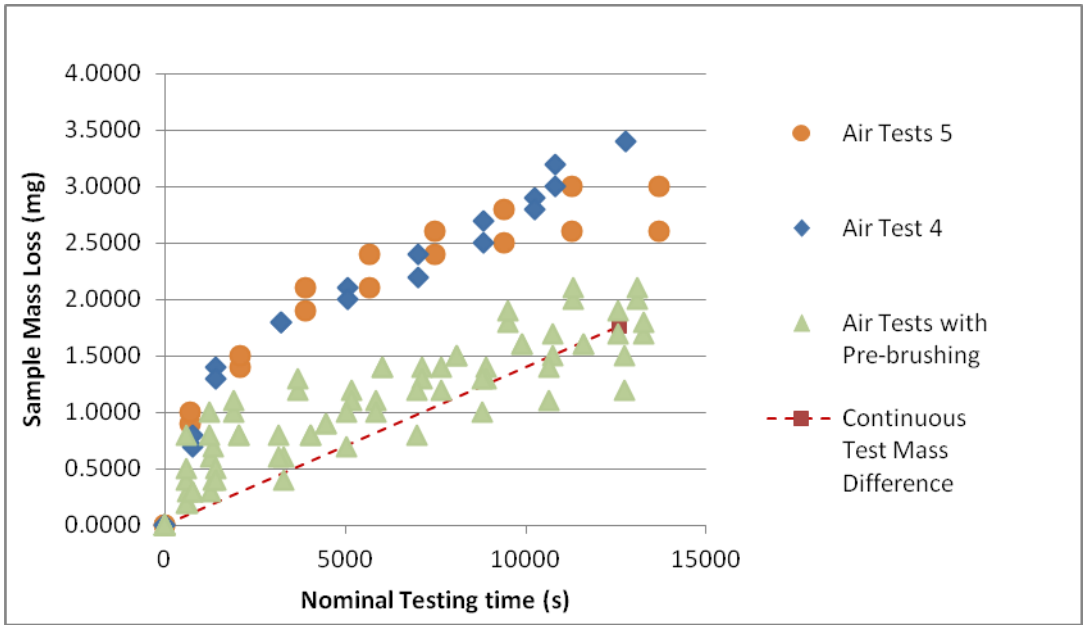

Figure 2-6. Air Testing Graphite-Graphite Wear Curves

We note that in Figure 2-6, the error in the time scale was negligible. Therefore the error bars are not shown here or throughout this report. Also, the error bar associated with mass data is not visible; it is the instrument's resolution, 0.1 mg.

The tabulated summary of the tests including Tests 4 and 5 are shown in Table 2-4. The average change in the sample mass of the graphite-graphite air tests was 1.76 mg for an average wear rate of 8.45E-08 g/N-m. The average kinetic friction remained constant throughout the test and the average value was 0.13 with a standard deviation of 0.02.

The calculated wear rates of individual sample during the test for the graphite-graphite air tests can be seen in Table 2-5, and in Table 2-6 the wear rates for the steel-graphite tests are also presented. The shaded cells in Table 2-5 were considered outliers as compared to the other values and not taken into account when calculating the averages (considered an outlier when more than 3 standard deviations outside the mean). The blanks in Table 2-5 and 2-6 were due to recording errors, with the exception of Test run 8 in Table 2-5. Test 8 had a sample rate of every 30 minutes for the entirety of the test. It was after this test that the sampling rate was changed to every 10 minutes during the first 30 minutes of the test to better measure the large wear rates observed in that time span.

Table 2-4. Graphite Air Testing Summary

Air Test	Temp. (°C)	Pressure (MPa)	Load (N)	Distance (m)	Wear Mass (g)	Average Wear Rate (g/N-m)	Friction
1	22	0	19.33	2134	0.0033	8.00E-08	0.16
2	22	0	19.37	2039	0.0017	4.30E-08	0.15
3	22	0	19.38	1912	0.0037	9.98E-08	0.11
4	22	0	21.04	2073	0.0067	1.54E-07	0.11
5	22	0	21.68	2187	0.0056	1.18E-07	0.10
6	22	0	21.4	2004	0.0036	8.39E-08	0.12
7**	22	0	19.78	2050	0.0027	6.66E-08	0.12
8	22	0	21.15	2122	0.0035	7.80E-08	0.11
9*	22	0	19.8	1933	0.0034	8.88E-08	0.13
10*	22	0	20.08	2193	0.0018	4.09E-08	0.15
11	22	0	19.75	2099	0.0041	9.89E-08	0.08
12*,**	22	0	19.27	2078	0.0025	6.24E-08	0.17

*Graphite Steel

**Recording Error, Total Distance Estimated

Table 2-5. Graphite Wear in Air at 20°C as a Function of Distance

g/m*10 (-6)									
Test	0-10 min	10-20 min	20-30 min	30-60 min	60-90 min	90-120 min	120-150 min	150-180 min	180-210 min
Air Test 3 (1)				1.5	0.7	1.6	1.6	1.3	4.6
Air Test 3 (2)				1.5	0.0	0.8	2.3	1.3	2.3
Air Test 4 (1)	13.4	11.5	2.8	2.0	1.9	2.1	1.7	6.5	1.3
Air Test 4 (2)	11.6	11.4	3.5	1.4	1.3	2.1	2.6	2.2	1.9
Air Test 5 (1)	16.4	0.0	4.5	3.4	1.4	2.1	0.7	0.7	0.0

Air Test 5 (2)	16.5	0.0	4.5	4.1	2.1	1.4	1.3	1.4	0.0
Air Test 6 (1)		6.0	0.0	1.9	2.1	1.3	0.0	2.1	1.1
Air Test 6 (2)		2.0	2.0	3.1	1.4	1.3	0.0	1.4	1.1
Air Test 7 (1)		1.9		1.4	1.4	0.7	1.4	0.7	0.6
Air Test 7 (2)		3.9		2.1	2.0	1.9	2.1	2.0	1.8
Air Test 8 (1)	10.6	6.0	3.7	1.4	1.1	0.6	0.7	0.0	0.8
Air Test 8 (2)	17.0	4.1	1.9	1.4	0.6	0.6	0.7	0.0	1.5
Air Test 11 (1)	4.8	3.9	5.9	0.0	2.1	2.1	2.7	1.4	0.0
Air Test 11 (2)	4.9	1.9	7.9	0.0	1.4	1.4	4.7	1.4	0.0
AVERAGE	**11.9**	**4.4**	**3.6**	**1.8**	**1.4**	**1.4**	**1.4**	**1.3**	**1.2**
St. Dev.	**4.9**	**3.8**	**2.2**	**1.1**	**0.6**	**0.6**	**0.9**	**1.1**	**0.8**

Table 2-6. Graphite-Steel Wear Rates

g/m*10(-6)									
Test	0-10 min	10-20 min	20-30 min	30-60 min	60-90 min	90-120 min	120-150 min	150-180 min	180-210 min
Test 9 (1)		10.3		8.5	1.4	4.1	3.3	2.0	1.4
Test 10 (1)	6.0	2.0	5.5	0.6	2.5	2	0.6	0.7	0.7
Test 12 (1)			5.8	1.3	1.4	2	2.6	0.7	0.7
AVERAGE	**6.0**	**6.1**	**5.7**	**3.5**	**1.7**	**2.7**	**2.2**	**1.1**	**0.9**
St. Dev.	**-**	**5.9**	**0.2**	**4.4**	**0.6**	**1.2**	**1.4**	**0.7**	**0.4**

3. Experimental study and analysis

The collected data was sorted into files and analyzed (Figure 2-4). Upon completion of each test, graphite samples were taken out from the apparatus and weighed. Photos of the surface of the graphite sample were taken so that the condition could be examined. The particulate mass was weighed and preserved for later SEM (scanning electron microscope) and XRD (x-ray diffraction) analyses.

3.1 Data and Sample Analysis

The SEM instrument used was a JOEL USA Inc., model JSM-6610V was used to determine the microstructure of the graphite sample surface. The SEM images were acquired at the Microscopy and Characterization Suite (MaCS) laboratory, Center for Advanced Energy Studies (CAES) in Idaho Falls.

As for micro-structural change of graphite particulate mass, before and after the wear test, we employed XRD. The XRD analysis was done at Virginia Commonwealth University in collaboration with Drs. Bertino and Franzel. The conditions used for the XRD are listed in Table 3-1.

Table 3-1. Conditions for XRD.

Model	**PANalytical X'Part Pro**	
Generator Voltage	45kV	
Tube Current	40mA	
Anode Material	Cu	
Slits	Divergence	Receiving
	0.25 mm	0.1 mm
Scan Step Size	0.026	

3.2 Reliability of Results

Since a literature review revealed the existence of few to no previous experimental study under the same testing conditions, this study compared the data generated to the similar works as a point of reference rather than as an absolute comparison. The experimental conditions of this study were compared to those attributed to Luo et al. (2005) and Stanfield (1968) in Table 3-2. The experiments conducted by Luo and Stanfield studied graphite properties for a high-temperature gas-cooled reactor (HT-GCR). The experimental conditions here were chosen to simulate the HT-GCR condition. In Figure3-1, our experimental results are compared to Luo's and Stanfield's studies at various temperatures. The temperature dependent wear rate under two different helium pressures (0.1MPa and 1MPa) are shown with Luo's data (0.1MPa) and Stanfield's data (0.1MPa).

Table 3-2. Experimental Conditions of Wear Test of Graphite in Helium.

	Graphite		Temp. (°C)	Helium Press. (MPa)	Wear testing mode		Friction load	
	Grade	Density			Orientation	Movement	Contact force (N)	Dist. (m)
NEUP 09-151	**IG-11, Toyo Tanso, Iso-molded**	**1.76**	**20-750**	**0.1-6.5**	**Sphere/Sphere**	**Both Rotating**	**20**	**1000**
Luo et al.			20-400	0.1	Sphere/Plate	Sliding vs. Stationary	30	720

Stanfield	PGX, Union Carbide, Molded	1.77	20-800	0.11	Plate/Plate	Sliding vs. Stationary	78.5	125

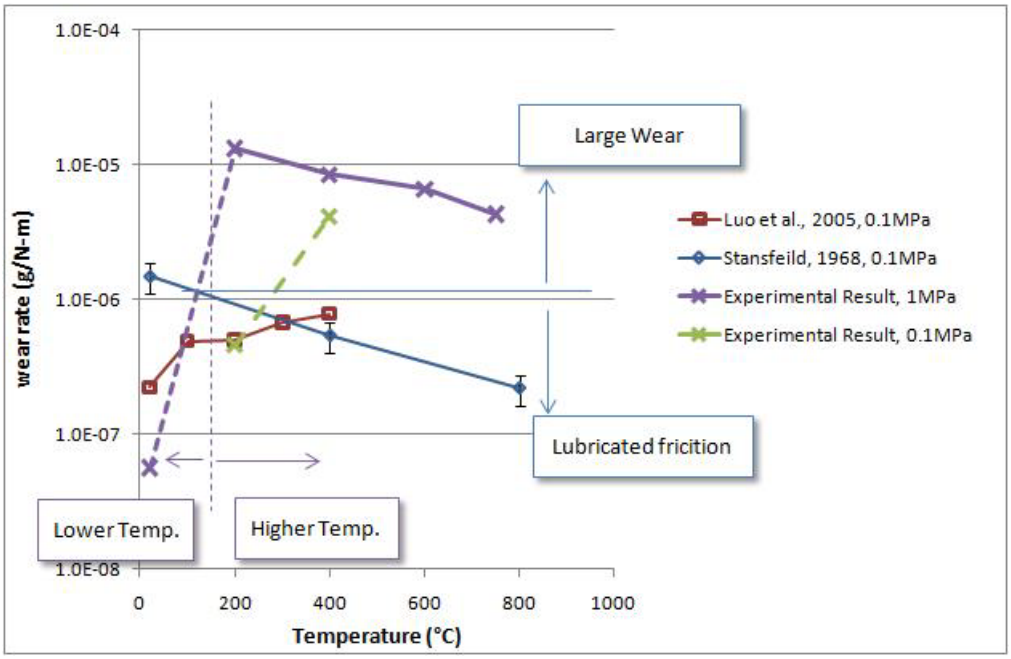

Figure 3-1. Wear Rate Comparisons to the Other Studies for Graphite-on-Graphite Contact.

This work's results of wear rate at higher temperatures (200° to 750°C) showed a 5-10 fold larger magnitude in contrast to Luo's and Stanfield's results (Experimental Results, 1MPa in Figure 3-1). At high temperatures (200° to 750°C), the result of the high wear rate is attributed to a "large wear" mode, while "lubricated" friction is associated with the low wear rate at low temperature (20° to 200°C). Since both Stanfield and Luo reported reflective and smooth worn surfaces of graphite samples, the wear mode in their studies is assumed to be "lubricated" friction, consistent with their low wear rates. The wear rate in this study under "lubricated" friction was in agreement with these previous studies as the wear rate's absolute magnitude was small.

The two wear modes, what this study calls "lubricated" friction and "large wear" were recognized by the other researchers as well. Two wear modes will be described in detail in later. Stanfield noticed two types of surface conditions, "grooved and non-reflective" and "reflective". Also, in Luo's study, the transition temperature from the "flat" surface to the surface with "many grooves" was between 200°C and 400°C. Luo et al. (2005) attributed the change in wear phenomena to a change in the stress distribution. When frictional motion is introduced to the surface of graphite the tangential force due to frictional contact influences the stress distribution along the contact zone. When a tangential force exists, the contact region is subject to wear due to compressive stresses. At low temperature, Luo et al. (2005) reported that yield failure was unlikely due to graphite's high compression strength. This was the explanation of wear due to "lubricated" friction. For "large wear", on the other hand, Luo et al. postulated that yield failure was likely in the region where the tensile stress exceeded the material's tensile stress at high temperature. However, our experimental results at helium pressures, 1.0 to 6.5MPa, extended Luo et al.'s results to that substantiated as "large wear".

The experimental apparatus designed and developed by Johnson (2012) was used to conduct tests reported here. The experimental uncertainties include load cell, pressure transducer, torque meter,

mass scale, thermocouple probe, encoder, and linear potentiometer. The experimental uncertainty, an estimate of what is attributed to the experimental apparatus is summarized in Table 3-3.

In terms of uncertainty associated with instrumentation, kinetic friction and wear rate have uncertainties estimated as 7.1% and 1.7%, respectively. For example, in Figure 3-2, the kinetic friction with instrumentation uncertainty as error bars is shown.

As shown in Figure 3-2, a trend versus temperature of kinetic friction is observable, even with the error bars for each test. We consider the uncertainty small enough to deduce the influence of both temperature and pressure on wear. Since several tests were done under the same experimental conditions, the error bars in following chapter are as implicitly included data under the same test conditions.

Table 3-3. Instruments Uncertainty for Wear Rate and Friction Calculation.

Instrument	Measure value	Uncertainty	Convert into	Uncertainty
Torque meter	Torque (N-cm)	0.7219N-cm	Kinetic Friction	7.1% (Using data for Test 8 0.465)
Load cell	Contact force (N)	0.225N (ave. 1.125%)		
Mass scale	Mass(g)	0.00005g	Wear Rate	1.7% (Using data for Test 13 1.6×10^{-7}g/Nm)
Encoder	Rotation (Hz) →Distance(m)	0.0075m (ave. 0.0074%)		
Pressure transducer	Environment pressure (psi)	5psi		
Thermocouple probe	Environment temperature (°C)	2.8°C		
Linear potentiometer	Sample position (m)	0.25mm		

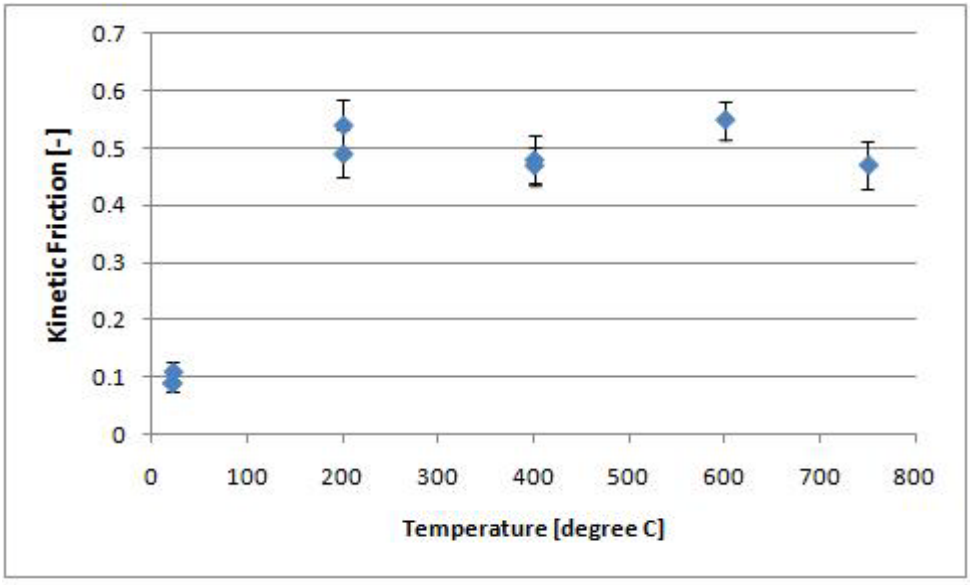

Figure 3-2. Kinetic Friction with Instrumentation Uncertainties.

3.3 Two Wear Modes

When the experimental apparatus demonstrated the ability to wear test, the main set of experiments were conducted under a helium gas environment. The helium test resulted in two different types of wear modes. The two wear modes were first found in the graphite sample's appearance. One wear mode showed a "lubricated" characteristic with a reflective and thin wear scar on the surface (Figure 3-3 a) with a small amount of graphite dust (average of 0.001g). The other wear mode showed a "large wear" with dark and wide wear scars and produced a two magnitude greater amount of graphite dust (up to 0.5g) (Figure 3-3 b). The "lubricated" characteristic was seen in the room temperature, 20°C and lower helium gas pressure (0.1, 1 and 3MPa) test. The "large wear" was seen when the temperature went up to 200°C or higher under 1 to 6.5MPa helium pressure. There are exceptions. When the temperature stays at room temperature, 20°C and the helium pressure is high (6MPa, Test 13), the wear mode resulted in "large wear" and produced a lot of dust (0.45g). Also, at 200°C with low helium pressure (0.1MPa) (Test 19 and 21), the surface showed reflective and thin wear scar and stayed in a "lubricated" condition. The repeatability of the phenomena was confirmed by the other test results (Table 3-4).

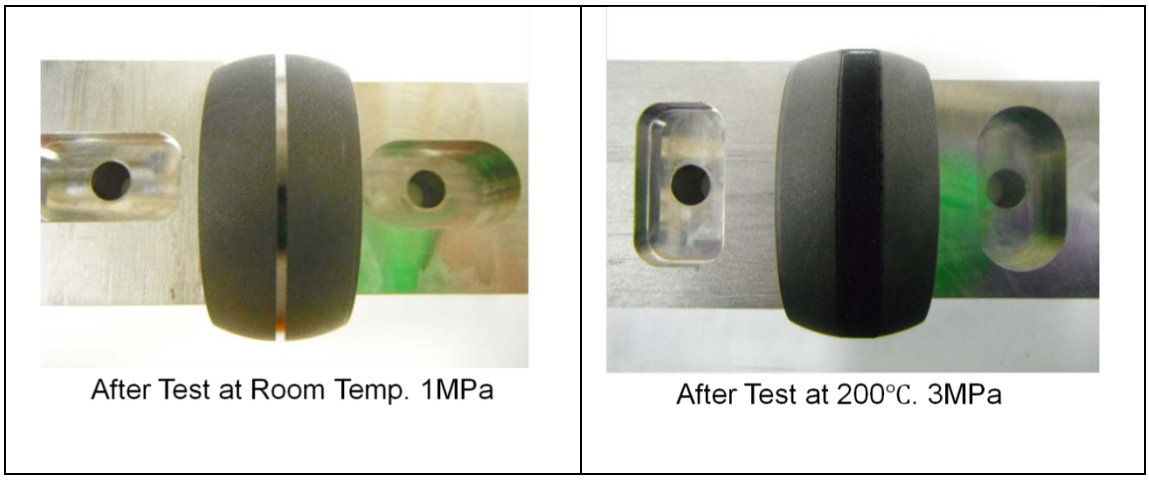

Figure 3-3. Tested Samples (a) Left: Lubricated Characteristic, (b) Right: Large Wear.

Table 3-4. Graphite Appearance after Wear Tests.

Helium Test

Temp./Pressure	101 kPa	1 MPa	3.0 MPa	6.5 MPa
20°C		Lubricated	Lubricated	Large Wear
200°C	Lubricated	Large Wear	Large Wear	Large Wear
400°C	Large Wear	Large Wear		Large Wear
600°C		Large Wear		
750°C		Large Wear		

(2)Graphite-on-Steel Test

Temp./Pressure	1MPa
20°C	Lubricated
200°C	Large Wear

(3)MLRF Test

Temp./Pressure	1MPa
20°C	Lubricated
200°C	Large Wear

3.4 Temperature Effects

3.4.1. Temperature Effect on Wear Rate and Friction

In the literature, the temperature effect on graphite wear was discussed. As shown in Figure 3-1, two previous studies showed the conflicting temperature trends on wear rate, either as increasing or decreasing with temperature. The experimental wear data as reported mainly differ in testing conditions and graphite grades. However, both Stanfield's study and Luo's study mentioned that when the graphite samples showed a reflective and smooth worn surface, the resulting wear rate was smaller than the samples with a grooved and non-reflective surface. In this study, it was observed the same tendency "lubricated" friction with low wear rate and "large wear" with high wear rate. The temperature dependence on wear rate for all helium testing is given in Figure 3-4.

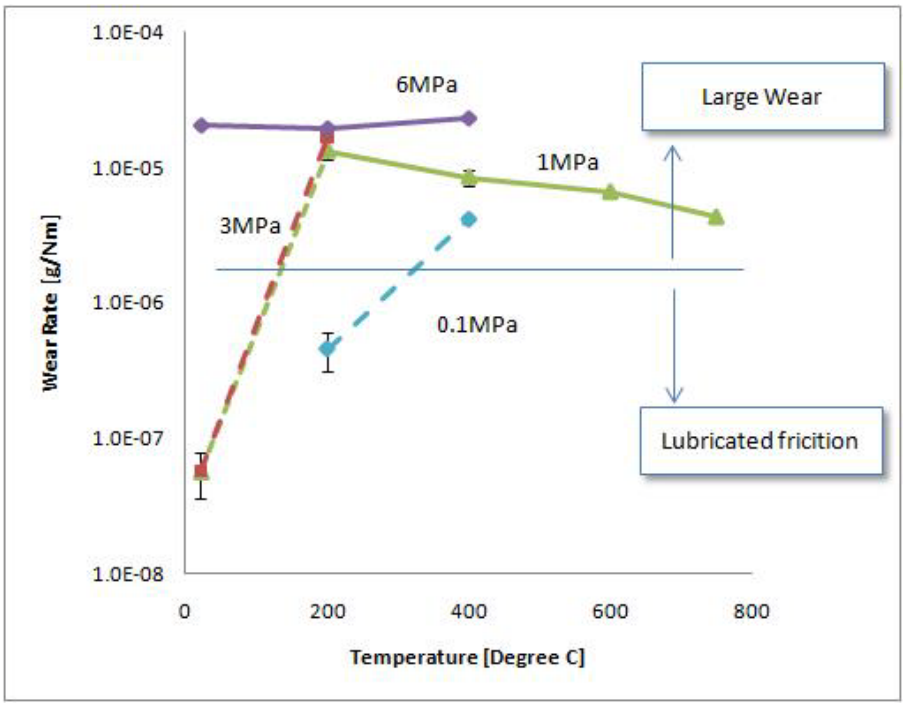

Figure 3-4. Temperature Dependence on Wear Rate under Various Helium Pressures

In Figure 3-4, the wear modes, "lubricated" and "large wear" were distinguished by wear rate and appear as dashed-lines. The transition of two modes is delineated with the indicated arrows. For "large wear" mode, the wear rate trend at 1MPa is slightly decreasing with temperature, while the data at 6MPa is approximately constant with temperature. The reason for a decreasing trend on wear rate for 1MPa helium pressure will be discussed in Chapter 3.5. The temperature trend on kinetic friction can be seen in Figure 3-5.

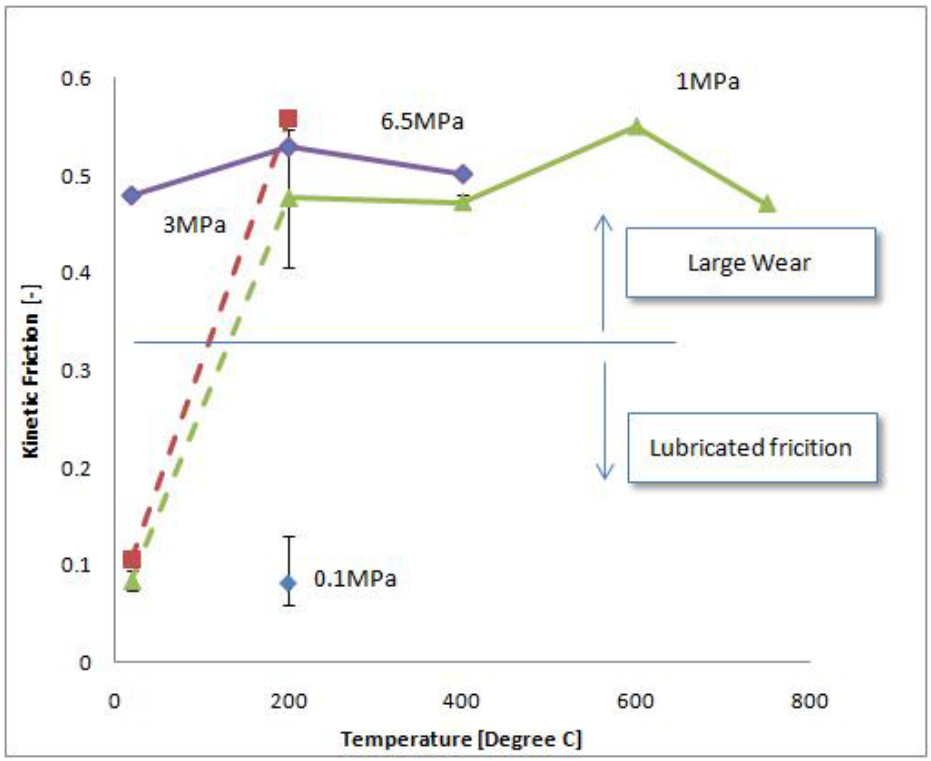

Figure 3-5. Temperature Dependence on Kinetic Friction under Various Helium Pressures.

The temperature dependence on kinetic friction also shows similar trends to support our understanding of the wear mechanisms. The dashed-lines and arrows indicate the transition between "lubricated" friction and "large wear". The "lubricated" friction mode corresponds to a low friction coefficient (average of 0.1) and the "large wear" mode corresponds to a high friction coefficient (average of 0.51). In 1995 Robert discussed the influence of the presence of inert gas on friction of graphite. In Robert's study, different kinds of inert gases were tested for pin-on-disc wear tests with two kinds of graphite, electrographite (EG319) and morganite (MY3A), at room temperature. Robert suggested that the presence of inert gas affects the superficial crystalline structure on the graphite's surface, which essentially reduces friction. The gas atoms that are potentially adsorbed or embodied into the surface improve the mobility of superficial crystallites that orient themselves parallel to the wear direction under the action of the contacting asperities. This leads to a decrease of both the roughness down to 0.6μm (c.l.a.), and the surface energy (Robert, 1995). Stanfield, Robert, and Luo reported a decreasing trend on wear properties characterized by a reflective and smooth band of contact, i.e. wear scar. This means that the likely phenomenological mechanism was what we call "lubricated".

Luo's experiments were conducted under helium environment from 20°C to 400°C. Luo reported different wear mechanisms at different temperatures. There occurred a transition in wear from low friction (0.15) at 20°C and high friction (0.336) at 400°C (Luo, 2005). The friction coefficient at 20°C, as reported by Luo, showed agreement with our result for "lubricated" friction (average of 0.1). Although the friction coefficient at 400°C was lower than our result (average of 0.51), both our result and that reported by Luo et al. showed a significant increase in friction when the wear mode changed to "large wear". Thus, in both our work and that of Luo's, a similar transition from "lubricated" to "large wear" was observed.

3.4.2. Temperature Effect on Wear Particle Production

As mentioned before, Figure 3-4 shows that the wear rate decreased with increasing temperature under 1MPa helium pressure. On the other hand, there is no evidence of temperature dependence of kinetic friction (Figure 3-5). While wear rate directly influences wear mass, kinetic friction is a measure of the contact torque. The decreasing trend in wear rate was observed only due to a change in the wear induced mass loss (Figure 3-4). This can be explained with wear particle production change with temperature.

The graphite particles were collected from a tray located under the graphite spheres in the test apparatus. The collected graphite particles were characterized using a SEM. The images of graphite particles from wear tests at different temperatures are shown in Figure 3-6.

The graphite particles were collected from a tray located under the graphite spheres in the test apparatus. The collected graphite particles were characterized using a SEM. The images of graphite particles from wear tests at different temperatures are shown in Figure 3-6.

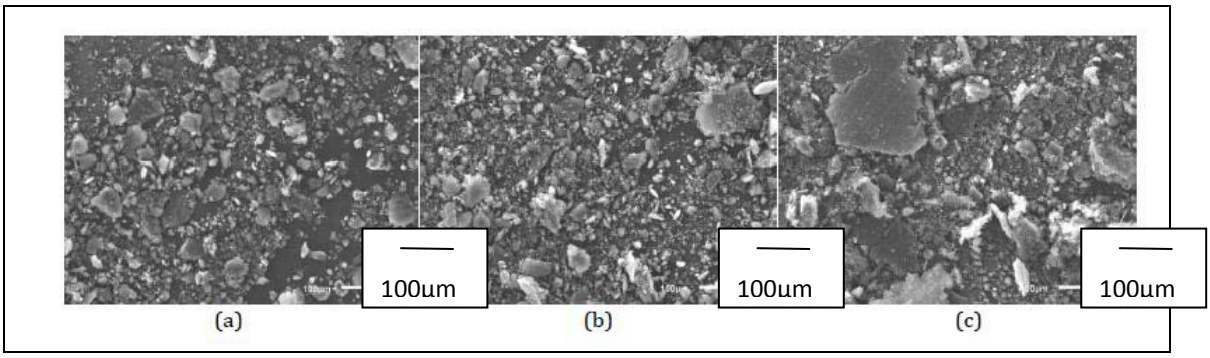

Figure 3-6. SEM images of graphite particles from wear test at (a) 200°C, (b) 400°C and (c) 750°C.

It is self-evident from the figure that the distribution of graphite particle images from SEM are different in size and shape for the test temperatures as noted. As seen in Figure 3-6(b) and (c), large-sized flakes are observed at 400°C and 750°C, respectively. The change from powder formation at 200°C to powder and flake formation at 400°C is observed by comparing the images of graphite particles Figure 3-6(a) and (b). At 400°C and 750°C, the much larger area-to-weight ratio was observed for “flakes” in comparison to particulates characterized at 200°C as “powder dust”. It is plausible that flakes are more likely to adhere to the graphite surface because of its mass (thus larger lift-off threshold) and carbon bonds in contrast to powder dust. However, results of mass or carbon bonding effects cannot be verified using SEM images. If this is in fact the dependence, a decrease in the wear rate trend with higher temperatures, 200°C up to 750°C, should result.

The temperature trend on wear rate in terms of graphite dust formation change is one aspect of the mechanism. For both wear rate and friction, there is another trend on temperature that distinguishes lower values as “lubricated” friction and higher values for “large wear”. This trend is not influenced by temperature alone.

Based on our literature survey, there were indications of change in the superficial crystalline morphology. We thus sought to investigate the micro-structural change of graphite and used X-ray diffraction (XRD) to determine the crystalline structures of solid samples. In the case of (non- nuclear grade) carbonaceous materials, analysis by XRD is well documented. We next discuss the wear modes based on XRD analysis.

3.4.3. Temperature Effects on Graphite Particle Crystalline Structure

X-rays are electromagnetic radiation of wavelength from 0.01 to 10nm. XRD has been in use as "fingerprint-like characterization" of crystalline materials; thus determination of their crystalline structures. Each crystalline solid has a unique, characteristic XRD pattern which in essence is its "fingerprint". X-ray crystallography of graphite indicates how the carbon atoms are ordered; that is, with the structure determined, the inter-planar spacing, size of crystallite, and degree of graphitization (Miyake, 1996) is considered well-known for a pure sample.

The samples from various wear test conditions that were analyzed by XRD are given in Table 3-5.

Table 3-5. Graphite Samples for XRD Analysis.

	Temperature, °C	Helium Pressure, MPa	Note
Test 7	200	1.0	Ultra High Purity helium gas
Test 8	400	1.0	Ultra High Purity helium gas
Test 9	200	1.0	Graphite-Steel
Test 13	20	6.5	Ultra High Purity helium gas
Pre-test			From bulk bar
Pre-test			From machined sample

For this case, the sample's X-ray diffraction pattern was compared to graphite's indexed reference (Figure 3-7). In Figure 3-8, the pre-test sample's X-ray diffraction pattern is depicted compared to the indexed reference. The pre-test sample is collected by grating IG-11. The positions of the two figures are adjusted to compare the incident angle, 2θ. The pre-test sample has the same peaks for the (002), (100), (101), (004), and (110) planes with moderate intensity distribution as shown. There was no other peak observed. This means that the nuclear grade graphite samples tested have a well-graphitized crystalline structure and no significant impurities.

The second step for XRD analysis is a comparison between samples to identify the difference(s). The post-test XRD spectra at two different temperatures are shown in Figure 3-9. The 200°C and 400°C tests are compared with pre-test sample. The graphite dust samples for 200°C and 400°C tests were collected from the tray beneath the graphite spheres in the testing apparatus. Both the 200°C and the 400°C tests show similar X-ray diffraction patterns. Although the 200°C test shows higher intensity for the (002) plane, there is no significant difference observed between the spectra obtained from 200°C and 400°C tests. A comparison with the pre-test sample indicates that all of the diffraction peaks for 200°C and 400°C tests have a lower intensity than the pre-test sample. Moreover, there is no distinct diffraction peaks for the (101) and (100) planes. We note that the merging peaks largely mean that graphite has lost its well-graphitized crystalline structure (Inagaki, 1963). This can be seen as evidence that due to wear under 1MPa helium pressure, at 200 °C and 400°C, our graphite samples have been subjected to physical degradation of their crystalline structure. The schematic images of (101) and (100) planes are seen in Figure 3-10. Since the graphite synthesis process requires highly graphitized treatment at very high temperature (~2500 °C), the change in crystalline structure during a wear test is the result of both contact wear and environmental conditions (pressure, temperature), especially the influence of high helium pressure, which will be discussed next.

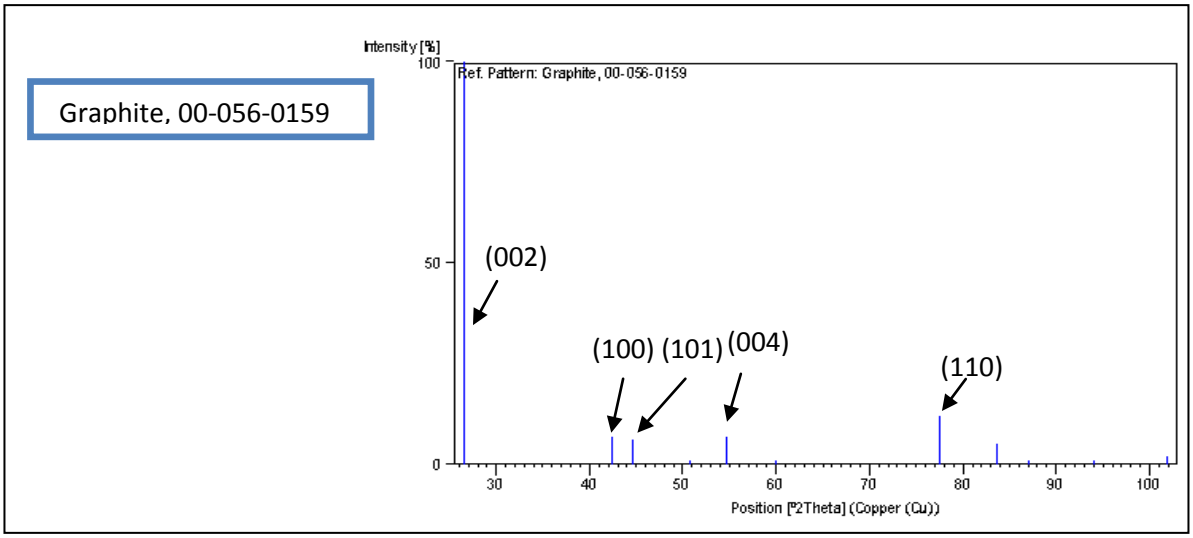

Figure 3-7. Index of X-ray diffraction pattern for graphite. (Howe, 2003).

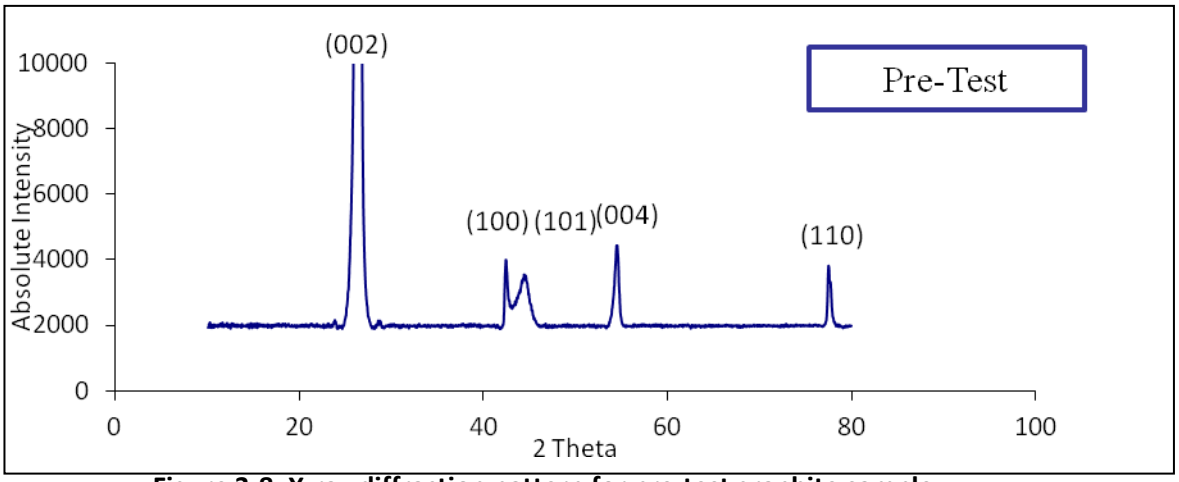

Figure 3-8. X-ray diffraction pattern for pre-test graphite sample.

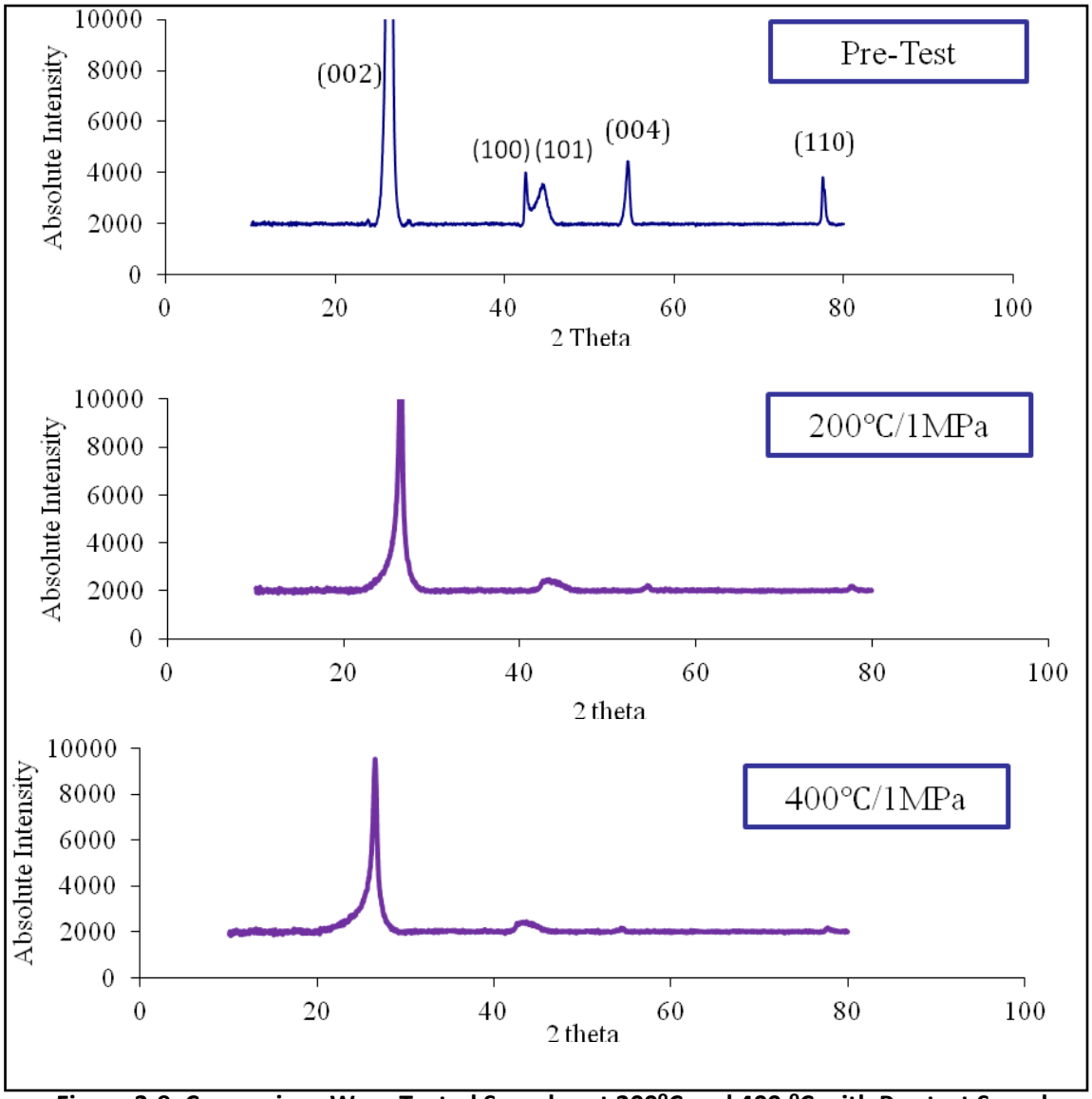

Figure 3-9. Comparison Wear Tested Samples at 200°C and 400 °C with Pre-test Sample.

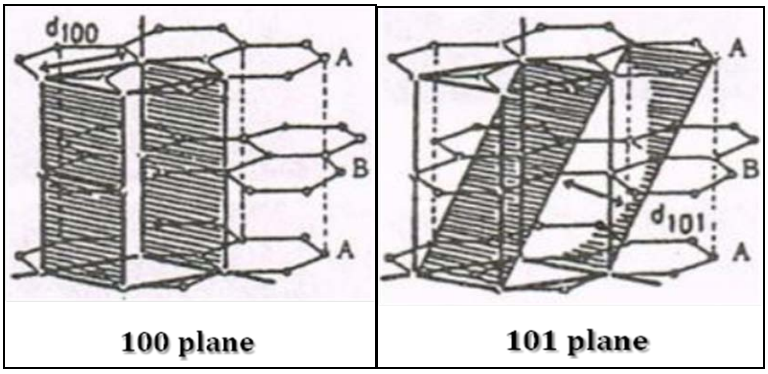

Figure 3-10. Image of (100) and (101) Plane (Miyake, 1996).

3.5. Pressure Effects

Unlike the temperature effect on graphite wear, the influence of pressure on wear has not been widely discussed in literature. The influence of helium pressure on graphite-on-graphite friction was studied by Robert (1995). In Robert's study, the introduction of helium gas led to a decrease of the friction coefficient from 0.45 to 0.02. However, Robert's experiment was only conducted at a low helium pressure range, 0.01 to 0.16MPa, for 10 hours under a sliding velocity of 30mm/s (total sliding distance of 1080m). Robert did not attribute the influence of helium pressure change on friction but the phenomenon of migration of helium atoms on the surface. In his discussion, the helium atoms "embed" themselves into the surface of graphite; then, increased the mobility of superficial crystallites. Thus, the surface roughness and surface energy decreased and consequently, decreased the friction coefficient (Robert, 1995).

If the graphite surface indeed adsorbs or embeds "resident" gas atoms, the facilitated frictional contact may yield a macroscopically smooth and optically reflective. Macroscopically this was in fact observed in the current sample; that is, we called this "lubricated wear". In contrast, for our results attributed as "large wear", the worn surface characteristics were different. The surface of the graphite sample for "large wear" was degraded and covered with wear particles. The helium pressure effect on wear rate and friction for this study can be seen in Figure 3-11 and 3-12.

Even at low temperature (20°C), both wear rate and friction showed high values at high helium pressure (6.5MPa). Also, at 200°C, the low helium pressure (0.1MPa) test showed low values for both wear rate and friction, while at higher helium pressure (1MPa to 6MPa) tests showed larger values. Thus graphite wear is affected by helium pressure in the same way as temperature and the low wear rate occurs only if both pressure and temperature are low in contrast to high wear rate when either pressure or temperature is high.

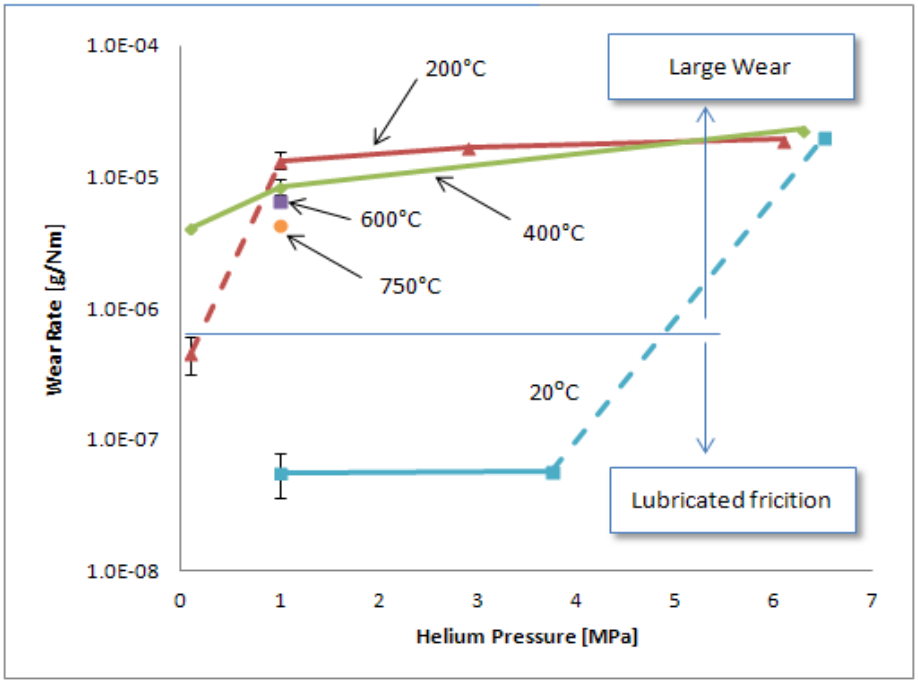

Figure 3-11. Pressure Dependence on Wear Rate at Various Temperatures.

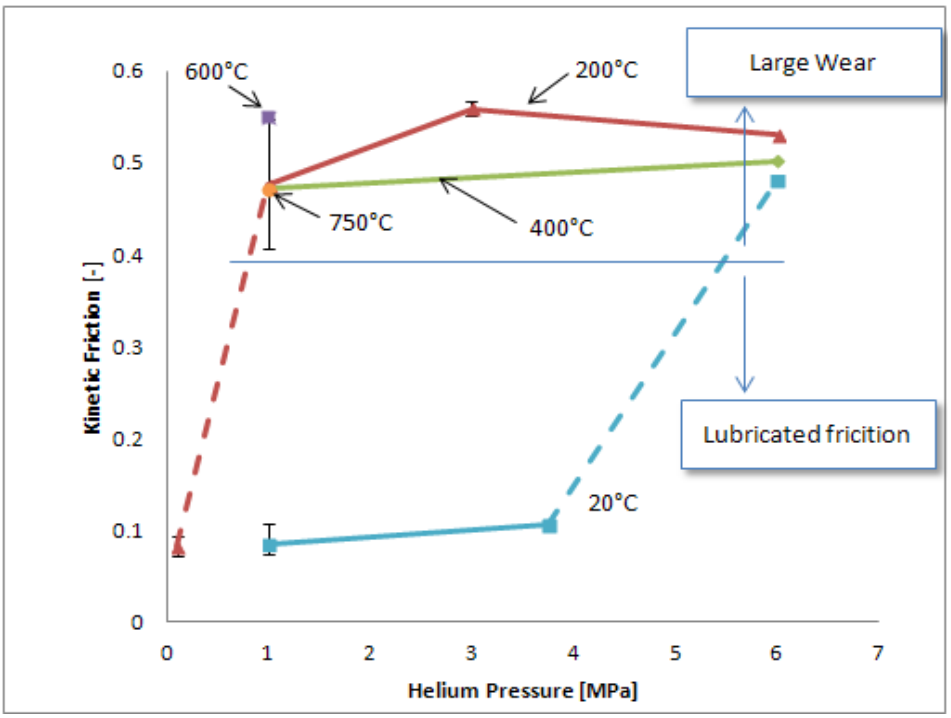

Figure 3-12. Pressure Dependence on Kinetic Friction at Various Temperatures.

To understand the effect on crystalline structure via graphite surface wear, XRD analysis was again performed. Results for pressure effect on crystalline structure for 20°C at 6.5MPa test are shown in Figure 3-13 relative to the pre-tested sample and the 200^{o}C at 1MPa tested sample. As shown, there is no significant difference between the temperature and pressure 'paired', 20^{o}C /6.5MPa test and 200 ^{o}C/1MPa test. Both graphite samples depict a prominent peak for the (002) plane and merged peak for (100) and (101) planes. The test at 20°C/6.5MPa resulted in "large wear" mode with the same crystalline structure as sample at 200 ^{o}C/1MPa.

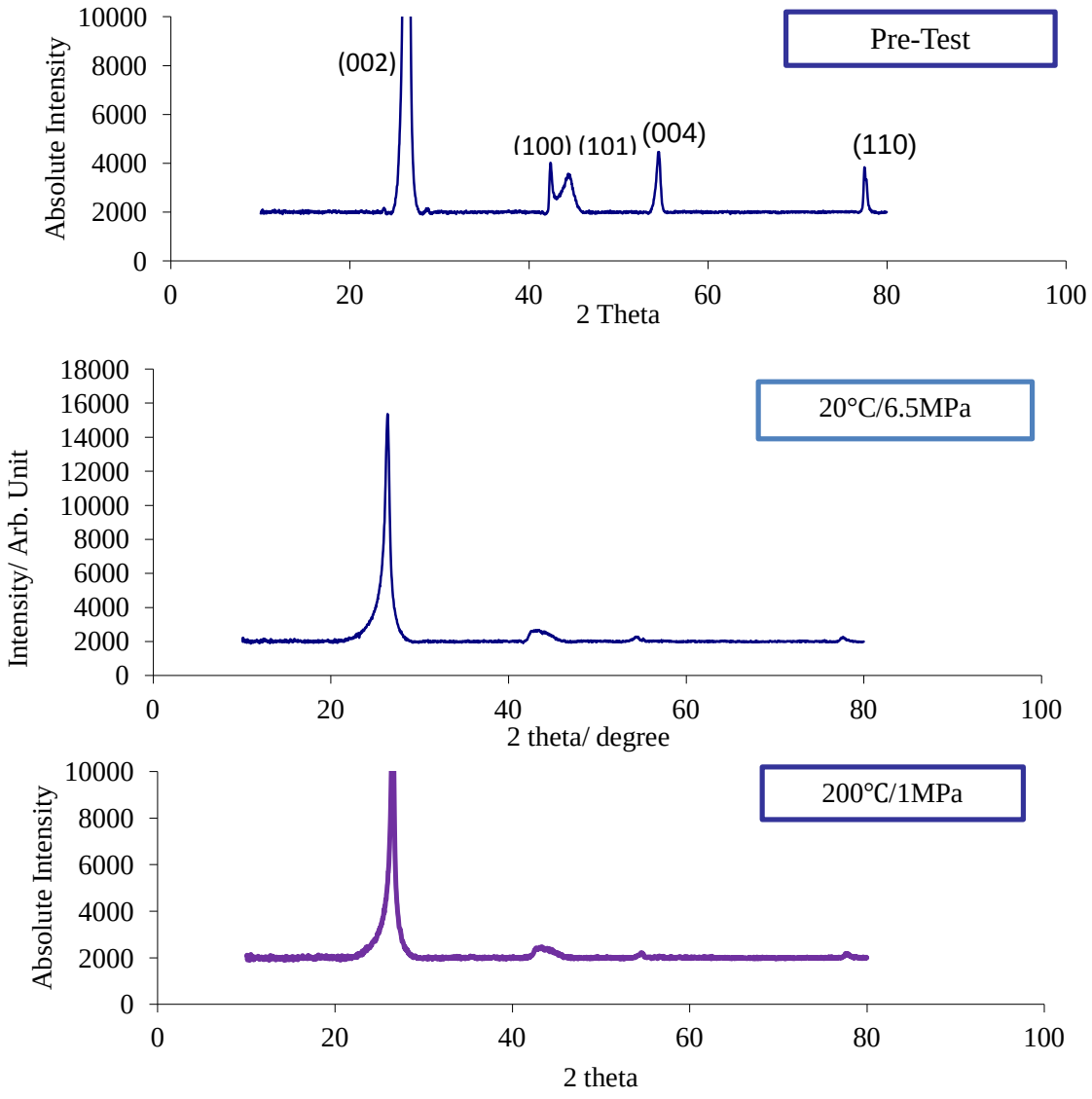

Figure 3-13. XRD Pattern Comparison with 6.5MPa Tested Samples at Room Temperature to 200°C Tested and Pre-test Samples

The SEM images of graphite particle for 20°C/6.5MPa test is shown in Figure 3-14. We also included the SEM image from tests done at 200 °C/1MPa as a point of comparison. The SEM images generally show the same grain size distribution with similar gray-scale distributions for both graphite samples. That is, there is no apparent pressure effect on crystalline structure for both 20 °C/6.5MPa and 200 °C/1MPa tests.

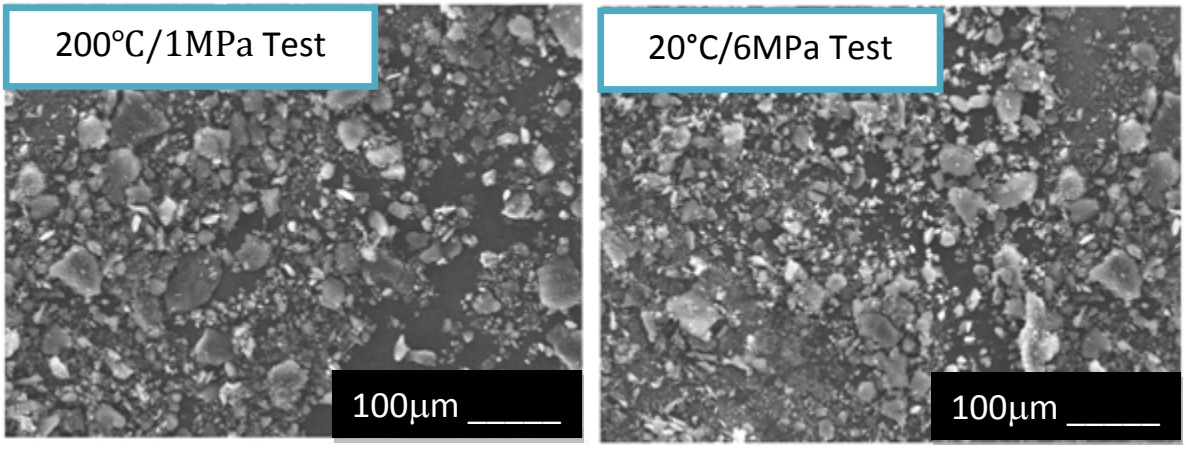

Figure 3-14. SEM Images of Graphite Particles for 20°C/6MPa Test and 200°C/1MPa Test

3.6. Transition from "Lubricated" friction to "Large Wear"

The current wear tests provided evidence of two phenomena under different helium pressures, at various temperatures. In the case of what we called "lubricated" friction, there was corresponding negligible wear dust generated and an optically reflective wear scar on the surface. On the other hand, when particulates generated were considered large, (up to 0.5g), the contact surfaces appeared darker and produced a broad wear scar. The SEM image and XRD analysis revealed that the surface crystalline structure changed as a result of the wear test. Both frictional contact and testing condition contributed to the change between "lubricated" friction and "large wear". The mechanisms of these two wear modes were described in the literatures as superficial crystallites change. The schematic drawing of phenomenological changes are shown in Figure 3-15.

As Figure 3-15 shows, graphite maintains a well graphitized crystalline structure as manufactured. Then, the machining process produces a spherical shape with a grained surface (Figure 3-15 top). Once frictional contact forces are introduced in testing, the morphology changes. At the beginning, the superficial crystallites migrate parallel to the wear direction within the contact zone. This study postulates that the migration occurs due to helium atoms adsorption and possible 'embedding' into (near) sub-surface. This facilitates relative sliding motion at the surface and results in "lubricated" friction as noted. Development of morphological changes ultimately results in a reflective contact 'band'. When either temperature and helium pressure alone or together assume larger values, due to the change in the material's properties, asperities on the surface then appear to contribute to different mode of particulate generation, one called "large wear".

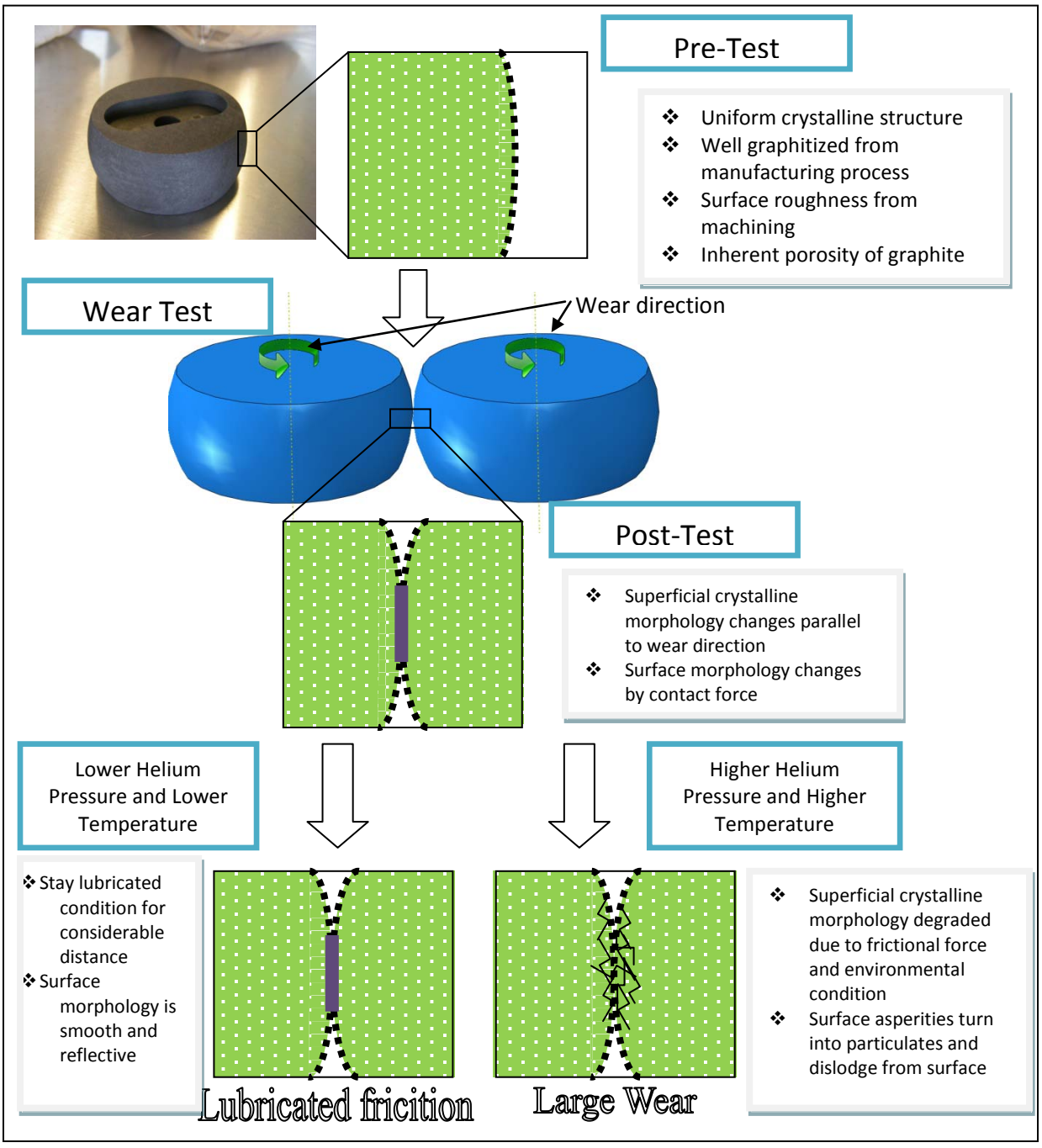

Figure 3-15. Schematic of Two Wear Modes.

The SEM images depicting the wear 'scar' is shown in Figure 3-16. The upper two images are from this study and the lower two images are from Luo's study (2005). The Luo's wear test was conducted under a lower helium pressure (0.1MPa) than this study (1MPa). At room temperature, both this study and Luo's visually show similar smooth surfaces. At 400°C, on the other hand, the surfaces have visually changed into a "large wear" mode, in contrast to Luo's study. The surface image for 400°C from Luo's study shows a combination of partially smooth and spalling pits while the surface from this study shows a degraded surface throughout. Since the testing (helium) pressure for Luo's study was lower than this study for the 400°C tests, the observed surface for Luo's study is thought to be the transition from "lubricated" friction and "large wear".

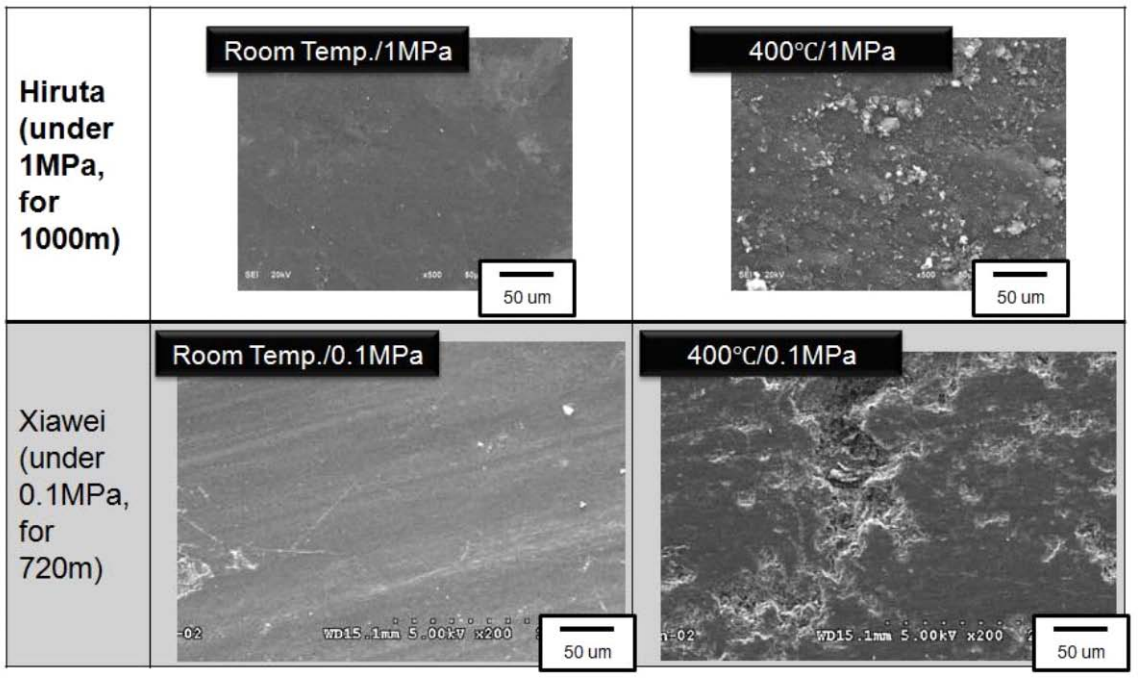

Figure 3-16. SEM Image of Wear Scar on Graphite Surface at Transition from "lubricated" to "lar wear".

Figure 3-17 shows the wear test results from this study and two others as represented in terms of helium pressure versus temperature. The shades of bluish-gray define approximate regions between two modes of wear. The two other studies were done under low helium pressure (0.1MPa) at various temperatures. In Stanfield's study, 400° and 800°C tests indicated "lubricated" friction with reflective surface and low wear rate. Luo's study showed "lubricated" friction mode for room temperature tests and combination of "lubricated" friction and "large wear" from 200° to 400°C. As noted, in the present work, a wear mode of "lubricated" friction was observed at lower temperature and pressure. At higher temperature and helium pressure, the wear mode transitioned to "large wear" with a degraded surface. Furthermore, this study determined that there is the phase of "large wear" in the presence of high helium pressures and temperatures. For the majority of operating conditions of a pebble bed reactor core, this study anticipates a condition of "large wear" that results in a greater amount of graphite dust than "lubricated" friction. Rostamian showed that particulate generation from these experimental results estimates a wear mass of approximate 2.3kg/yr at temperatures higher than 200°C, for a PBR of an actual size such as HTR-10. (Rostamian, 2012). We noted that this dust production rate is still much

smaller than that estimated to be required for dust combustion/explosion at some 508.3kg/yr (Poulsen, 2011).

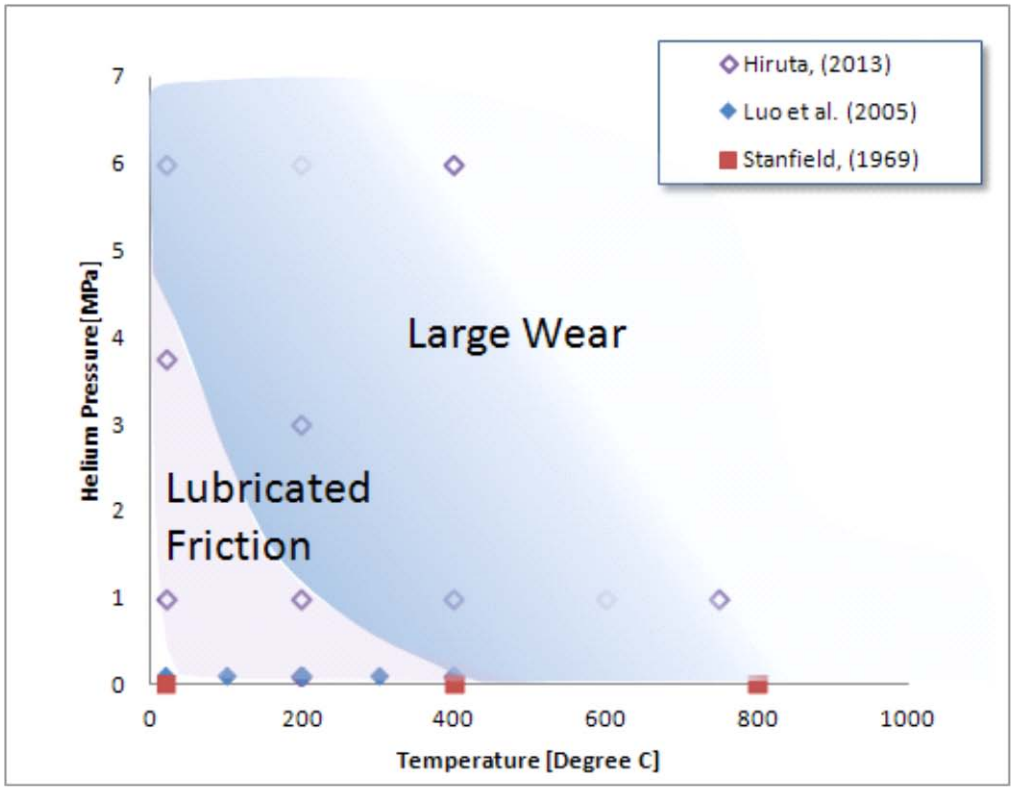

Figure 3-17. The Wear Test Conditions of Helium Pressure Versus Temperature.

3.7. Graphite-on-Steel Test and MLRF test

Two other wear test configurations were conducted in this study. We investigated graphite-on-steel contact and a different grade of nuclear grade graphite. The graphite-on-steel contact was a simulation of the contact of graphite spheres against the wall during loading/unloading or online refueling of the PBR. A different grade of nuclear grade graphite test was considered because of morphological differences of nuclear grade graphite depend on proprietary manufacturing processes.

The wear tests conducted at room temperature, 20°C, and 200°C under 1MPa helium pressure were compared to the graphite-on-graphite tests with IG-11. Since test conditions for helium tests covered the range of "lubricated" friction and "large wear", the test conditions of 20°C, and 200°C under 1MPa helium pressure were considered sufficient. The results from these tests are described below.

3.7.1 Graphite-on-Steel Test

As noted, the graphite-stainless steel contact is anticipated to occur during online refueling of the PBR. Select, burnup assayed fuel spheres with insufficient burnup are reintroduced in to the core and thus encounter frictional contact via the refueling system. The experimental arrangement is shown in Figure 3-18. The results were calculated as the same as all of the other tests. We found unique wear particles for Test 9 (Figure 3-19). The particle had a larger size and a flake like shape, while most of the other particles were fine and uniform in size. At 200°C, the wear mode was "large wear" due to the sample's appearance and wear rate. For "large wear", the cumulative wear mass was less (0.0327g) than graphite-on-graphite tests (average of 0.33g) but the wear scar appeared as wide as the graphite-on-

graphite wear. Also, it was noticed that the wear scar of the sample for Test 9 had a reflective wear scar, which was not observed in the other test.

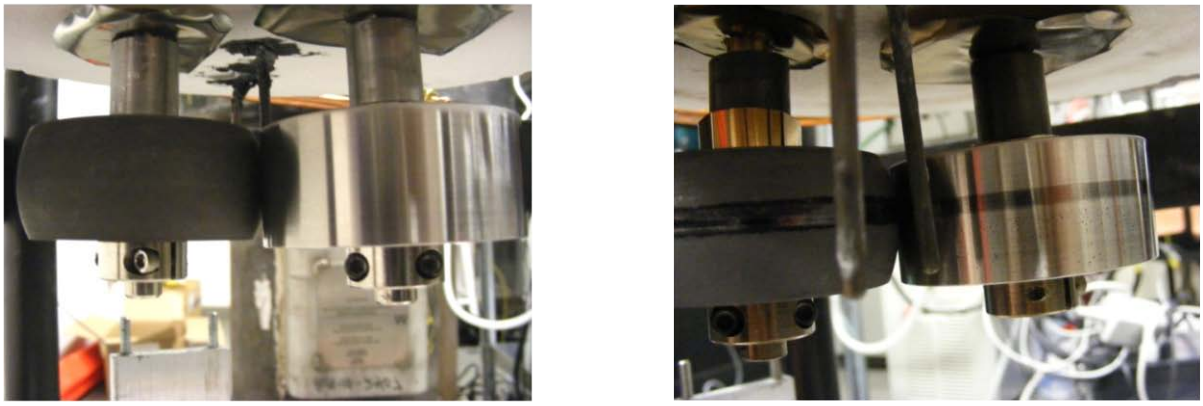

Figure 3-18. Pre-(Left) and Post-(Right) Test Sample Appearance for Graphite-on-Steel Test at 200ºC.

Graphite-on-Steel Test at 200°C (Test 9)

Graphite-on-Graphite Test at 200°C (Test 4)

Figure 3-19. Graphite Particle from Test 9, Graphite-on-Steel at 200°C and Test 4 as a Comparison

The temperature trend on wear rate for graphite-on-steel is shown in Figure 3-20 as a comparison of the result from helium tests.

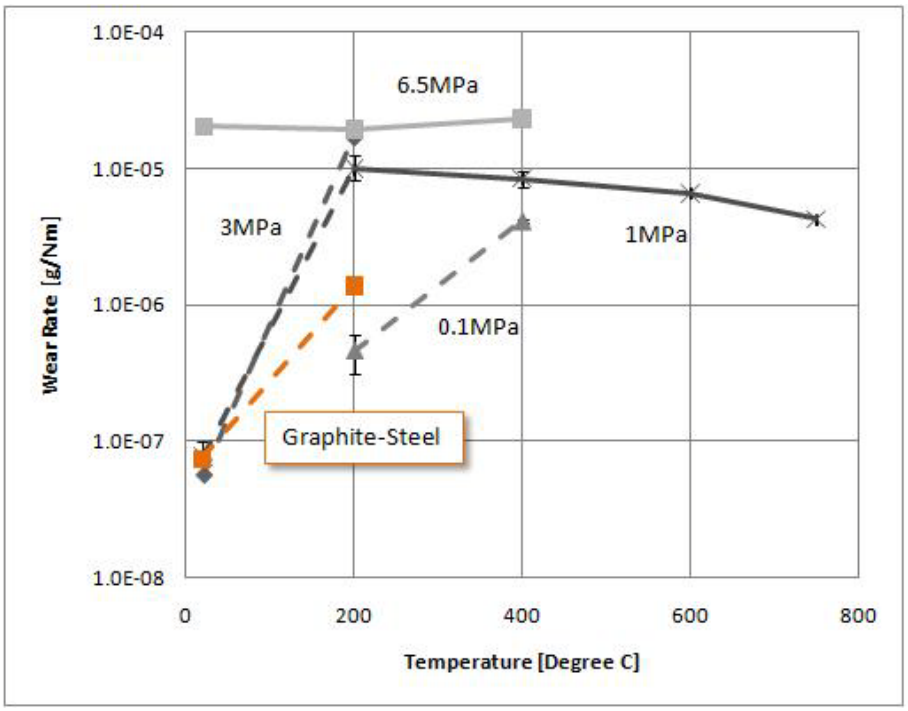

Figure 3-20. Temperature Dependence on Wear Rate with Graphite-on-Steel.

At room temperature, 20ºC, wear rate was as low as graphite-on-graphite combination with reflective wear scar. At 200ºC, the wear scar appeared as broad as "large wear", while there was less wear dust produced (0.033g) than the graphite-on-graphite test (average of 0.32g). The results for 20ºC and 200ºC tests imply that the wear mode for graphite-on-steel is "lubricated" friction for 20ºC test and "large wear" for 200ºC test. This temperature trend is similar to the graphite-on-graphite test. At 20ºC, test results agree with the result of graphite-on-graphite test at 1MPa helium pressure, both in terms of on wear rate and morphology of the graphite sample. However, there is a notable, distinct wear scar and corresponding wear dust for the 200ºC test.

The wear scar at 200 ºC was distinguished as optically reflective. The other distinctive appearance for graphite-on-steel test at 200 ºC was morphology of graphite dust (Figures 3-19). The dust from graphite-on-steel test appeared "flakier" than graphite-on-graphite test.

The SEM images of graphite dust are shown in Figure 3-21. The appearance of a particulate distribution indicates that graphite-on-steel contact yields a flakier morphology than graphite-on-graphite test. As we discussed before, the flakes have larger area-to-weight ratio than "powder" dust which is typically generated in graphite-on-graphite wear tests at lower temperature (200ºC to 400ºC).

The SEM image of graphite dust indicates that the flake type particulates are dimensionally bigger than that generated from graphite-on-graphite test. As noted before, flakes tend to adhere to the surface in contrast to the "powder dust". Thus less graphite dust is generated (collected).

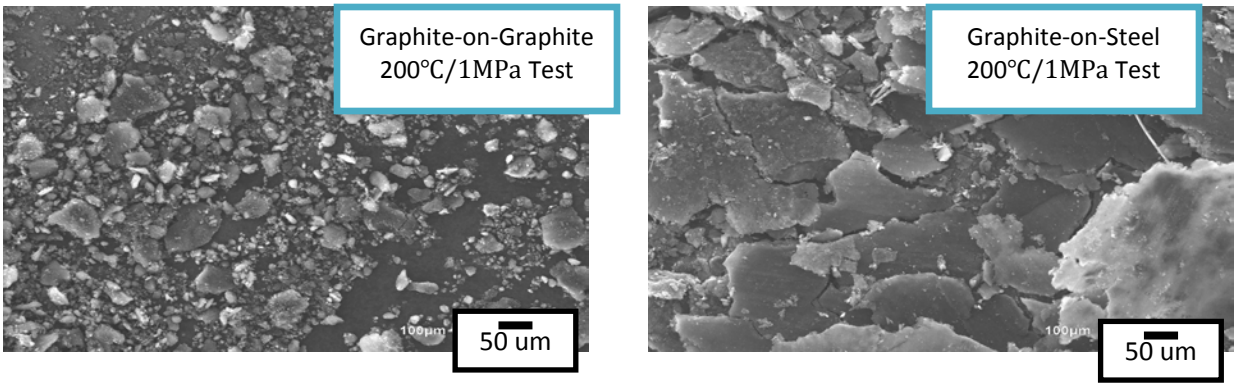

Figure 3-21. SEM image of Graphite Dust from Wear Test under 1MPa at 200°C for Graphite-on-Graphite Test (Right) and Graphite-on-Steel Test (Left).

As shown in Figure 3-18, graphite adhesion onto the surface of steel was observed. Since steel is not porous and harder than graphite, the frictional wear against a graphite surface is postulated to occur under initial frictional contact wear at the surface rather than later when particulates are present. Thus when the graphite adheres onto the steel surface, it is possible that there is no direct contact of graphite and steel, but the contact of graphite and graphite particulate adhering onto the steel surface. The graphite particulate adhesion acts as a thin lubricating film. This change in contact is thought to be a reason for smaller amount of graphite dust for graphite-on-steel tests.

3.7.2. XRD Analysis of Graphite-on-Steel Wear

The XRD pattern of graphite particulate from graphite-on-steel test is shown in Figure 3-22 and compared to the pre-test XRD pattern. As shown in the figure, the graphite-on-steel test XRD pattern shows only one evident peak for (002) plane. This means that the superficial crystallites as a result of contact between graphite and the adhered (surface) graphite changes in crystalline structure more dramatically than the graphite-on-graphite test. However, this loss of graphitized crystalline structure does not yield more graphite dust. Also, the graphite dust produced under graphite-on-steel contact would have less likelihood for be transport inside the PBR core and fuel handling system not only because of its large area-to-weight ratio but also an assumed lack of circulation of coolant. This of course depends on the actual design. Therefore, the graphite dust produced via graphite-on-steel contact is less of a concern in terms of safety than the graphite-on-graphite contact not only because of morphological change of graphite dust as noted but the confined, anticipated geometry.

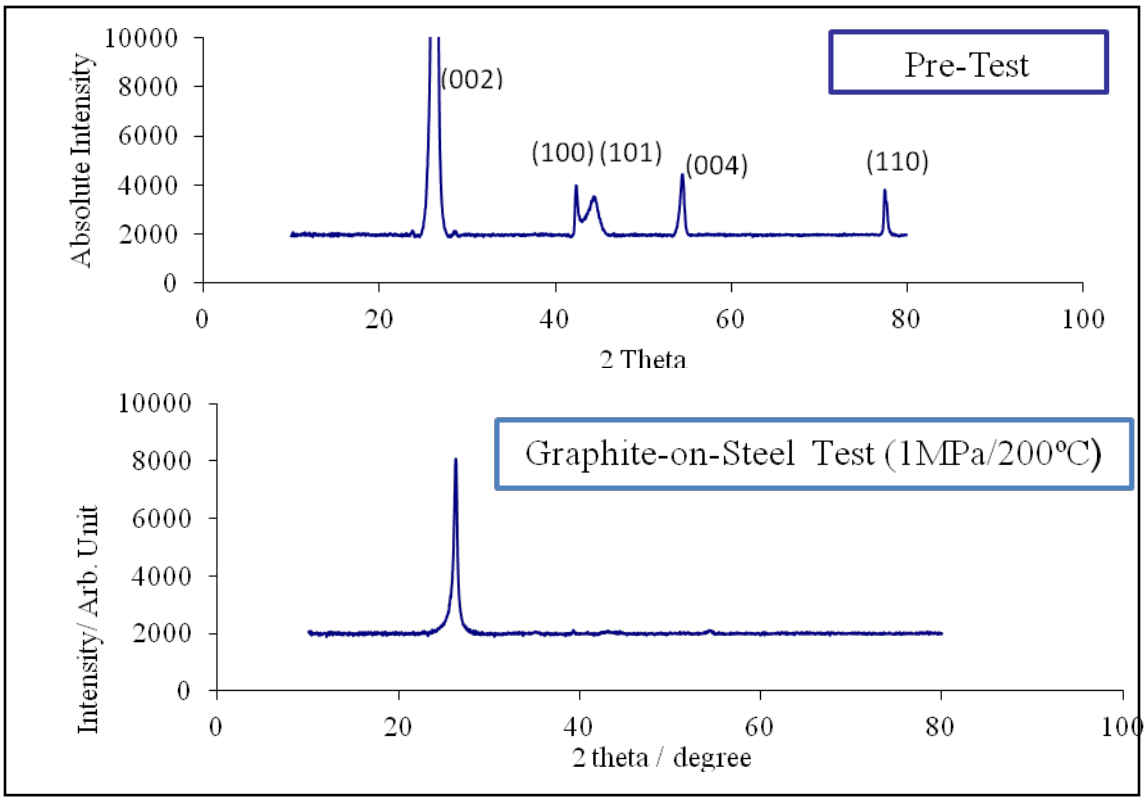

Figure 3-22 XRD Pattern of Graphite Dust from Graphite-on-Steel Test.

3.7.3. MLRF Test

Further experiments were done with a different grade of nuclear grade graphite. The tested graphite grade, MLRF, is manufactured by one of the NGNP certified graphite providers, SGL.

Tests using MLRF yielded graphite samples that had trends similar to both "lubricated" at room temperature and "large wear" at 200°C (Figure 3-23). The test at 200°C was conducted only for a short distance due to the failure of one of the sample's holding shafts (Test 25). The wear rate for the test at 200°C was calculated based on this shortened distance and recorded the greatest value from all of helium tests.

Table 3-6. Helium Test Result for MLRF.

Helium Test	Temp. (°C)	Pressure (MPa)	Load (N)	Relative Distance (m)	Wear Mass (g)	Average Wear Rate (g/N-m)	Friction
24	20.4	1	19.79	990.8	0.0013	6.78×10^{-7}	0.179
25	200	1	16.53	252.08*	0.3408	6.76×10^{-5}	0.5

* Sample holding shaft failure

20°C (Test24)

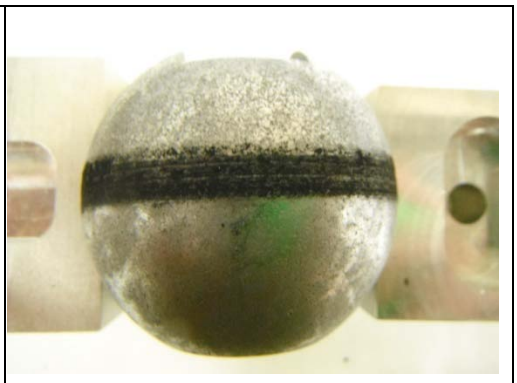

200°C (Test 25)

Figure 3-23. Sample Appearance for MLRF after wear test

As Figure 3-23 shows, the post-test surface appearance at 20ºC and 200ºC were “lubricated” friction and “large wear”, respectively. The tested graphite, MLRF, showed a temperature trend similar to IG-11, as shown by Figure 3-24. However, MLRF had a higher wear rate for both 20ºC and 200ºC tests. As discussed, the graphite dust is generated from gradual surface wear from frictional contact between graphite samples. Further, Rostamian found that the graphite wear depends on the asperity level (Rostamian, 2012). The asperity level is dependent on the material properties and surface finish, thus on the manufacturing process. The properties for IG-11 and MLRF are different due to different manufacturing processes. One difference between IG-11 and MLRF is the material density; this is related to grain size at the surface (MLRF has a larger grain size (at <1000μm) than IG-11 (at 20 μm)). With larger surface grain size, the surface wear may yield more graphite dust when frictional contact forces are imposed. This depends on the proprietary ‘binder’ and the ‘bake-in’ process that may be used in the manufacturing process. This defines the initial porosity and interconnected solid phase. Since the temperature trend was similar for both MLRF and IG-11, the wear phenomenon is similar. This means the wear mode transition from “lubricated” friction to “large wear” also occurs for MLRF, in a manner similar to IG-11 under the similar condition.

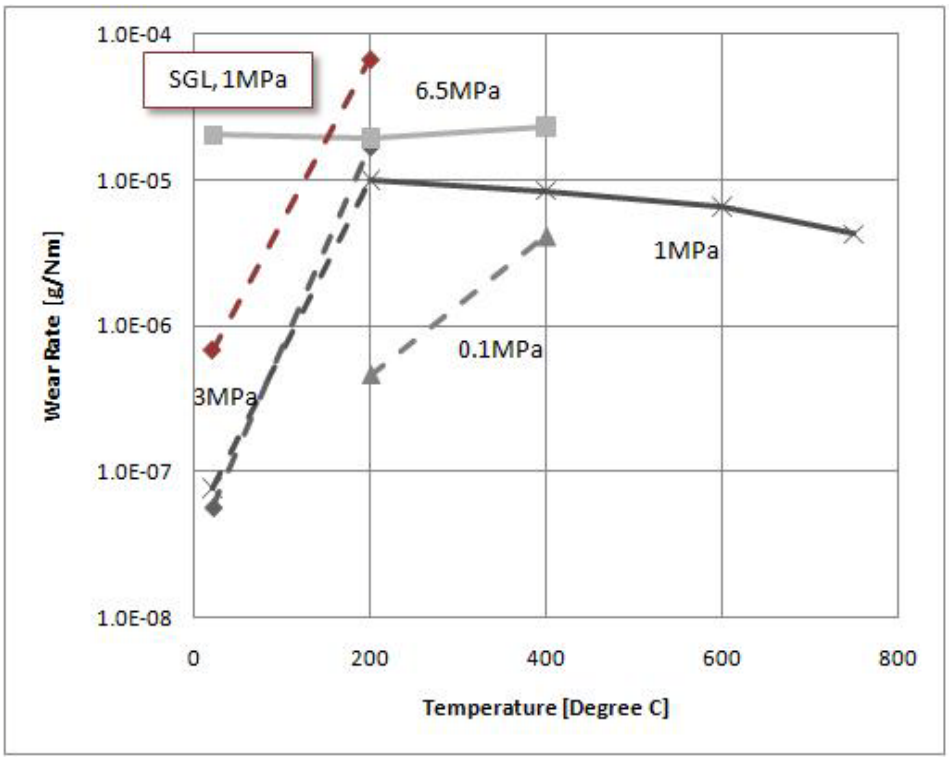

Figure 3-24. Tempreature Dependence on Wear Rate for SGL Test with Comparison of IG-11.

3.8. Conclusion for Chapter 2 and 3

The pebble bed reactor (PBR) is one type of graphite-moderated gas-cooled reactor (GM-GCR); the Very High Temperature Reactor (VHTR) has been considered under the Next Generation Nuclear Plants (NGNP) program. Unlike most reactors, PBRs have an online refueling system. Further they use spherical graphite pebbles (approximate 6cm in diameter) with fuel kernels embedded as fuel elements. The graphite pebbles are dropped into the top of the reactor, gradually traverse randomly down through the reactor core, and are removed from the bottom. The removed graphite pebbles are then either lifted to the top of the reactor core if the assessed burn-up is low, or relegated as spent fuel if sufficiently burned or assessed as defective. The motions of these graphite pebbles and the frictional contact in the bed produce graphite dust. Graphite dust particles carrying adsorbed leaked fission products may be of particular safety concern in a depressurization accident because they can then escaper out of the primary system. A potential graphite dust explosion in an air-filled confinement building can exacerbate dispersion of fission products. Thus, the safety concerns must be understood for PBR plant design and licensing.

In Chapter 2 and 3, we summarized experimental results on wear tests using nuclear grade graphite in frictional contact under conditions of helium pressure and temperature of relevance to the VHTR/NGNP; that is , from 0.1 to 6.5MPa, up to 750ºC.

The wear tests with a purposely designed test apparatus showed that it was possible to conduct wear tests under desired conditions within acceptable uncertainties. The wear tests under higher helium pressure (1 to 6.5MPa), at higher temperatures (200° to 750°C) revealed that there were two distinct wear modes. One mode was characterized as “large wear”, the other mode “lubricated” friction. The wear characteristic under “lubricated” friction agreed with limited previous experimental studies under lower helium pressure (0.014 to 0.1MPa). In contrast, “large wear” showed a larger wear rate (average of 1.37×10-5g/Nm) than the “lubricated” friction mode (average of 1.93×10-7g/Nm). The post-test wear

scar appeared as an optically reflective, flattened surface for “lubricated” mode and degraded, optically dull surface for “large wear” mode. These wear modes were additionally characterized by Scanning Electron Microscope (SEM) images. X -Ray Diffraction (XRD) analysis of the pre- and post-experiment graphite. SEM/XRD images showed that there was a loss of well-organized crystalline structure due to frictional contact under higher helium pressure (1 to 6.5MPa), at higher temperature (200° to 750°C). The estimated uncertainties of experimental data in this study were estimated to be satisfactorily small enough such that the influence of temperature and pressure on friction could be discerned.

4. Computational modeling and predictions of frictional contact wear

Computational modeling and simulation of the contact mechanics, as anticipated in a PBR configuration, was carried out for the purpose of predicting the amount of dust generated during anticipated full power operation year of a PBR. A methodology that encompasses finite element analysis (FEA) and micromechanics of wear is developed to address the issue of dust production and its quantification. In particular, the phenomenon of frictional wear and change in wear rate with sliding (contact) length was investigated by Rostamian (2012).

This work studied the wear properties of graphite by simulating pebble motion and interactions of a specific type of nuclear grade graphite, IG-11. This study consists of two perspectives: macroscale stress analysis and microscale analysis of wear mechanisms. The first is a set of FEA simulations considering pebble-pebble frictional contact. In these simulations, the mass of generated graphite particulates due to frictional contact is calculated by incorporating FEA results into Archard's equation, which is a linear correlation between wear mass and (contact) wear length. However, the experimental data by Johnson (2012) revealed that the wear rate of graphite decreases with sliding length. This is because the graphite material is porous and thus, the surfaces in contact experience frictional wear over time, which results in a gradual decrease in wear rate as the surface morphology changes. In order to address the change in wear rate, a more detailed analysis of wear mechanisms at room temperature was presented since thermophysical properties of high temperature graphite are incomplete. In this 'microscale' study, the wear behavior of graphite at an asperity level is studied by simulating the contact between asperities of facing surfaces. By introducing the effect of asperity removal on wear rate, a nonlinear wear rate is obtained.

The nonlinear wear law proposed in this study serves as a model to predict the effect of changing surface topology on the wear behavior of graphite. This tribological model is valid for applications where mass removal is in the form of powder formation rather than flake or chip formation.

4.1. Introduction and scope of computational prediction of dust production

This chapter describes the wear mechanisms of graphite pebbles frictional contact. The preliminary computational simulations are finite element simulations of frictional contact between two graphite pebbles. The range of inter-pebble forces are presented by Cogliati and Abderrafi (2008) calculated by PEBBLES code. This study comprises of two stages; macro-level considerations and micro-level considerations. The first stage is a set of finite element simulations considering pebble-pebble frictional contact. In these simulations, the generated graphite particulate due to frictional contact is calculated using the commercial finite element code ABAQUS (2010) and the linear Archard's equation (Archard, 1956). The Archard's equation leads to linear results as expected. However, the experimental observations reveal that wear rate of graphite decreases with sliding length. As a result, the second stage of this work was a more realistic analysis of the wear mechanisms leading to wear of graphite at room temperature. Wear behavior of graphite at the asperity (surface imperfection) level was studied by simulating the contact between two asperities of facing surfaces. By introducing the effect of asperity removal on wear rate in the form of an 'asperity height function', a nonlinear wear rate is calculated. A fit of the asperity height function with the computational wear variations results in a power law formulation for wear. These FEA simulations serve as a ground for developing an asperity contact model to describe the nonlinear wear effects as experimentally observed by Johnson (2012).

There have been several efforts to develop codes to model the dust-related phenomena inside a pebble bed reactor including dust generation, lift-off, transportation through the main circuit, dust

coagulation, chemical interaction with radio-nuclides, and deposition. A representative list of these dust prediction models is presented in Table 4.1.

Table 4-1. Dust Prediction System Codes.

Codes	Phenomena Modeled (Dust Related)	Reference
Dust and Activity Migration and Distribution model	Dust generation, Lift-Off and Deposition	HTGR, 2010
SPECTRA: Radioactive Particle Transport Package	Fission Product and Dust Transport	Stempniewicz, 2012
PEBBLES	Dust Generation in Core	Cogliati, 2008

The 'Dust and Activity Migration Model' models the integrated effects using correlations derived from the measurements on the AVR. The SPECTRA code was developed to have the Radioactive Particle Transport Package in an effort for licensing consideration of smaller, advanced reactor concepts. The SPECTRA code, however, is used in the Westinghouse NGNP consortium for the analysis of dust and fission product transport in the U.S. DOE NGNP program (Stempniewicz, 2012) and can be used for HTGRs in general. The PEBBLES code is a discrete element method code, which simulates the forces and relative velocities of the spherical elements (fuel and non-fueled) inside the core. The code estimates the overall dust production in the core by the use of the Archard wear equation, which is a first order approximation of the overall wear rate (Cogliati, 2010).

4.2. Initial Finite Element Simulations

4.2.1. HS and BCC configurations

In an effort to computationally simulate pebble-pebble frictional contact, a finite element model of contacting pebbles has been created in ABAQUS. Two different configurations have been considered: (1) the HS model, which refers to two HemiSpheres in contact (Fig. 4.1a), and (2) the BCC model (Fig. 5.1b), which is the Body Centered Cubic model. In the BCC configuration, one pebble is in the center of a cube and can be in contact with eight corner spheres of this unit cube. In Fig. 4.1b, a symmetric portion of the BCC model is represented. Dynamic simulations were conducted with realistic pebble-pebble forces (Cogliati, 2008), friction at contact points and rotation of the center pebble. A mesh refinement study was performed to ensure mesh independent results, and to determine the optimum mesh size in the contact regions between pebbles.

Graphite was modeled as an elastoplastic material using a von Mises isotropic plasticity modeled with nonlinear hardening, coupled with a linear wear model to determine the worn mass per pebble pass. Finally, the results were discussed and compared with those in (Lou, 2005) and (Cogliati, 2008).

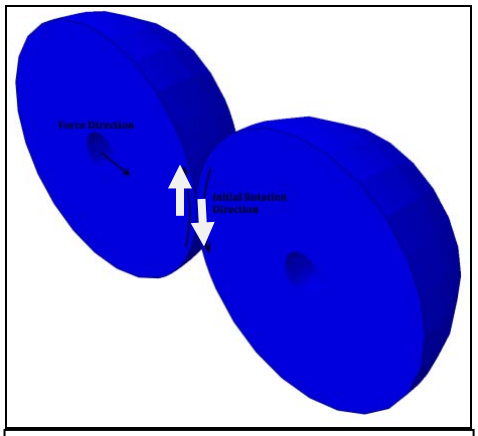

Above, the direction of force is from left to right sphere and arrows show the initial rotational directions. At right, the direction of force from the 'middle' sphere is to the right, against both spheres.

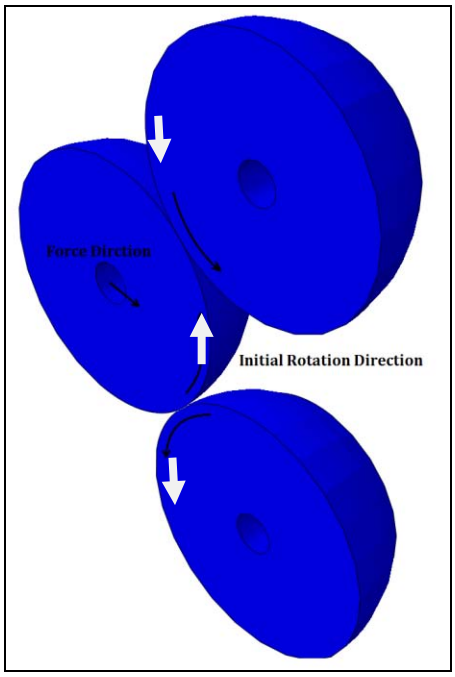

(a) (b)

Fig. 4-1. Pebble-pebble contact in (a) HS and (b)BCC configurations.

4.2.2. Stress/Strain Curve for IG-11

The nuclear grade graphite IG–11 with an elastoplastic behavior is considered to determine the extent of pebble wear due to contact and wear forces. For IG-11, the Young's modulus and the Poisson ratio are reported as E=9.8GPa and ν =0.126 (Yokoyama, 2008). Other values are reported for the Young's modulus in different sources, e.g. E=9.5GPa (Yoda, 1983). In this work, the value of 9.8*GPa* was used because it is accompanied by a stress-strain graph shown in Fig. 4.2. As observed in this Fig.4.2, IG-11 exhibits plastic deformations of almost 4% at room temperature.

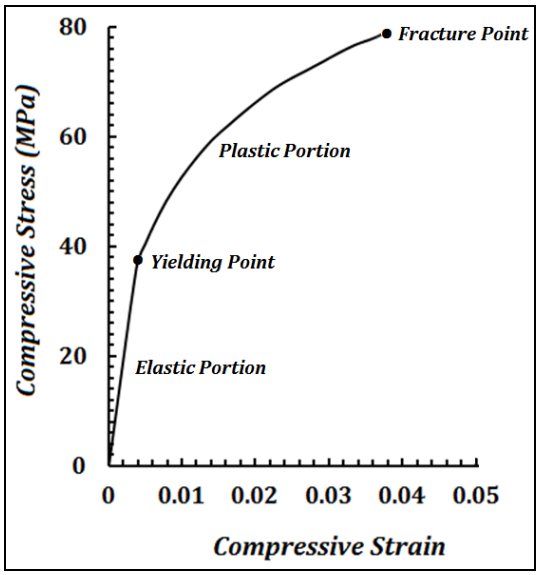

Fig. 4-2. Stress-strain curve for IG-11 (Yokoyama, 2008).

The yield stress and the corresponding plastic strains are obtained from the plastic portion of the stress-strain curve (Fig. 4.2). Table 4-2 shows the values used in ABAQUS as the equivalent stress-strain curve and the plastic model used in the FEA simulation.

Table 4-2. Isotropic Plasticity Model Data.

Yield Stress (MPa)	Plastic Strain
45,005,500	0
48,779,700	0.0015747
53,811,900	0.0040155
58,765,500	0.0066925
63,247,300	0.0099206
67,414,600	0.0136999
71,739,100	0.0185028
74,962,900	0.0230694
77,557,600	0.0271636
79,287,400	0.0309429

4.2.3. Simulation Setup

As noted, the simulation setup consists of two configurations for pebble-pebble contact: a simple model of two hemisphere (HS) and a body centered cubic (BCC) unit cell configuration. The latter represents a more realistic configuration of pebble conditions in contact with 5 pebbles, which is an average coordination number for a pebble in the porous bed of a PBR (du Toit, 2009). In the present work, however, the maximum number of contact points is 2. The number of contact points was chosen based on the defined loading. The target pebble pushes against the other two pebbles on the right hand side, as shown in Fig. 4.1b. If the number of contacts were chosen as 5, this loading would not affect the extra pebbles on other side of the central pebble, which are not shown in the model.

A set of simulations was carried out by considering the inter-pebble forces, friction at contact points and rotation of the pebbles in order to study the contact stresses. Each simulation modeled a rotation corresponding to 2.06m of relative movement of the contact points. This is an estimation predicted in (Lou, 2005) for the HTR-10 in China. This wear length corresponds to 10.92 revolutions.

The contact normal forces in the contact region are used to calculate the wear. Therefore, simulating the contact in a small portion of the pebble is sufficient to compute the amount of material removed from the pebbles by wear and to encompass the entire contact region. On the other hand, by simulating only a small portion of the relative motion between the pebbles, computational costs are greatly reduced. As a result, a reciprocal rotation of the pebbles is considered. This reciprocal motion will be discussed and presented as finely meshed zone in Fig. 4.3.

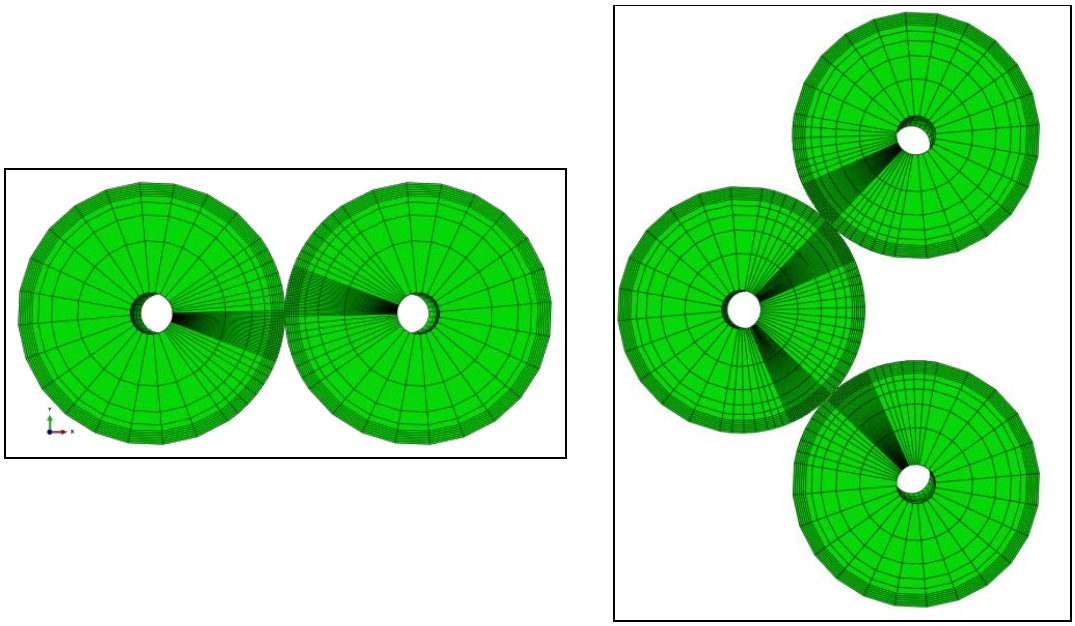

(a) (b)

Fig. 4-3. Contact zone refined mesh for (a) HS and (b) BCC models.

4.2.4. Element Selection and Assembly Setup

Linear hexahedral 3D stress elements (C3D8R) with reduced integration have been used to mesh the geometry. Reduced integration usually means that an integration scheme one order less than the full scheme is used to integrate the element's internal forces and stiffness. Superficially this appears to be a poor approximation, but it has proved to offer significant advantages. For second-order elements, in which the isoparametric coordinate lines remain orthogonal in the physical space, the reduced-integration points have the Barlow point property (Barlow, 1976); that is, the strains are calculated from the interpolation functions with higher accuracy at these points than anywhere else in the element. For first-order elements, the uniform strain method yields the exact average strain over the element volume. Not only is this important with respect to the values available for output, it is also significant when the constitutive model is nonlinear. This is because the strains passed into the constitutive routines are a better representation of the actual strains.

Reduced integration decreases the number of constraints introduced by an element when there are internal constraints in the continuum theory being modeled. These constraints are incompressibility, or the Kirchhoff transverse shear constraints if solid elements are used to analyze bending problems. In such applications, fully integrated elements will “lock”—they will exhibit response that is orders of magnitude too stiff, so the results they provide are quite unusable. The reduced-integration version of the same element will often work well in such cases.

Finally, reduced integration lowers the cost of forming an element. For example, a fully integrated, second-order, 20-node 3D element requires integration at 27 points, while the reduced-integration version of the same element only uses 8 points and, therefore, costs less than 30% of the fully integrated version. This cost savings is especially significant in cases where the element formation costs dominate the overall costs. The deficiency of reduced integration is that, except in one dimension and in axis-symmetric geometries modeled with higher than first-order elements, the element stiffness matrix will be ranked deficient. This most commonly exhibits itself in the appearance of singular modes (“hourglass modes”) in the response. These are nonphysical response modes that can grow in an unbounded way unless they are controlled.

Considering symmetry, half-spheres were considered to be initially in contact at one point. Like any actual node on the solid continuum elements in the model, boundary conditions, constrains and loads can be assigned to reference points. The advantage of using reference points is to apply loads and boundary conditions to specific surfaces or nodes of the model using constraints.

Two reference points were assigned at the center points of the half-spheres. These reference points apply the rotation boundary conditions to the model acting as a rotating shaft on the axis of the spheres. Two other reference points are chosen on the axis of the spheres for assigning stationary boundary conditions, i.e. boundary conditions which constraint the spheres from moving up and down. These latter nodes are also used for translational boundary conditions.

4.2.5. Non-linear Analysis

Each analysis step is associated with a specific procedure that defines the type of analysis to be performed during the step, such as a static stress analysis or a transient analysis. One can change the analysis procedure from step to step in any meaningful way, so this gives great flexibility in performing analyses. Since the state of the model (stresses, strains, temperatures, etc.) is updated throughout all general analysis steps, the effects of previous history are always included in the response for each new analysis step.

For each step in the analysis one can indicate whether ABAQUS will account for nonlinear effects from large displacements and deformations and also the nonlinearities due to contact mechanics complexities. If the displacements in a model due to loading are relatively small during a step, the nonlinear effects may be small enough to be ignored. However, in cases where the loads on a model result in large displacements, nonlinear geometric effects can become important. The *Nlgeom* setting for a step determines whether ABAQUS will account for geometric nonlinearity in that step. In the present work, due to high nonlinearity of the spherical geometry of the contacting pebbles, *NLgeom* has been used in all steps.

Also, it has been found through observation of multiple simulations that in the case of large displacements (high nonlinearity), steps of relatively larger step times can lead to unrealistic deformations and irrecoverable distortions. This usually causes the solution not to converge.

Here, based on a mesh verification capability of ABAQUS/CAE, element failure criteria are checked. One of these criteria is the maximum stable time increment for the desired nonlinear analysis. This maximum stable time determines the minimum time increment size of each step. In case of multiple steps, the consistency of the minimum time increment size is a necessity.

4.2.6. FEA Results and Discussions

In this section, the von Mises stress contours and contact normal forces are illustrated and discussed. Finally, an estimate of the mass removal from the surface of graphite pebbles is given. The results are then compared to those in (Luo, 2005 and Cogliati, 2008). In these works, dust production results are obtained for HTR-10 and AVR, both pebble bed reactors. HTR-10 is a 10 MWt nuclear reactor, which uses 27,000 nuclear graphite pebbles (IG-11) as the moderator with a pebble pass rate of 125 pebbles per day. AVR was the first pebble bed reactor 46 MWt (1967-1988), which used 100,000 graphite pebble moderators of 14 different types with a pebble pass rate of 400 pebbles per day.

Considering the wear length of 2.06 meters for HTR-10 pebbles (Lou, 2005) and the resultant 10.92 revolutions, simulations were conducted. In Fig. 4.4, the stress contours are shown at different angles of rotations during the reciprocal movement of the contacting pebbles for the HS configuration. The stress contour changes in time indicate that the two pebbles are rotating about their axes back and forth forming a reciprocating angular rotation against each other (Fig 4.4). The average stress values of all the nodes on an element face at the contact region are multiplied by the surface area of the element

face to produce contact normal force on each node, which are exported in the post processing section, ABAQUS/Viewer.

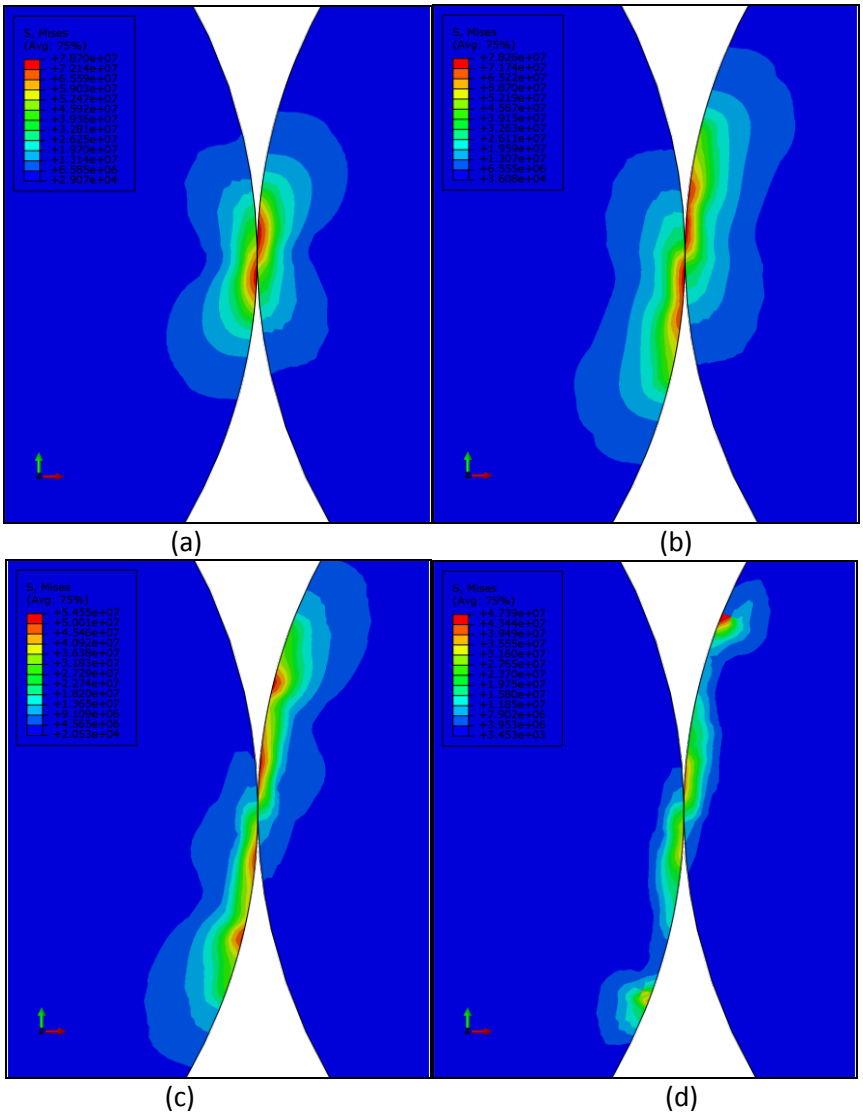

Fig. 4-4 The Von Mises stress contours at contact region for HS model at rotation angles as follows: (a) 1°, b) 10°, (c) 15° and (d) 20°.

In Figs. 4.5 and 4.6, the stress contours at the lower and upper contact regions are shown at different angles for the BCC model, respectively. Comparing the stress values at contact points in Figs. 4.5 and 4.6, it is observed that the lower contact point has a higher stress than the stress at the upper contact point. As a conservative approach, the wear mass is calculated considering the simulation results from the lower point, which has a higher stress and normal forces.

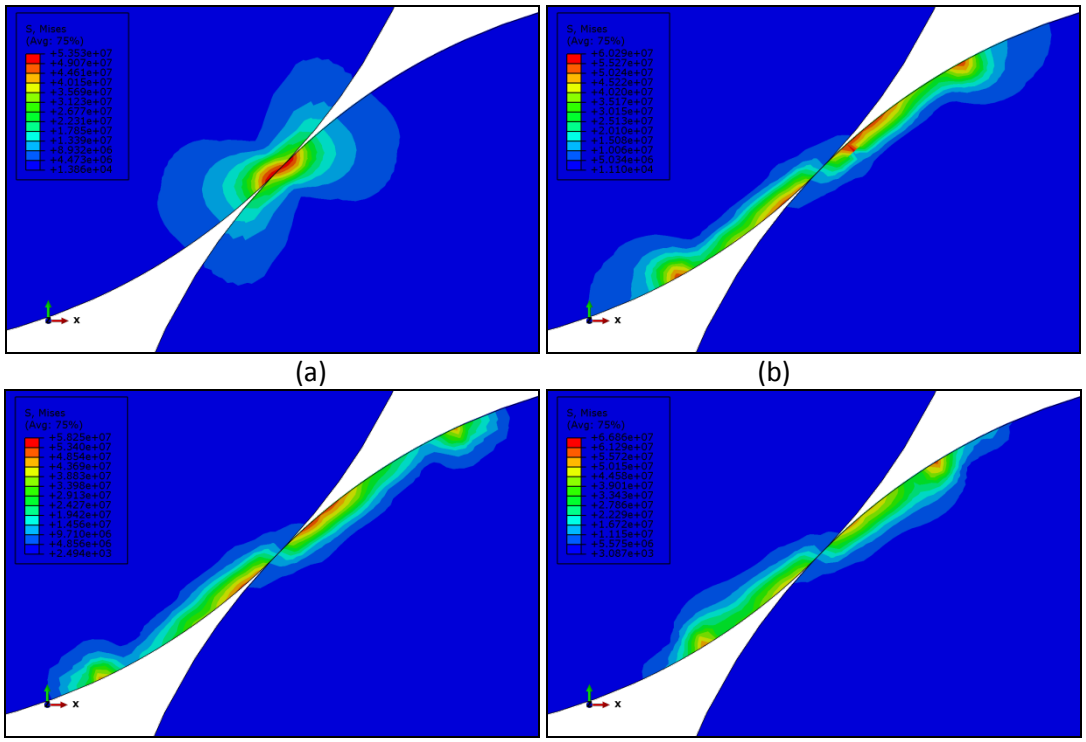

(a) (b)

(c) (d)

Fig. 4-5 The Von Mises stress contours at lower contact region for BCC model at rotation angles as follows: (a) 1°, b) 10°, (c) 15° and (d) 20°.

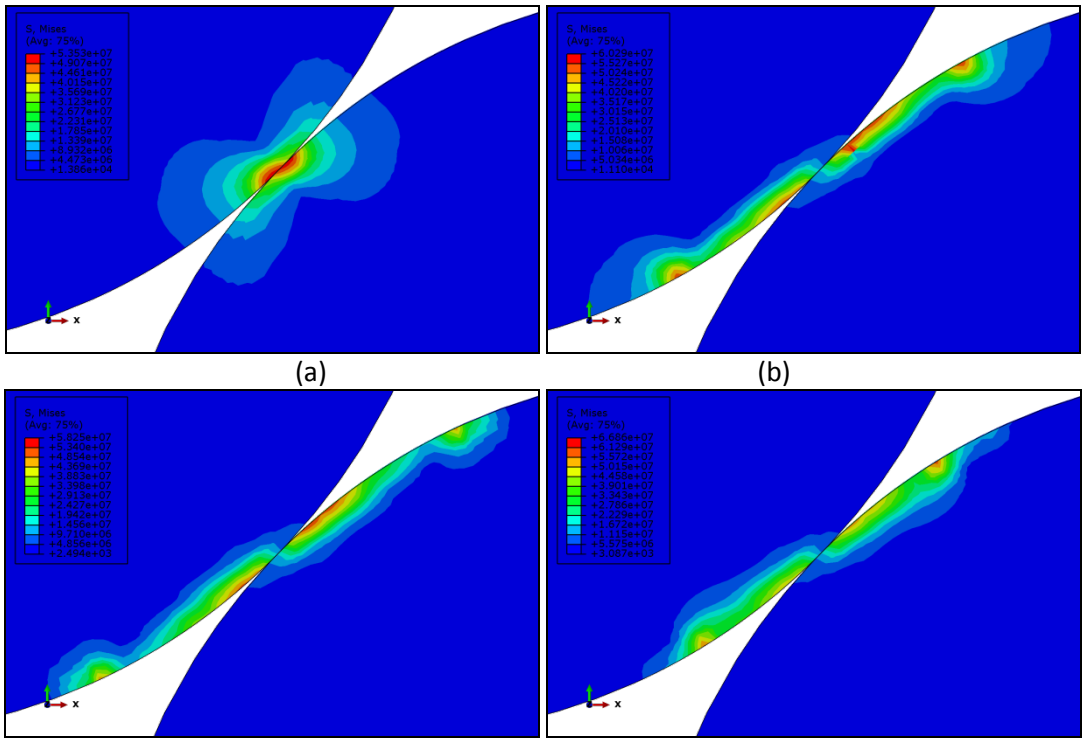

(a) (b)

(c) (d)

Fig. 4-6 The Von Mises stress contours at lower contact region for BCC model at rotation angles as follows: (a) 1°, b) 10°, (c) 15° and (d) 20°

In the BCC configuration, the difference between in von Mises stress of the upper and lower contacts can be explained by their direction of rotation with respect to the direction of translation of the center pebble. The arrows in Fig. 4.7 indicate that pebble 1 tends to make its way between pebbles 2 and 3. Pebble 2 rotates in a direction that allows a smoother translation for pebble 1 although frictional forces are acting on the two pebbles. At the same time, pebble 3 rotates in a direction which is opposite to the direction of the translation of pebble 1.

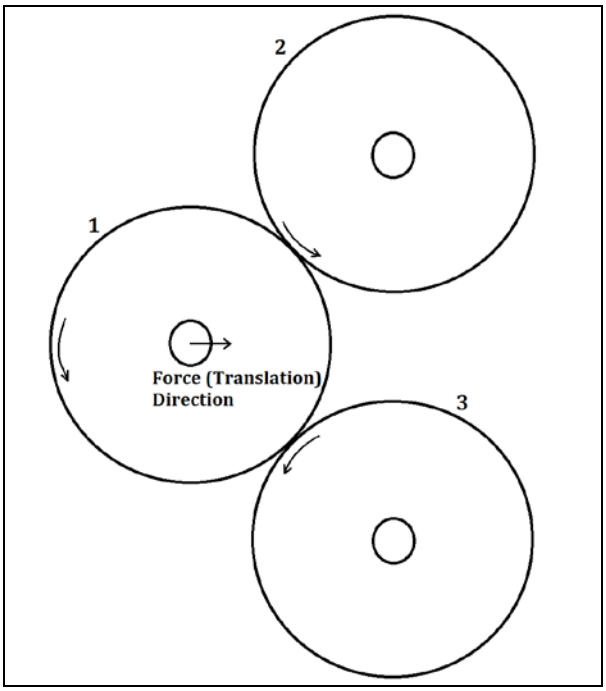

Fig. 4-7. Difference between the interactions between pebble pais 1-2 and 1-3.

In Fig. 4.8a, the contact normal force contours at the contact regions are shown at two nodes on the HS model. In Figs. 4.8b and 4.8c, the contact normal forces contours are illustrated for the upper and lower contact points in the BCC model, respectively. The upper and lower on the BBC configurations are presented in Fig. 4.7. The blue area is the region in which the contact interactions and properties are defined. As presented in Figs. 4.8b and 4.8c, the lower point shows a higher normal force. As explained in Fig. 4.7, this is due to the fact that the lower point on has a higher friction as a result of its rotation as compared with the upper point.

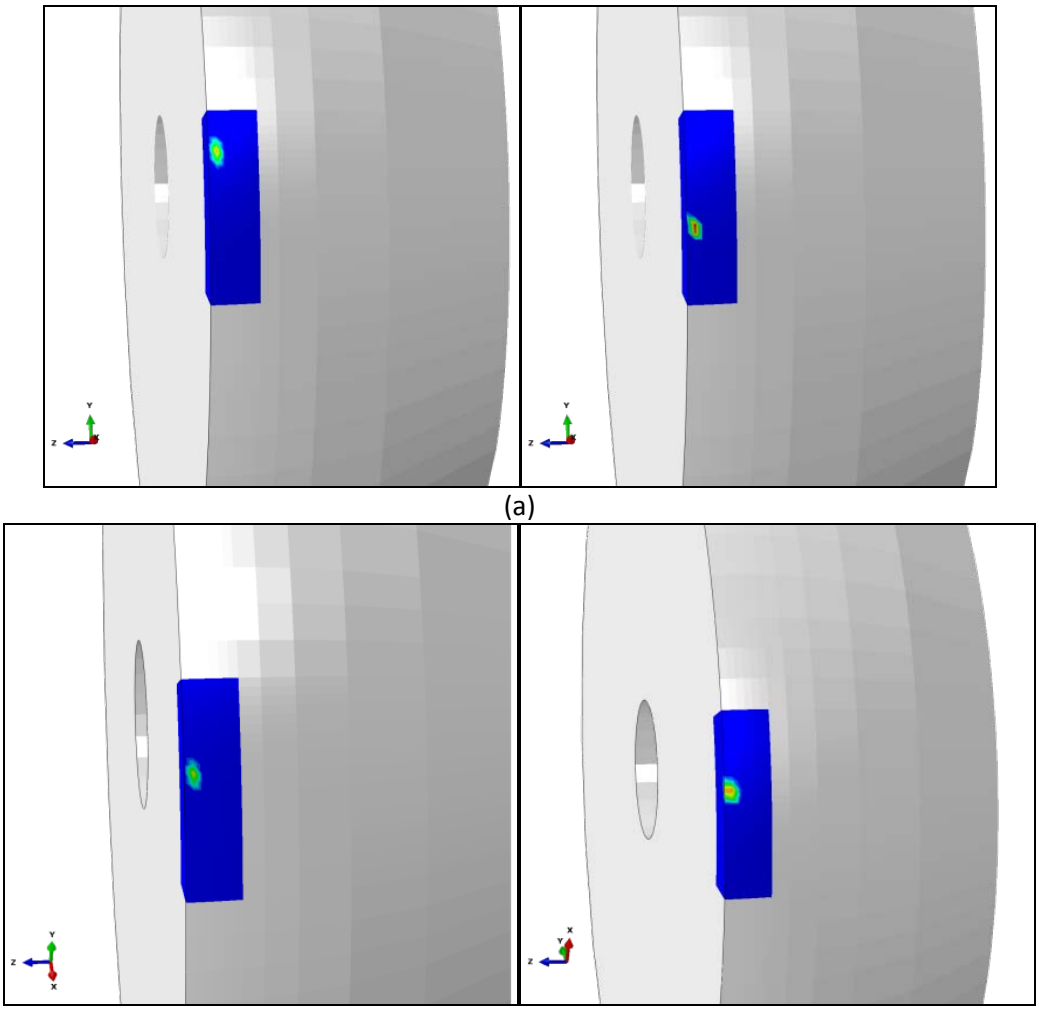

(a)

(b) (c)

Fig. **4-8. Contact normal force contours at one node of the contact region for (a) HS, (b) BCC-upper contact and (c) BCC-lower contact.**

It is seen that the difference between the normal forces is only 1%. Therefore, as a conservative approach, the normal force of the lower point in the BBC configuration is chosen for wear analyses as conducted in Chapter 4.3.

4.3. Wear Simulations

4.3.1. Damage by Micro-structural Changes

The formation of wear particles is usually considered as being determined by an attainment to a critical situation. The critical situations may be governed by strain parameters in the models of plasticity-dominated wear or by fracture parameters for brittle-dominated wear. For graphite as brittle materials (ceramics, glasses, hard coating and others), wear particle formation is controlled predominantly by fracture of surface layer and therefore may be described by fracture mechanics approach.

Several micro-mechanisms lead to a cumulative effect on a macro-scale known as surface damage. In the first case (mesoscale), the damage is ‘ductile damage’ if it is nucleation and growth of cavities under static loading. It is ‘creep damage’ when it occurs at elevated temperatures. It is ‘low cycle

fatigue' when the test sample is under repeated high level loadings. In the second case (micro-level), it is called brittle failure, or quasi-brittle damage, when the loading is monotonic; it is called high cycle fatigue damage when the loading is a large number of repeated cycles.

Sustained load cracking is more predominant than cyclic fatigue effects, due in part to the very limited crack-tip plasticity of ceramics and other highly brittle materials. Highly brittle materials have strong covalent or ionic bonding, which essentially limits any obvious mobility of point defects and dislocations (Lemaitre, 2005).

4.3.2. Archard's Wear Equation

The descriptions of the wearing process show that this process involves many variables, few of which have been researched sufficiently to formulate wear equations that can be used by designers. Some wear equations can be found in the literature, but none can be generally applied. The most widely publicized equation is the Archard's wear equation (1965), in which the rate of wear, ($\dot{V}$, volume per unit of time), is:

$$\dot{V} = K.\frac{F\dot{L}}{H} \tag{4.1}$$

where K is a constant referred to as 'wear coefficient', F is the applied load, $\dot{L}$ *i*s the sliding speed and H is the hardness of the softest of a pair of the material. Clearly, neither this equation nor any other published equation can adequately describe what occurs in wear. However, this equation is widely known, and values of k for various materials are increasingly found in the literature. These numbers serve as broad guidelines for anticipated wear rates of materials, just as do published values of coefficients of friction. However, designers need coefficient values of high reliability within a range of ±20% or better in order to design acceptable systems.

Most engineers are certain that one or more wear equations exist that are more applicable to their problem than is suggested above. This belief arises from the existence of good equations in most other topics in engineering; there are equations for the bending of beams, the electrical resistance of materials, the rate of heat transfer, and the natural frequency of vibration of machinery, etc. These are relatively simple phenomena, however, governed by very few variables. Adhesive wear, on the other hand, involves several variables (Blau, 1992). Some of which can be measured easily and others of which are difficult or impossible to measure. It should be emphasized that there is no equation which can be generally applied.

In fact, there are many practical situations in which the published equations lead to erroneous conclusions. For example, cam shafts in auto engines are not fully hardened because in that state they wear far too fast; some brake materials wear faster at low speeds than at high speeds; some hardenable steels wear faster at low sliding speed than at high sliding speed; and graphite wears at a higher primary rate, which decreases with sliding length. It is therefore important not to rely on any specific equation without considerable simulative testing. In testing, it is very important to characterize the sliding system thoroughly, including factors such as stiffness of the system, vibration modes, and atmospheres surrounding the test. However, the characterization of the system is inadequate because it may involve errors. The most accurate method of determining whether a laboratory test truly simulates a mechanical component under study is to verify that the progression of surface change (wear rate, friction, appearance) and the wear debris are identical or nearly identical.

In the present work, an average dust estimate of 0.094 mg per pebble pass results in an average dust of 3.5g/yr for HTR-10. Using the above approximation, an estimate of 41.5 grams of dust per full working year is predicted for the AVR. This is while in the AVR, 3 kg of dust was accumulated for a full working year in filters (Moormann, 2009). In the AVR, the helium outlet temperature was 950°C, but fuel temperature instabilities occurred during operation with extremely high local temperatures

(Moormann, 2009). As a consequence the whole reactor vessel became heavily contaminated by Cs-137 and Sr-90.

In this work, the frictional contacts between pebbles as anticipated in a pebble bed reactor are simulated to predict the potential dust generation in PBR reactor core. The prediction of graphite dust generation gains its importance under air ingress accidents at elevated temperatures. The present graphite dust estimate supports the notion that the dust which was generated and accumulated in AVR was a consequence of various frictional mechanisms. However more considerations into the present work can lead to better estimates for dust generated in pebble bed reactors.

4.4. Micromechanics of Wear

Since the real surface of contact is the peak of in-contact asperities, the likely form of wear on graphite surface is assumed to be powder formation; that is, dislodging of the asperities. This is also seen in the experiments carried out by Johnson (2012). In these experiments, it has been shown that powder is formed and accumulated on collection tray after a long sliding (~1000m) distance at room temperature. In this section, the SEM images of dust are analyzed to examine the validity of the assumption of powder formation. Next, an analytical 'asperity height model' is introduced to account for the change in wear rate with sliding length as the result of asperity height decrease. Finally, a set of finite element simulations considering the contact of asperities is performed in order to calculate the constants of the analytical 'asperity height model'. The wear results from computational predictions are compared to the experimental results for verification purposes. The surface is made of two segments which are a rough surface and a smooth surface. It is expected that the material of a rougher surface has a higher wear volume after a certain sliding distance. The wear ring around the pebbles is seen to have been smoothed after the pebbles have been in contact (see Fig. 4.12). Therefore, by a closer examination of the Archard wear model, we attempt to assess the dependence of wear volume on the asperity height.

4.4.1. Proposed Wear Equation Correlation

Based on the micro-level consideration above, we consider the volumetric wear rate form of the Archard equation:

$$\dot{V} = K\frac{F\dot{L}}{H} \tag{4.1}$$

Introducing the asperity height into this equation, we approximate the volume by $V \approx hA$:

$$-\dot{h}A = K\frac{F\dot{L}}{H} \tag{4.2}$$

where, A is the contact area, assumed to be constant. The negative sign denotes that the time rate change of asperity height is negative, representing a decrease in asperity height with time. It should be noted that the constant contact area can vary based on the component shape and the contact configurations.

In order to generalize this equation in terms of the contact area, we consider the contact stresses instead of normal forces. Then, Eq. (4.2) takes the form:

$$-\dot{h} = K\frac{P\dot{L}}{H} \tag{4.3}$$

where, P is contact stress. By performing computational simulations in ABAQUS, contact stresses can be easily obtained at each node in the mesh (Rostamian, 2012).

In Eq. (4.3), L is sliding distance rate or relative velocity at contact. However, the time rate of change in the asperity height, $\dot{h}$, is unknown. To eliminate this unknown, we consider:

$$h = h(t) = h\left(L(t)\right) \tag{4.4}$$

which denotes that the dependence of asperity height on time can be formulated as the dependence of asperity height on wear length. Note that, the gas adsorption effects on graphite surface are not considered. In order to find $\dot{h}$, we take the partial derivative of h with respect to time:

$$\frac{dh}{dt} = \frac{dh}{dL}.\frac{dL}{dt} \Rightarrow \dot{h} = \frac{dh}{dL}.\dot{L} \Rightarrow \frac{\dot{h}}{\dot{L}} = \frac{dh}{dL} \tag{4.5}$$

Substituting Eq. (4.5) into Eq. (4.3) yields,

$$-\frac{H}{P}\frac{dh}{dL} = K \tag{4.6}$$

This is still a linear equation for the rate of change of the asperity height. However, it can now be argued that the asperity height, which decreases with the sliding length, can start to influence the material constant K . This material property is commonly considered as a constant when the Archard's equation is implemented for wear calculations. In this work, we introduce a function, which take into account the effect of asperity height variations. This function incorporates the effect of asperity height decrease into the linear Archard wear model for higher sliding distances. When the asperity height decreases from its initial height, the surface becomes smoother, which indicates that the wear rate should decrease. Before introducing the asperity height function, we consider the following normalized parameters to simplify the equations.

$$L^* = \frac{L}{L_{\max}}, \quad h^* = \frac{h}{h_i} \tag{4.7}$$

where, $L_{\max}$ is the maximum sliding length and h_i is the average asperity height of the component unworn surface. Therefore, Eq. (4.6) takes the form

$$-\alpha\frac{dh^*}{dL^*} = K \tag{4.8}$$

where, $\alpha = \left(h_i H\right)/\left(L_{\max} P\right)$. Now, by introducing the following asperity height power-law function, we strive to model the effect of surface smoothing:

$$\psi\left(h^*\right) = R\,h^{*n} \tag{4.9}$$

where R is an 'asperity model constant' to be obtained by comparing the theoretical model with the computational data and n is the exponent of the power-law function, also to be determined through a fit of the computational results. A decay over wear length is expected in the wear coefficient. The 'asperity height function' is in the form of a power law, which can fit a decay over length. Substituting the asperity height function $\psi\left(h^*\right)$ into Eq. (4.8), we will have:

$$\begin{cases} -\alpha\dfrac{dh^*}{dL^*} = K, & h = h_i \\ -\alpha\dfrac{dh^*}{dL^*} = \underbrace{K\,\psi\left(h^*\right)}_{K'} = K\,R\,h^{*n}, & h < h_i \end{cases} \tag{4.10a,b}$$

where, $K' = K\,R\,h^{*n}$ is a varying dimensionless wear coefficient, which depends on the variation of asperity height with wear length and on the material properties. By rearranging and integrating, the

varying wear coefficient, K' , can be derived as a function of the sliding length, L^* , and the constant R . There follows,

$$K' = \left\{ \frac{KR}{\left[(1-n)\alpha L^* \right]^n} \right\}^{1/(1-n)} . \qquad (4.11)$$

The wear coefficient thus derived depends on two parameters: the asperity model constant *R* and the power law coefficient n . These latter parameters are determined through a fitting process described here. All the fitting work described here assumed the properties of graphite IG-11. The finite elements computational model presented in later section allows the determination of the asperity height as a function of wear length. That model is used repeatedly to obtain a function describing the height *h* of a given asperity versus the wear length, L , as it is varied between 0.0 and 2.0 meters. The derivative of that function is proportional to K'. Knowing the computed (L , K') pairs and introducing the L values into Eq. (4.11) for K', "model" values for are obtained for various values of the parameters R and *n* . This process allows the formulation of a fitting problem for the R and *n* parameters, based on minimizing the difference between the computed K' and the "model" K'. The values of R and *n* that are retained in this work are the first pair found that results in a maximum absolute error below 10^{-6} for K'. The parameters obtained in this way from computational model data up to 2.0 meters of wear length are then used for predicting the wear performance for up to 1000 meters of wear length with remarkable accuracy, as detailed later through comparison with the experimental results.

4.4.2. The Computational Analysis

The finite element software ABAQUS has been used to conduct simulations of the micromechanics of wear (ABAQUS user's manual). Primarily, 3D spherical asperities were considered to be modeled using the implicit module of ABAQUS known as the 'ABAQUS Standard'. However, given the demanding nature of contact conditions, the nonlinear geometry of the asperities, severe deformations, and foremost, the overlapping of asperities, the implicit module of ABAQUS faced convergence issues. This is due to the time step differences in implicit and explicit numerical schemes. The implicit scheme employs a more reliable and rigorous scheme for considering the equilibrium at each step of the deformation. However, the unconditionally stable implicit method will encounter some difficulties when a complicated 3D problem such as contact is considered. The reason is, the implicit scheme finds a solution by solving an equation involving both the current state of the system and the later one. Thus, as the reduction of the time increment continues at large deformations in 3D problem, the computational cost in the stiffness matrix is dramatically increased and even causes divergence (Kim, 2002). However, the explicit scheme calculates the state of a system at a later time from the known state of the system at the current time. In this scheme the time steps need not be small for convergence, and only stability criteria need to be met. Therefore, an alternative was taken by applying the same methodology in the explicit solver of ABAQUS known as the 'ABAQUS Explicit', which is very robust in handling contact problems.

- Finite Element Model

Fig. 4.9 shows the finite element mesh used for the cylindrical asperity model. This asperity model was made of linear hexahedral elements (C3D8R). R stands for 'reduced-integration', which uses a fewer Gaussian points when solving the integral. The advantage of the reduced integration elements is that the strains and stresses are calculated at the locations that provide optimal accuracy; the so-called

Barlow points (Barlow, 1976). A second advantage is that the reduced number of integration points decreases CPU time and storage requirements.

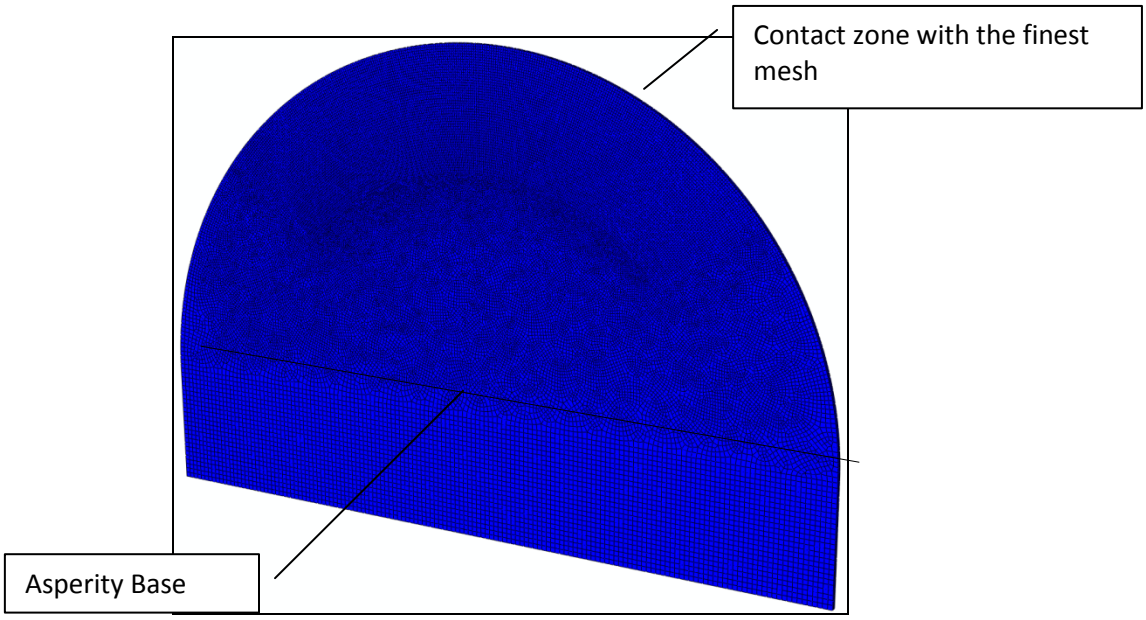

Fig. 4-9. A meshed asperity of radius 3µm and thickness 0.04µm.

In the case of cylindrical asperities which is considered in this study, it would take much shorter run time to conduct the simulation in 2D considering shell elements. However, since element removal is sought in these simulations, the elements which are originally within the interior of the asperity can start to interact with the opposing asperity as a contact surface. This feature is only available in 'general contact algorithm', which requires the use of 3D solid elements. Thus, a 3D model of the asperities was constructed.

Despite being robust for large deformations and saving extensive amounts of run time, the reduced-integration solid and shell elements used in ABAQUS are prone to zero-energy modes. These modes, commonly known as hourglass modes, are oscillatory in nature and result in mathematical states that are physically unfeasible. They typically have no stiffness and give a zigzag appearance to the mesh as seen in Fig. 4.10, known as hourglass deformations. The occurrence of hourglass deformations in an analysis can invalidate the results and should always be minimized. Therefore, hourglass control is used to overcome this deficiency. This formulation provides improved coarse mesh accuracy with slightly higher computational cost and performs better at high strain levels. Hourglass control is an embedded feature in ABAQUS.

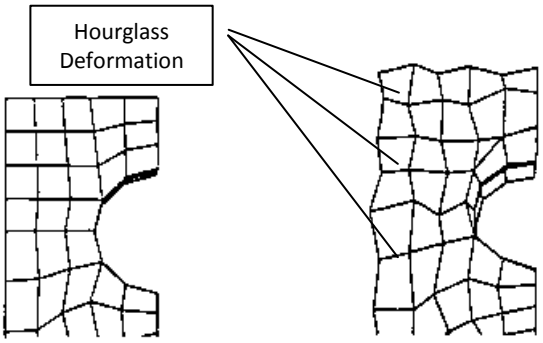

Fig. 4-10. A schematic of Hourglass deformation.

Plane strain is simulated in this 3D model by constraining the front and back planar faces of the asperity as a symmetry boundary condition (i.e. $u_z = 0$, $ur_x = ur_y = 0$). In this way, the model behaves as a plane strain slice. For simplifying the boundary conditions, a prescribed velocity was primarily used for the movement of the upper asperities and the lower asperity was fixed as its base. Hence, to simulate the movement of both pebble surfaces, the relative tangential velocity was applied to the moving (upper) asperities. In another simulation, it was found out that prescribing velocities to both upper and lower asperities in opposite directions provides more realistic results for the two asperities. Therefore, the actual tangential velocity of pebbles at contact was applied to upper and lower asperity bases.

- *Mass Scaling*

Modeling using an explicit procedure can take a considerable amount of time for the simulation to converge. This is due to the fact that the minimum stable time increment is very small. The minimum time step size for explicit time integration depends on the minimum element length, l_{min}, and the speed of sound in the medium, c. One should note that for a given set of material properties, the minimum time step size Δt_{min}, is controlled by the smallest element dimension in the model. Also, for a given mesh, the minimum time step size depends upon c, which is a function of material density, elastic modulus, and Poisson's ratio. In ABAQUS, the 'mesh verification tool' determines the minimum time step size in the model.

$$\Delta t_{\min} = \frac{l_{\min}}{c}, \quad c = \left(\frac{E}{\rho\left(1-\nu^2\right)} \right)^{1/2}$$

where, ν is the Poisson ratio, ρ is the specific mass density and E is the Young's Modulus. The minimum stable time increment was verified by the "mesh verification tool" in ABAQUS/CAE, which in this case is 10^{-12} s.

In ABAQUS/Explicit, one can control the minimum time step size by including artificial mass scaling into the analysis. It may be necessary to use mass scaling if the calculated time step is too small. When mass scaling is introduced, element density is artificially adjusted to achieve a specified time step size. When used appropriately, mass scaling can often improve the computational efficiency while retaining the necessary degree of accuracy required for a particular problem class. The following relations indicate how a change material density can lead to a change in the minimum time step:

$$\left(\frac{\Delta t_{artificial}}{l_i}\right)^2 = \frac{\rho_i\left(1-\nu^2\right)}{E} \Rightarrow \rho_i = \frac{\left(\Delta t_{artificial}\right)^2 E}{l_i^2\left(1-\nu^2\right)}$$

It is seen that the artificial mass scaling does not affect the material properties like the modulus of elasticity and the Poisson ratio. Instead the corresponding artificial step time increases. Care must be taken not to add too much mass to a model in which inertial effects are significant. Mass scaling was introduced into the material model in multiple steps. This means that in every step, an artificial mass was added and the simulations were performed. After assessing the results, if inertial effects were not seen as compared with the results of no artificial mass, then some more mass was introduced. Otherwise, mass scaling would not be continued.

- *Material Model*

The material properties for nuclear grade graphite IG-11 were chosen for the asperity model. Here we have used a damage model and have included damage evolution to visualize the degradation of the fully damaged elements. Material failure refers to the complete loss of load-carrying capacity, which results from progressive degradation of the material stiffness. An undamaged constitutive behavior of the material (i.e. elastic-plastic with hardening) is determined (Yokoyama, 2008) as seen in Fig. 4.11.

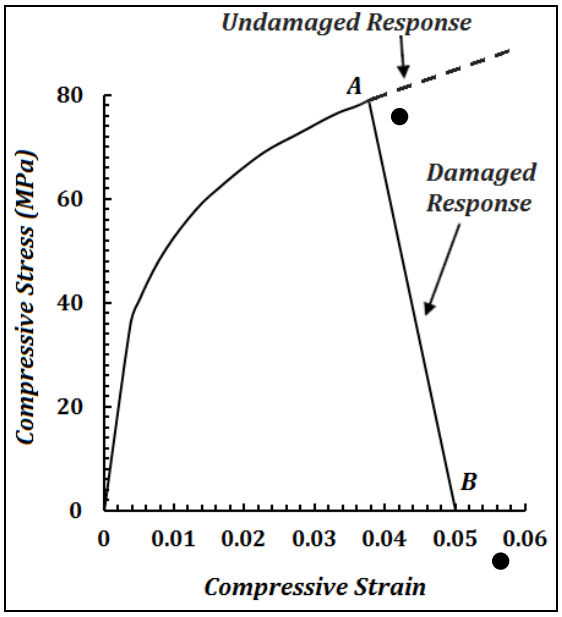

Fig. 4-11. Elastic-plastic behavior with hardening for nuclear graphite IG-11.

Then, a damage initiation criterion is determined (point A). This is followed by damage evolution (path A–B) and finally the choice of element removal (point B).

In absence of any experimental data for the damage softening part of the curve (A-B), a simple linear damage evolution law was used to degrade the material stiffness to zero where the equivalent total strain reaches 0.05 (point B in Fig. 4.11). When an element reaches point B on the curve, its stiffness has fully degraded, and the element is removed from the mesh. The assumption for the degradation point is reasonable since graphite does not withstand high strains.

4.5. The Finite Element Analysis

The height of asperities and the surface topology determine the roughness of the material surface. The average asperity height for the IG-11 provided by Toyo Tanso Inc. for the experiments performed by Johnson (2012) is 3µm. Considering asperities of various heights results in a range of asperity overlaps. The common range for overlaps is between 2.5 and 7.5% for steel (Faulkner, 2000). However, no such report is available for nuclear grade graphite. Having an average asperity height, an average overlap of 5% is considered in the FEA simulations of asperity interaction.

The finite element analysis of asperity contact in ABAQUS Explicit revealed that asperities undergo very high deformations. As the material reaches a total strain of 0.05, the elements are removed and the degradation leads to material removal from the asperity. In Figs. 4.12, the degradation and material removal from asperities of 3□m high are presented.

Since the Von Mises stress is very high everywhere in the model, a Von Mises stress contour would not be helpful is distinguishing the high deformations. The deformation at the microscale is very large as compared with macroscale. Since large plastic deformations are present, equivalent plastic strain contour (PEEQ) is presented in Figs. 4.12. The red color shows the highest plastic deformation at the contact region. The blue color shows the smallest plastic deformation, which is mostly observed at the asperity base.

The height of the worn asperity from the first simulation was used to perform the next simulation on this asperity after one full rotation of the graphite pebble. This process continued to derive the right hand side of Eq. (4.10b). This is needed to derive the 'asperity model constant', *R* and the power law exponent, *n*. As seen in Eq. (4.10b). One idealization made here is assuming a new asperity with its original shape but with new height, which derived from the asperity removal as shown below.

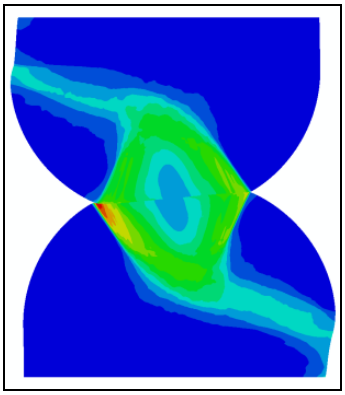

(a)

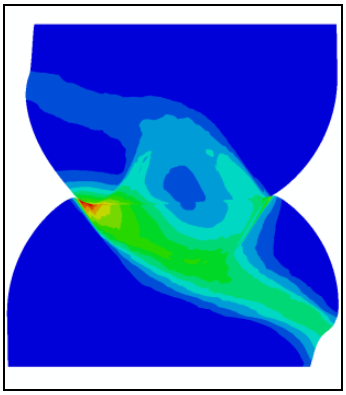

(b)

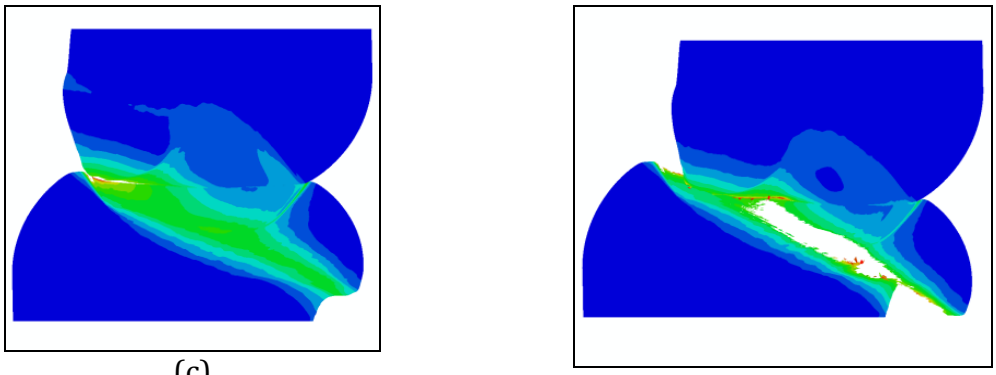

(c) (d)

Fig. 4-12. Equivalent plastic strain contour: the degradation and material removal process from asperities at: (a) t=0.000325s , (b) t=0.0013s, (c) t=0.002275s and (d) t=0.00325s for tangential speed of 0.08m/s.

4.6. Verification with the Experimental data

In this project, we construct the wear apparatus to test wear dust accumulation from nuclear grade graphite spheres. The verification with the experiment is carried out to examine the computational model.

4.6.1. Sample Surface Observations

The SEM images (Fig. 4.13) from the room temperature graphite samples, after ~1000 m of sliding show a wear scar of 1.7mm wide, show a smooth and clean surface. This is while outside of wear scar, a rough surface from the fabrication process is observed. This indicates that the asperities were polished and leveled by the rotating motion.

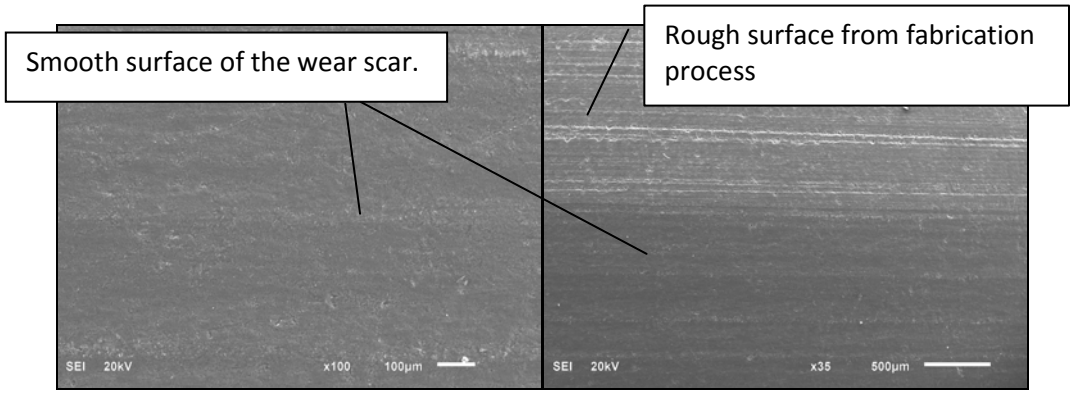

(a) (b)

Fig. 4-13. The SEM images of graphite sample (a) wear scar zone (b) interface between the scar (lower) and rough zone (upper).

4.6.2. Asperity Model Wear Results

The wear mass results from the tribometer are presented in Fig. 4.14. The wear mass was recorded every approximately 200 meters. Fig. 4.14 clearly demonstrates that the primary wear rates are reduced as the sliding length increases. This indicates a power-law decrease of wear mass with wear

length. The error bars show the uncertainty of the experimental data, which is due to the uncertainty in the scale used for collecting gradual mass measurements.

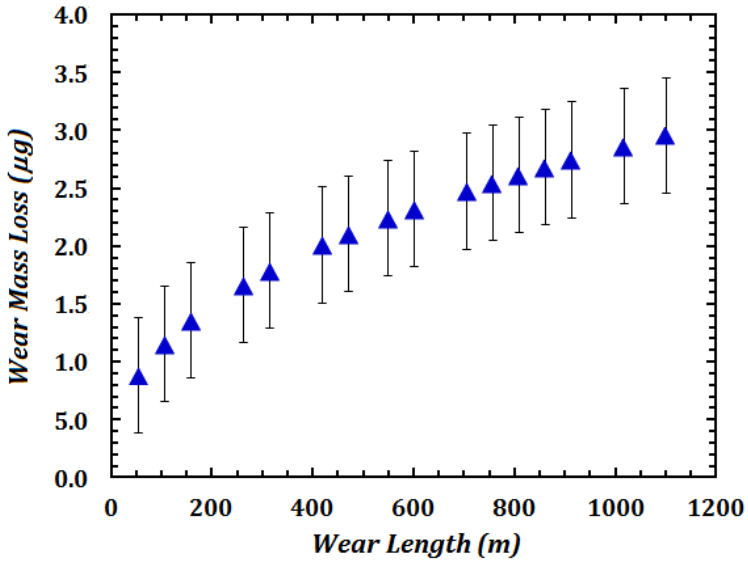

Fig. 4-14. Wear Mass Loss from the experimental air-tests for ~1100 meters.

The wear coefficient obtained from the theoretical model is compared to the computational results in Fig. 4.15a, and to the experimental data in Fig. 4.15b. The theoretical model exponent and 'the asperity model constant' were derived by fitting with the computational results. The model thus obtained is then compared with the experimental data for verification purposes.

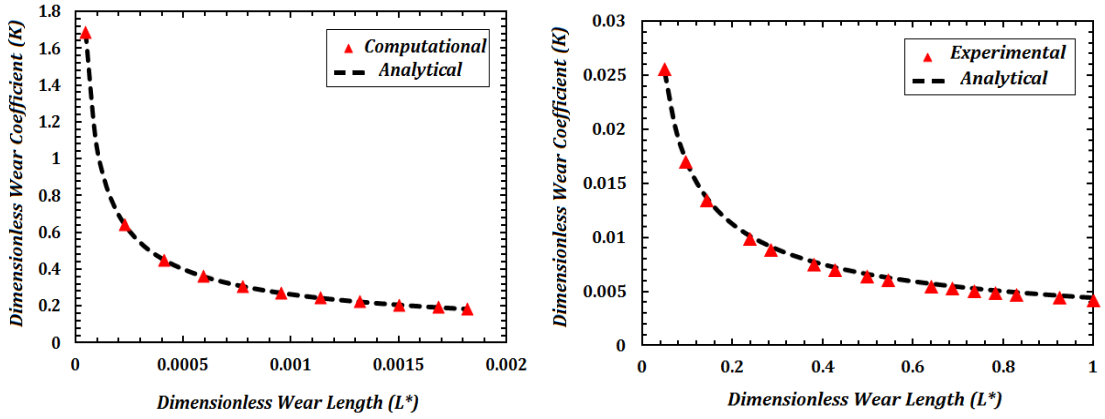

(a) (b)

Fig. 4-15. Comparison of theoretical K with (a) computational results and (b) experimental data with respect to the dimensionless sliding length, L^*.

With a fit of the analytical mode with the computational results, the exponent, *n*, is computed to be -1.38 and the dimensionless micro-level asperity model material constant, *R*, is 2.5×10^{-4}. The minimum (final) asperity height, as predicted by this model, is 12.45% of the initial average asperity

height. This indeed indicates that the surface has become smoother and thus the wear coefficient smaller.

Using the new varying wear coefficient, the wear results, which were predicted before based on a constant coefficient, can now be rectified. It is clearly observed in Fig. 4.15b that the proposed theoretical model, which stems from the computational data, predicts a higher overall wear coefficient than the actual wear coefficient derived from experimental data. This is because the natural lubricating properties of graphite surface have not been considered (Czichos, 1978). As explained earlier, when two graphite surfaces are in frictional contact at room temperature under the PBR loads, powder formation is the main form of wear. The powder is then capable of filling in the surface valleys, which causes the surface to become smoother than what is incorporated into our ABAQUS model. Therefore, there is a difference between the predicted wear coefficient and the experimental results. The proposed wear coefficient has been used to produce wear mass loss. As seen in Fig. 8.10a, the initial wear rate starts to decrease by wear length. The predicted wear mass using the proposed analytical model (Fig. 4.16a) shows an excellent agreement with the experimental data (Fig. 4.16b). The significance of the proposed varying wear law is seen as compared to the predictions by the conventional Archard's equation (Fig. 4.16b). The error bas indicated on the graph in Fig.4.16b are from the uncertainty associated with the scale with which the data was recorded. This indicates that the analytical model has predicted reliable results that fit in within the uncertainty limits.

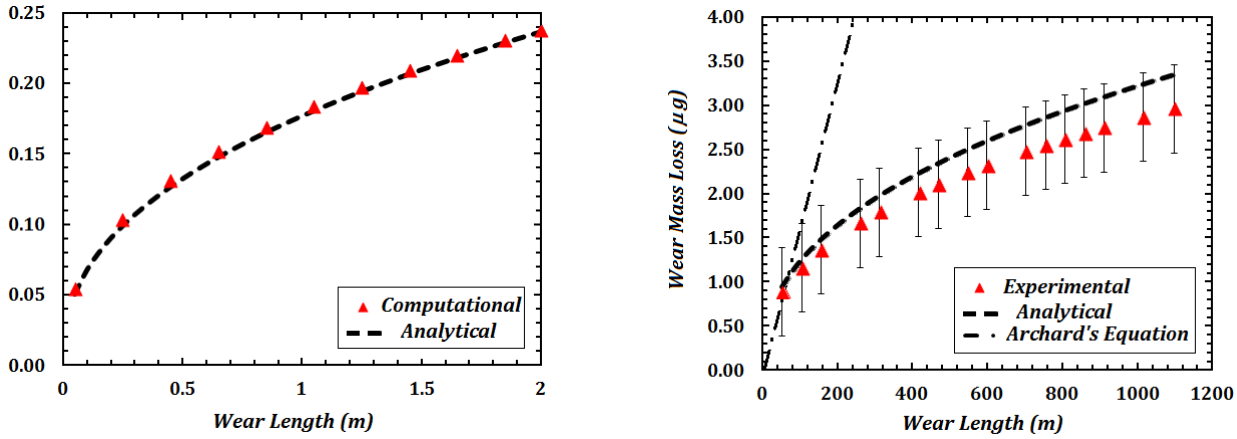

(a) (b)

Fig. 4-16. Instantaneous and cumulative wear mass for a pebble with respect to wear length, L.

Due to the difference between the predicted and actual dimensionless wear coefficients, the predicted wear mass is approximately 20% higher than the actual wear mass. There is another explanation for the difference between the theoretical and experimental data. That is, the uncertainty in the reported experimental data at room temperature is very high. This is because the uncertainty attributed to the analytical scale used in the mass measurements (10^{-5}g) is larger than the smallest particulate mass (7.414×10^{-6}g). Therefore, it is concluded that the results by the proposed wear model falls within the uncertainty boundaries of the experimental results. It is also clearly observed in Fig. 4.16b that the proposed wear model shows a significant improvement in comparison to the Archard wear equation. This improvement is in the consideration of the change in the surface topology, which was not considered in the Archard's equation.

The varying wear rate of graphite is shown in Figs. 4.17. It is seen that the wear rate decreases as graphite asperity height decreases with increasing wear length. The reported wear rate was a constant 8.45×10^{-8} (Johnson, 2012). This value is the same as the initial rate predicted in the present study.

However, in the present study, the rate is shown to be varying by wear length. It must be noted that the present results are for air test at room temperature and atmospheric pressure and under the inter-pebble loading for a typical PBR.

Any variation in these factors leads to a different wear rate or even wear mechanism. High temperatures effects are experimentally examined in this study and the wear mechanisms contributing to wear regimes are discussed later.

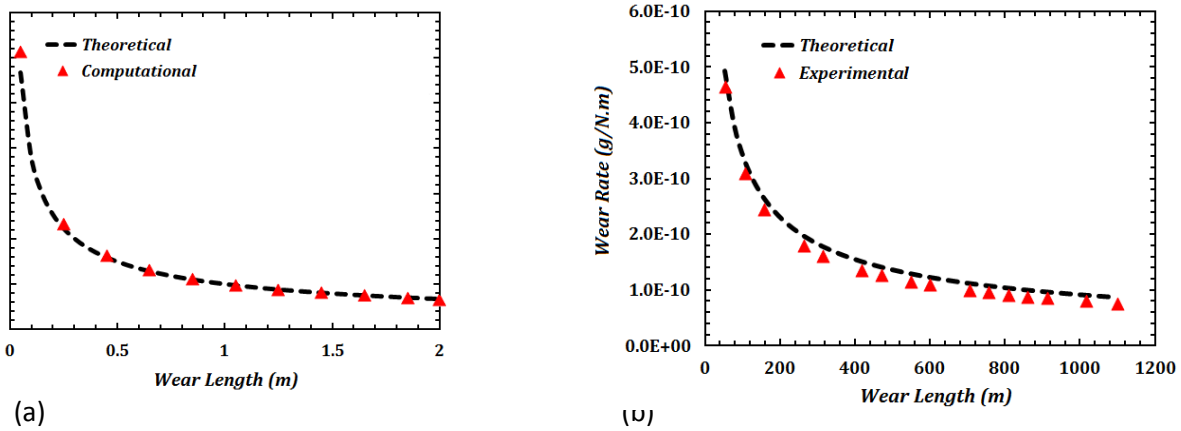

Fig. 4-17. Wear rate for one graphite pebble with respect to wear length, L.

Using the dimensionless wear coefficient, K', obtained in this work, it is attempted to derive the wear mass for one pebble through 2.06m of HTR-10 wear length as performed by Rostamian et al. (2012). By performing wear calculations as carried out by Cogliati et al. (2011) based on the air-test results of Lou et al. (2005), the wear mass produced by inter-pebble forces (Cogliati, 2008) is calculated. Estimates for HTR-10 and AVR are reported using the present model. The wear mass for one pebble is estimated to be 0.235 mg. For HTR-10 with an inventory of 27,000 pebbles and a pebble flow rate of 125 pebble per day, the wear mass is predicted to be 5.36g/yr. As explained by Rostamian at al. (2012), the estimated wear mass for AVR would then be 63.555g/yr.

4.7. Conclusion of Chapter 4

The computational results revealed that there is a ~20% difference between the theoretical model-based simulation and the experimental data. This is attributed to the lack of a surface-level lubrication component in the model, thought to be induced by 'gas adsorption' as well as 'relocation of surface-adhering graphite particulates'. Gas adsorption decreases the wear mass loss due to filling of edge sites (Roberts, 1995). It is assumed that when particulates are formed due to wear, they primarily relocate in the valleys between asperities (Play, 1977). The gas adsorption and particulate relocation increase the smoothness of the surfaces, which in turn decrease the wear coefficient. The lamellar structure of graphite facilitates the establishment of smooth surfaces between sliding contacts, and the presence of adsorbed gases may further improve the quality of these surfaces. Since these artifacts are not considered in the finite element simulations, the predicted wear coefficient is larger than that attributed to the experimental data.

The proposed model and the experimental results show that the wear mass for air environment at room temperature and atmospheric pressure is small and on the order of grams per year for a reactor. Therefore, it is predicted that higher temperatures contribute to increased wear. It was shown by Lou et

al. (2005) that the wear rate of graphite at elevated temperatures is much higher than that at room temperature. Lou (2005) performed a theoretical study of higher temperature wear of graphite without the consideration of helium environment.

In the following section, helium-test experimental data at higher temperatures and pressures will be reported, and the effects of such environments are discussed.

- *A Note on Uncertainty of FEA Results*

The uncertainty of final wear mass results from FEA calculations cannot be reported due to two major reasons: 1) the uncertainty of the material data was not indicated in the source reports of journal papers; 2) since no data on damage evolution of graphite was reported, the damage evolution model considered in this study is an assumed linear model. However, the room temperature results predicted by the analytical model are within the uncertainty limits of the experimental data.

The predicted amount of dust obtained in this study is at least two, if not up to three orders of magnitude lower than the dust mass required for explosions described below.

5. Prediction study of Isochoric inert gas behavior

5.1. Graphite dust combustion/explosion in PBR

It is evident that during normal operation of a graphite-moderated MHTGR, dust will be generated due to frictional contact and wear of graphite surfaces. One expects that the magnitude of generated dust will be different in the two MHTGR designs; the PMR and PBR. In the both primary circuit configuration, thermo-fluid and thermo-physical conditions, besides transport we expect deposition and re-suspension (lift-off) of dust. To add further complexity, there will likely be fine particles that migrate as the fuel form into the primary system. Thus there is the potential for 'dust/fine particle interaction'. As noted, this defines the source term of postulated events. In fact, the accumulation of dust and fine particles determine the initial condition.

In two postulated scenarios, the pressurized loss-of forced circulation (P-LOFC) accident, and depressurized loss-of-forced circulation (D-LOFC) accidents, the accumulated inventory of dust in the primary system presents itself as a potential source of a dust combustion/explosion. This is especially true in the presence of an "ignition source" and source of continuous thermal energy and sufficient supply of air (oxygen) within and near the dust. Also, the potential for "auto-ignition" increases with elevated temperatures. In the literature, there is little on graphite itself; however, there are studies on different grades of coal and carbon in particulate/powder forms. In fact, the body of research spans many industries, as reviewed, for example, by Cashdollar and Eckhoff. Eckhoff noted the importance of preventing the ignition of sources and explosion of dust clouds and finally, mitigating the explosion itself. VDI3673 and NFPA68 Standard may be of relevance to NGNP especially, in terms of vent sizing methods. Eckhoff, Arntzen and co-workers have developed a multiphase CFD code, Flame Acceleration Simulator, with partial validation form experiments. However, these are beyond the present scope of work.

There is limited experimental data on combustion of graphite dust, particularly at elevated temperatures. Furthermore, data specifically on nuclear grade graphite is likely non-exist or unpublished. However, from limited data on graphite wear study and past MHTGR programs (i.e. AVR, Ft. St. Vrain), the dust characteristics indicates that graphite will be generated in quantities sufficient to support dust auto-ignition and combustion. That is, with respect to the anticipated particle size, dust concentration, stoichiometry, and temperature, a graphite dust explosion is possible. This thus requires study with respect to NGNP.

In the literature on (generalized) dust explosion, care has to be exercised in the interpretation of experimental data where a pressurized source is used to disperse graphite particles. Convective effects due to strong pressure gradients can lead to significant error in the interpretation of system pressure. Moreover, the influence of the ignition source on the (P, T, V)- fields must be carefully studied. In addition, there is evidence that dust layers on a surface may itself have an ignition temperature. This effect has been demonstrated with certain perspective, the 'knowledge base' gaps and needs are as follows; that is, there is a need for: 1) data based on experiments, modeling and theory specifically on volatile and non-volatile fission products as retained by bulk graphite and graphite particles., and 2) experimental data in order to verification and validation models (computational) at NGNP relevant conditions.

5.2. Graphite Particle Pyrotechnically-induced Dissociation Testing Apparatus

A novel testing apparatus (Fig. 5.1) is used to determine the combustion characteristics of graphite and air at high temperatures. The apparatus is based on ballistic test fixture already designed, fabricated, and tested to study confined explosions and detonations. The apparatus is designed such that individual components may be easily exchanged with minimal effort.

A key element of the test apparatus is a pair of pyrotechnically-actuated valves used to separate the graphite powder production chamber from the combustion test apparatus. These “pyro-valves” are used to separate the pressurized chamber where the powdered graphite is produced from the combustion test apparatus. Upon actuation, the valves allow gases to flow from the high pressure region into the lower pressure camber. The performance of these “pyro-valves” is superior to burst discs because they are unaffected by elevated temperatures, no debris introduced into mixture, and the mixing characteristics of the gases can be tailored.

Combustion experiments are conducted using different ballistic test vessels connected to the pyro-valves. The choice of vessel depends on the objective for a particular test. Combustion parameters that can be measured include: minimum ignition energy, flame speed, flammability and detonation limits, detonation cell size, and deflagration-to-detonation transition (DDT) lengths. These fixtures can withstand repeated exposures to dynamic pressures of 207MPa (30kpsi). The vessels feature several ports to accept pyrotechnic or electrical initiators, multiple pressure transducers, strain gauges, and various optical instruments.

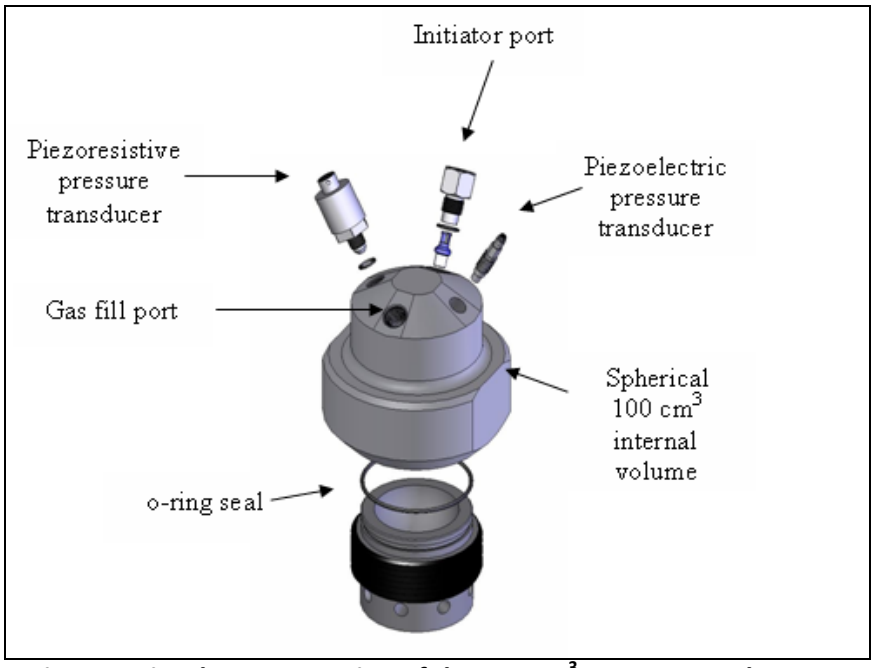

Fig. 5-1. Visual representation of the 100 cm^3 reactor vessel.

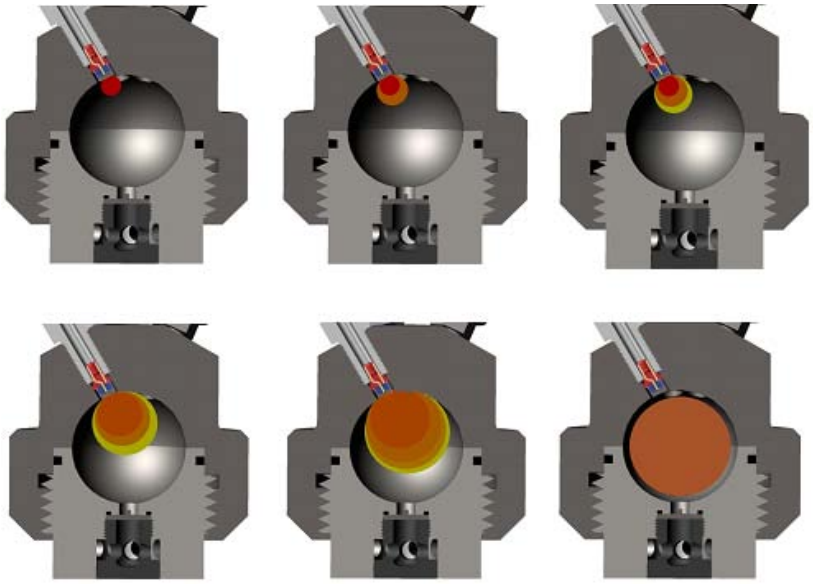

Fig. 5-2. Evolution of heat generated during the pyrotechnically-induced dissociation of nitrous oxide.

5.3. Pressure Sensors and Data Acquisition

Static pressure sensors measure the pressure of the gases the fixture at the initial fill conditions and during temperature conditioning. Since the static sensors are susceptible to damage from the dynamic pressures generated in an explosion, they are isolated from the internal environment during testing by valves. Dynamic pressures are monitored using piezoelectric sensors. Signals are fed to a data acquisition system (DAQ) capable of sampling up to 2×10^{8} samples/second. With a typical 2µs rising time, this is sufficiently fast dynamic events anticipated in graphite combustion.

Thus, this task includes conducting the experiments that simulate air-ingress accident in PBR upon depressurization transport of generated graphite dust. Compare experimental data using the call to 'map' the minimum explosible limit range of at least the nominal particulate size, concentration, and additional prioritized parameters of relevance to the air ingress accident in PBR. Since there is a common initiator for ignition devices with graphite, Zirconium Potassium Perchlorate (ZPP) is reviewed and selected for this task.

5.4. ZZP combustion

ZPP is commonly used in automotive airbag initiators, aerospace initiators and other ignition devices [Forman. 1991]. ZPP is comprised of zirconium, potassium perchlorate, Viton B and graphite. The following table provides the composition of ZPP as given by Hohmann, Tipton and Dutton [Hohman, 2000].

Table 5-1. Composition of zirconium potassium perchlorate [Hohman, 2000].

Ingredient	% By Wt.
Zirconium	52
Potassium Perchlorate	42
Viton "B"	5
Graphite	1

Viton “B” is a rubber binder comprised of tetraflouroethylene, hexaflouropropylene and 1,1 diflouroethylene with weight percentages of 20, 15, 65 respectively. According to Hohmann et al [Hohman, 2000], Viton “B” serves a dual purpose, one is the binding of the metal powders to the potassium perchlorate, and the other is to extend the age life of the pyrotechnic mixture. Further, it is mentioned that graphite is added to the mixture in order to increase its density thereby increasing the reaction rate of the pyrotechnic mixture [Hohman, 2000]. The potassium perchlorate is used to provide oxygen for the redox reaction during the decomposition of ZPP, and the zirconium is used as the reducing agent [Hohman, 2000]. It is also reported that the caloric content of the ZPP mixture ranges from 1340 to 1450 calories per gram.

Gillard and Roux [Gillard, 2002] studied the ignition and combustion characteristics of a 40 mg ZPP mixture in a closed volume. They found that the mixture burns in about 200 microseconds at approximately 3000 K and transfers energy to the chamber walls via radiation from the hot ZPP particulates. This study is significant as it provides experimental parameters, in particular the burn rate and temperature, associated with ZPP combustion.

5.5. Energy Release Characteristics of ZZP combustion

The total energy released by ZPP combustion has been thoroughly studied, and previous work by Richardson and Rink [Richardson, 2001] indicate the energy content of ZPP is approximately 5455 J/g. This value is within the ranges quoted by Hohmann et al [Hohmann, 2000], for various ZPP formulations.

In order to estimate the amount of time required for ZPP to deliver its sensible energy to the surrounding nitrous oxide mixture, a transient analysis of the initiator function is required. However, it should be noted that only an estimation of this time is required. A detailed analytic model describing the heating and energy release from the ZPP is beyond the scope of this paper, but is the subject of future research.

The details concerning the combustion of ZPP are quite complex and knowledge of relevant associated rate parameters is limited. However, in order to estimate the rate at which the energy is released from ZPP combustion, the heating and decomposition times of the material need to be estimated. It has been found that ZPP follows first order kinetics and an Arrhenius equation can be used to represent its dissociation [Helmy, 2004]:

$$K_{zpp} = Ze^{-\frac{E}{RT}} \qquad (5.1)$$

where:

K_{zpp} is the reaction rate constant (min^{-1})

Z is the pre-exponential factor (min^{-1})

R is the universal gas constant (cal/mol/K)

E is the energy of activation (cal/mol)

T is the temperature of the ZPP (K).

Helmy found the pre-exponential factor and the activation energy to be 1.55×10^{16} min^{-1} and 50.5 Kcal/mol, respectively [Helmy, 2004].

The expression for the specific rate constant Equation (5.1) can be combined with concentration to express the rate law. If the control volume is taken to be the closed vessel chamber and assuming no leaks, then a simplified first order reaction is:

$$\frac{dC_{zpp}}{dt} = -K_{zpp}C_{zpp} \tag{5.2}$$

where:

C_{zpp} is the concentration of solid ZPP (mol/cm^3)

t is the time (ms)

K_{zpp} is the reaction rate constant from Eq. (5.1).

Further, the solution to equation (5.2) is:

$$Ln\left(\frac{C_{zpp_f}}{C_{zpp_O}}\right) = -K_{zpp} * t \tag{5.3}$$

where:

C_{zppo} is the initial concentration of ZPP

C_{zppf} is the final concentration of ZPP at some time t.

The solution of Equation (5.3) yields the time required for complete combustion of the pyrotechnic charge. However, to evaluate the reaction rate constant from Equation (5.3) the temperature of the ZPP as a function of time must be known.

In modern pyrotechnic initiators, the pyrotechnic charge is ignited by a small, electrically-heated, bridge-wire in intimate contact with the ZPP [Nyer, 1997]. Details concerning the mechanical and electrical design of the initiators are available in the literature [Forman, 2006, Rink, 2006, Thompson, 2007]. The temperature of the bridge-wire increases as a function of time according to:

$$T_W = T_O + \frac{{I_w}^2 R_w}{m_w Cp_w} t \tag{5.4}$$

where:

T_w is the temperature of the wire (^oC)

T_o is the initial temperature of the wire at ambient conditions (^oC)

I_w is the current passing through the (amps)

m_w is the mass of the bridge-wire (g)

Cp_w is the heat capacity of the bridge-wire ($J/g/^oC$)

R is the resistance of the wire (ohms)

t is the time the current is passed through the wire (ms).

According to Beyer [Nyer, 1997] the mass and heat capacity of a typical bridge-wire is 1.804E-5 g, and 0.44 $J/g/^oC$ respectively. Further, a typical current sent through a bridge-wire for this work is 3 amps [Rink, 2009].

Equation (5.4) is developed assuming a constant bridge-wire resistance. To account for more realistic variable resistance bridge-wires, Davenport [Davenport, 1967] expressed the temperature dependency of the wire resistance as:

$$R_W = R_O(1 + \alpha T) \tag{5.5}$$

where:

R_o is the initial resistance of the bridge-wire (ohms)

α is a constant ($ohms/^oC$)

T is the temperature of the bridge-wire (^{o}C).

Because α is typically in the range of 1x10^{-3} to 4x10^{-3} ohms/^{o}C for bridge-wires [Davenport, 1967], a value of 2.5x10^{-3} ohms/^{o}C is assumed to be reasonable. Further, since the resistance of the wire is 1 ohm at the temperature of the surrounding ZPP, assumed to be 25 ^{o}C, a value for R_o is estimated to be 0.94 ohms. Then, to find the temperature of the wire as a function of time, Equations (5.5) and (5.4) are combined to give:

$$T_W = T_O + \frac{I_W{}^2 R_{O_W}(1+\alpha T_W)}{m_W Cp_W} t \qquad (5.6)$$

Rearranging to obtain an explicit expression for the temperature of the wire as a function of time yields:

$$T_W = \frac{I_W{}^2 R_{O_W} t + Cp_W m_W T_O}{a I_W{}^2 R_{O_W} t - Cp_W m_W} \qquad (5.7)$$

For the values stated above a discontinuity occurs at 0.373 ms. The presence of this discontinuity suggests an infinite wire temperature, which obviously is not physically possible. Although more accurate formulations of bridge-wire heating have been developed [Nyer, 1997], this simplified model is shown to be sufficient for estimating the time required for ZPP ignition and combustion.

Finally, since the current through the wire is constant, the power delivered from the wire can be found by substituting Eq. (5.5) into the power expression from Ohm's law:

$$P_W = I^2 R_O(1+\alpha T_W) \qquad (5.8)$$

Typical bridge-wire initiators are characterized by resistances of 2 ohms and currents between 1 and 3 amps [USCAR, 2004]. Further, the transport properties of typical bridge-wire materials are well known [Nyer, 1997]. Therefore, as shown in Figure 6 the temperature of the wire can be estimated.

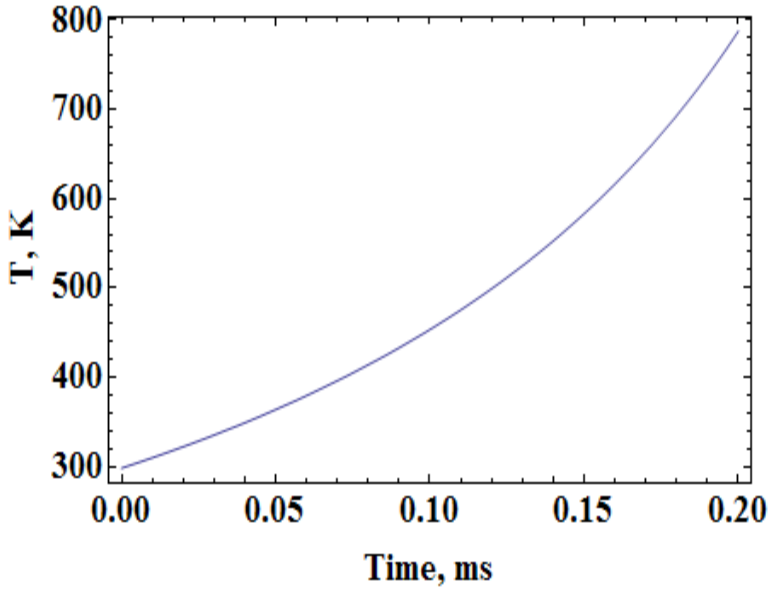

Fig. 5-3. Temperature of the bridge-wire as a function of time.

As the bridge-wire heats, it releases energy to the surrounding ZPP charge. Therefore, for the sake of simplicity, it is assumed that a certain amount of ZPP in intimate contact (denoted as "ZPPIIC" throughout this thesis) is thermally equilibrated with the bridge-wire. Using this assumption it is possible to estimate the rate at which ZPP reacts. This estimate is fundamental to the development of the analytical model described in this thesis, and is explained in the following paragraphs.

In order to estimate the rate at which the ZPP burns, it is necessary to describe how the bridge-wire heats the charge. The auto-ignition temperature of ZPP is 775 K [Lee, 1990]. Further, when the bridge-wire heats to the auto-ignition temperature of the charge, the ZPPIIC will begin to burn. As the ZPPIIC begins to burn, it is assumed that enough energy to heat the remaining charge of ZPP is liberated. Although this is not a physically realistic description of the process, it not only provides a conservative estimate for the time required for ZPP combustion. But, it also provides an expression for the rate of sensible energy transferred to the nitrous oxide-bearing mixture.

In order to estimate the amount of ZPPIIC required to heat the remaining charge the following heat transfer model applies:

$$E_{zpp} X m_{zpp} = (1 - X) m_{zpp} Cp_{zpp} \Delta T \qquad (5.9)$$

where:

E_{zpp} is the energy of the pyrotechnic charge (J/g)

Xm_{zpp} is the mass of ZPP in intimate contact with the wire (g)

$(1\text{-}X)m_{zpp}$ is the mass of remaining ZPP (g)

Cp_{zpp} is the heat capacity of the ZPP mixture (J/g/K)

ΔT is the temperature rise from ambient to the auto-ignition of ZPP (K).

By using the values given earlier in this thesis and estimating the heat capacity for the pyrotechnic charge, the amount of ZPPIIC is estimated to be 8.25 mg.

As the ZPPIIC burns, hot gaseous products at approximately 3140 K are generated [Berger, 2005] and, as a result, high pressures are produced within the ZPP charge. This pressure gradient forces the products from both ZPPIIC and ZPP combustion through void spaces in the remaining charge. As the combustion products progress through the remaining charge and the ZPP reaches its auto-ignition temperature of 775 K, additional hot gas is produced. In this situation the model of Hohmann [Hohmann, 2000] can be modified to include the void fraction (ε) to yield:

$$\frac{dm_{zpp}}{dt} = -K_{zpp} * \varepsilon * m_{zpp} \qquad (5.10)$$

Following Belyaev (1975] the void fraction (ε) is estimated to be 0.04. This agrees with prior estimations for the void fraction of ZPP as given by Rink [Rink, 2006]. However, before an estimate of the rate of combustion for the entire ZPP mass is calculated, it is first necessary to estimate the rate at which ZPPIIC charge burns. Equation (5.2) can be used to estimate the rate of reaction of the ZPPIIC as a function of time. The results of this are shown in the following figure.

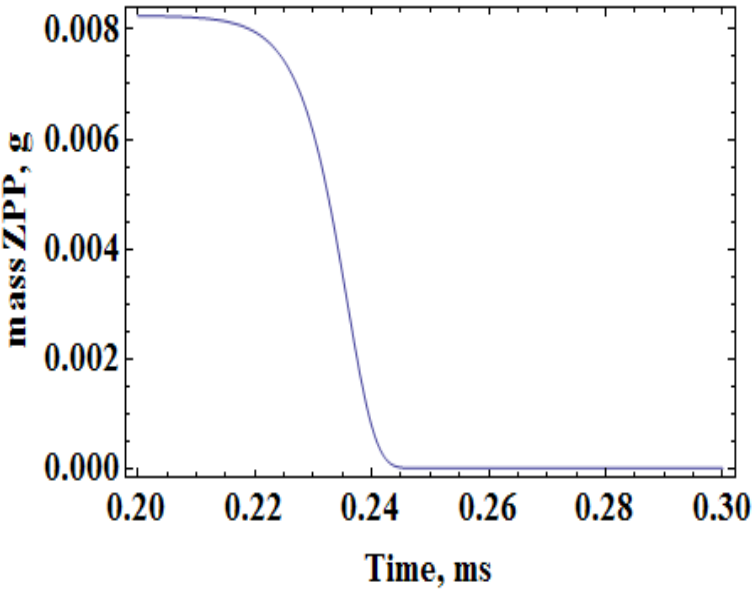

Fig. 5-4. Mass of ZPPIIC with the bridge-wire as a function of time.

Recall that the bridge-wire and the ZPIIC are assumed to be in thermal equilibrium. Because the model for the bridge-wire temperature (Figure 5-3) indicates that the ZPP ignition temperature (775 K) is reached in 0.2 ms, Figure 5-4 indicates that ZPPIIC ignition begins after a further delay of approximately 0.02 ms. At this point, the products of combustion from the ZPPIIC are forced through, and heat, the remaining charge. Assuming that these gaseous products heat the remaining mass uniformly; the amount of time required to dissociate the remaining mass is estimated by using Equation (5.10). Results of this analysis are shown below in Figure 5-5.

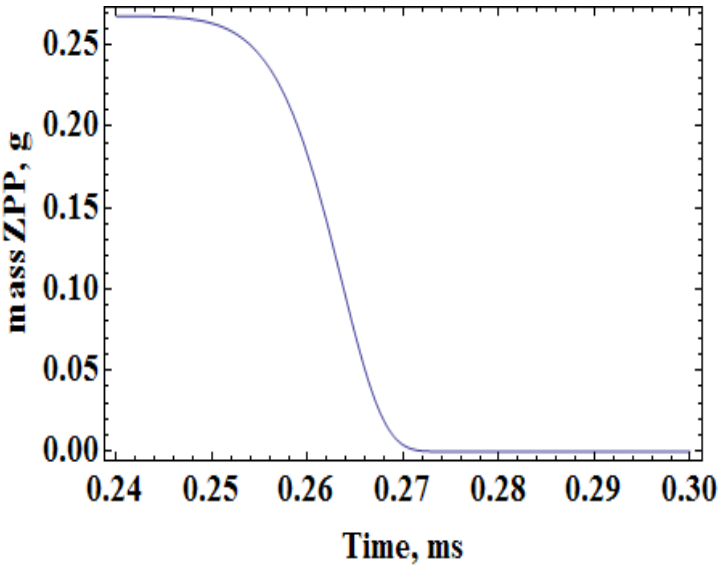

Fig. 5-5. Mass of remaining ZPP as a function of time at 3140 K.

Figure 5-5 shows that approximately 99% of the remaining charge is completely burned in 0.27 ms. Although this estimate is considered to be conservative, it is in agreement with dissociation rates of ZPP measured to be approximately 0.2 ms [Gillard, 2002].

In summary, a 275 mg charge of ZPP is found to react in approximately 0.27 ms while providing 5455 J/g [Hohmann, 2000, Richardson, 2002] and producing combustion products at 3100 K [Berger, 2005]. The validity of the ZPP combustion temperature is confirmed. This predictive capability is an important input for the analytical model of nitrous oxide dissociation developed in the following section.

5.6. The Density Limit of ZPP and Shell Model

The model presented by Turns [Turns, 2000] is derived combining the First Law of thermodynamics and the principles of chemical kinetics. Assuming ideal gas behavior and homogeneous mixtures, Turns [Turns, 2000] derived the following relations for the transient temperature and pressure within a closed vessel:

$$\frac{dP}{dt} = R_u T \sum_i \omega_i + R_u \sum_i X_i \frac{dT}{dt} \qquad (5.11)$$

$$\frac{dT}{dt} = \frac{\frac{Q}{V} + R_u T \sum_i \omega_i - \sum_i (h_i \omega_i)}{\sum_i X_i (Cp_i - R_u)} \qquad (5.12)$$

where:
P is pressure (MPa)
T is temperature (K)
t is time (ms)
R_u is the universal gas constant
ω_i is the reaction rate of the i^{th} chemical species (mol/cm^3/ms)
X_i is the concentration of the i^{th} chemical species (mol/cm^3)
Q is the heat transfer rate (J/ms)
V is the volume (cm^3)
h_i is the specific enthalpy of the i^{th} chemical species (J/mol)
Cp_i is the heat capacity of the i^{th} chemical species (J/mol/K).

However, a complication arises in applying the homogeneous model of Turns [Turns, 2000] to the heterogeneous, pyrotechnically-induced dissociation of nitrous oxide. In other words, because the sensible energy from ZPP combustion is introduced to the nitrous oxide-bearing mixture at a finite rate, the initial temperature of the mixture cannot be taken as uniform. In order to account for the transient temperature increase due to heat transfer from the burning ZPP to the nitrous oxide-bearing mixture, an exponential relationship of the following form is suggested:

$$\frac{dE}{dt} = -a * E \qquad (5.13)$$

where:
E is the energy released by ZPP (J)
t is time (ms)
a (the transfer coefficient) is a constant (ms^{-1}).

In order to evaluate Equation (5.13) the transfer coefficient (a) needs to be determined. Recall the mass of solid ZPP decreases by 99.99% in 0.27 ms. Further, the energy of the ZPP particles is transferred primarily via radiation [Gillard, 2002]. Therefore, it can also be assumed that 99.99% of the sensible

energy of the ZPP is released into the nitrous mixture in 0.27 ms. Using this value in solving Equation (5.13) for the transfer coefficient (a) yields a = 32 ms^{-1}.

The expression for the thermal capacity for the nitrous oxide mixture is differentiated with respect to time to yield:

$$\frac{dE}{dt} = N_o Cp_{mix} \frac{dT}{dt} \qquad (5.14)$$

where:

N_o is the initial number of moles of the nitrous oxide-bearing gas mixture

Cp_{mix} is the heat capacity of the nitrous oxide-bearing gas mixture (J/mol/K)

T is the temperature of the nitrous oxide-bearing gas mixture (K)

t is time (ms).

Combining Equations (5.13) and (5.14) and solving for the rate of temperature change of the nitrous oxide mixture yields:

$$\frac{dT}{dt} = \frac{a * E * Exp[-at]}{N_o * Cp_{mix}} \qquad (5.15)$$

Since an expression for the time rate of change of temperature has been derived the model of Turns [Turns, 2000] can be modified to account for the non-homogeneous temperature distribution. Since Equations (5.14) and (5.15) are two ordinary differential equations describing the temperature rise of the system from two different coupled sources; the principle of superposition allows their solutions to be added together to express the overall temperature change of the system:

$$\frac{dT}{dt} = \frac{\frac{\dot{Q}}{V} + R_u \sum_i \left(h_i \dot{\omega}_i\right)}{\sum_i X_i \left(Cp_i - R_u\right)} + \frac{a * E * Exp[-at]}{N_o * Cp_{mix}} \qquad (5.16)$$

A logical check on the applicability of Equation (5.16) is provided through consideration of the functional group (-at). The second term of Equation (5.16) will approach zero when the time is 0.28 ms (the estimated time of complete ZPP combustion), this indicates that the temperature contribution of ZPP to the increase in system temperature is complete.

Equation (5.16) describes the temperature rise rate during the dissociation of nitrous oxide and is the primary equation in the shell model. However, the accuracy of Equation (5.16) is limited to initial densities of the nitrous gas mixture that are approximately 0.0267 g/cm^3.

The applicability of Equation (5.16) to model the dissociation of nitrous oxide is limited to situations in which the pyrotechnic provides sufficient sensible energy to heat the gas to the auto-ignition temperature of nitrous oxide. In the case of pyrotechnically-induced nitrous oxide dissociation, sufficiently high temperature regions exist in close proximity to the reacting pyrotechnic. However, regions far removed from the influence of the pyrotechnic may not be sufficiently heated to result in any appreciable nitrous dissociation.

As the initial gas density of the nitrous oxide is increased, more energy must be supplied from the ZPP to dissociate the nitrous oxide. This suggests that a density limit exists for which Equation (5.16) will no longer accurately approximate the temperature and pressure rise rates during the dissociation of nitrous oxide, because the reaction rate will become infinitesimally small. At the same time this density limit, found to be 0.0267 g/cm^3, is an order of magnitude lower than the highest density case (0.2042 g/cm^3) tested by Rink [Rink, 2009]. To model the dissociation of the nitrous oxide mixture at these high

initial densities, and to simulate the locally high temperature regions surrounding the burning pyrotechnic, the domain is split into smaller volumes, or “shells”. Ultimately the number of shells is dependent upon the initial density of the nitrous oxide-bearing mixture.

5.7. Conclusion of Chapter 5

An analytical model was developed to describe the pyrotechnically-induced dissociation of nitrous oxide in isochoric reactors. The model incorporated a variable number of equal density concentric reactant shells, the number of which was chosen through consideration of their volume in conjunction with energy input from the pyrotechnic.

The results from the model were compared to experimental data. At low initial densities (0.026 g/cm^3) the extent of nitrous oxide dissociation determined experimentally was accurately predicted by using the model with one shell. Therefore, a classical batch reactor model with global first order reaction kinetics, modified to include the rate of energy deposition from a pyrotechnic source, was capable of describing the dissociation of nitrous oxide at low densities. However, at high initial densities (0.026 g/cm^3 to 0.205 g/cm^3) it was found that 20 shells were required to replicate the experimental data. Therefore, the classical batch reactor model with a discretized domain was shown to predict the dissociation of nitrous oxide at high densities. It was further shown, that the analytical value of the extent of reaction converges to experimentally measured values as the number of shells is increased.

The inclusion of more shells into the current model significantly increases its complexity. Therefore, in order to simplify the implementation of the model, it is recommended that the code be modified to incorporate a numerical looping scheme, thereby allowing for a more convenient means of changing the number of shells. In addition, for the high initial density cases the number of shells should be increased in order for the experimentally measured extent of dissociation and the analytically predicted value to converge.

5. Conclusion

An experimental and computational study, consisting of modeling and simulation (M&S), of key thermal-mechanical issues affecting the design and safety of pebble-bed reactors (PBR) was conducted. The objective was to broaden understanding and experimentally validate thermal-mechanic phenomena of nuclear grade graphite, specifically, spheres in frictional contact as anticipated in the bed under reactor relevant pressures and temperatures. The contact generates graphite dust particulates that can subsequently be transported into and circulated in the flowing gaseous (He) coolant. Under postulated depressurization transients and with the potential for leaked fission products to be adsorbed onto graphite ‘dust’, there is the potential for fission products to escape from the primary volume. Furthermore, there is the distinct possibility for the dispersed dust to combust if sufficient conditions are met. The team designed and conducted two separate effects tests to study and benchmark the potential dust-generation rate, as well as study the conditions under which a dust explosion may occur in a standardized, instrumented explosion chamber. The project started August 2009 and concluded September 2013.

As noted, both the PBR’s moving bed reactor core and its online refueling system with extracted graphite fuel pebbles (spheres) eliminates fueling outages both raise safety concerns. Due to frictional contact of pebbles as the bed (slowly) moves, graphite dust is generated and subsequently, its ‘lift-off’ and transport in the primary circuit becomes a safety concerns because graphite dust can be laden with fission products. As the bed contains a large number of pebbles, one anticipates fuel failure from which fission products are released. To understand graphite dust generation, this project custom-designed,

constructed and conducted an experimental study, concurrently M&S, to assess the thermal-mechanics of pebbles leading to dust generation. Additionally, an experimental study on the pyro-mechanics, specifically the pressures produced during the discharge of burning pyrotechnic (graphite dust) into inert gas was investigated. From pressure results, the minimum combustible mass of graphite dust needed during a design basis air ingress accident was estimated.

Thus the project objectives in terms of tasks, as outlined in the proposal were as follows, to:

(1) Design and construct an experimental apparatus to study the thermal-mechanics of graphite spheres in frictional contact during relative motion; that is, the generation of graphite dust as a result of this frictional wear.
(2) Conduct experiments with the apparatus at higher temperatures and (helium) gas pressure of relevance to a PBR
(3) Model and simulate the thermal-mechanics of graphite spheres in frictional contact to be partially verified by experimental data and to estimate the graphite dust generate per reactor year
(4) Experimentally investigate the possibility of graphite dust combustion; that is, the minimum combustible conditions (nominal particulate size, concentration and so forth) and its relation to situations following an air ingress accident in PBRs.

Thus the team designed, constructed and operated a wear testing experimental apparatus and reliably measured the frictional wear generated graphite dust under a range of conditions including at higher temperatures and pressures of relevance to a PBR. The results of wear tests revealed there were two different wear modes for the nuclear grade graphite spheres tested. First at higher temperatures and (helium) pressures as applied, the data yielded what we call “large wear” which was not reported in the past. “Large wear” is distinguished from “lubricated friction” by a degraded surface morphology as a result of the wear test and further SEM/XRD supported data on crystalline structure. “Large wear” results in a higher wear rate and a posteriori estimate of the coefficient of friction. XRD analysis of pre- and post-experiment graphite showed there was a loss of well-organized crystalline structure due to frictional contact under higher pressures and temperature. The graphite dust generated however under “large wear” (and “lubricated wear”) was still small per reactor years as estimated. The lubricate wear results were in good agreement with two previous studies, generally under lower pressures and temperatures.

Computational modeling and simulations were developed in parallel to the experimental study. A phenomenologically-based model explaining experimental results was developed and predicted the key non-linear trend relative to the traditional, linear model. The constants in the proposed analytical wear model were obtained by fitting with the experimental results. Then, the model was used to further predict experimental data. The M&S results revealed that there is approximately 20% difference between the analytical model and the experimental data. However the phenomenological trend agreed well. This difference in magnitude was explained in terms of observations and SEM/XRD data obtained. The model lacked a surface-level lubrication sub-model, thought to be induced by gas adsorption as well as relocation of surface-adhering (dislodged) graphite particulates. Though the former was not experimentally verified, it is our opinion that surface-adhering graphite particulates can function as a ‘lubricant’ and thus limit the graphite dust generate as a result of frictional contact.

Thus the experimental results showed that the wear-generate graphite mass under room to higher temperatures and pressures is small and on the order of grams per reactor year. Finally, dust explosion combustion experiments were performed by Poulsen and Rink to investigate the smallest amount (mass) of graphite dust that can lead to explosions under idealized combustive conditions. Based on

their tests, they estimate that the minimum graphite dust concentration is on the order of 0.0267g/cm^3. This is thus some 220 times more than the dust generated from frictional wear as measured. Thus the pebble-pebble frictional contact is not a plausible source of dust generation and subsequent explosion hazard under normal operating conditions or even accident scenarios.

.

6. References

6.1 List of References for Wear Experiment Task

Archard, J. F.; Hirst, W. (1956) The wear of metals under unlubricated conditions. Proceedings of the Royal Society of London. Series A, *Mathematical and Physical Sciences*, 236(1206), 397-410.

Airgas Inc. 2011 Product Catalog, 27

Antwerpen, W. van, Toit, C.G. du, Rousseau, P.G. (2010) A review of correlations to model the packing structure and effective thermal conductivity in packed beds of mono-sized spherical particles. *Nuclear Engineering and Design*, 240, 1803-1818.

ASME. (2010). *Guidelines for Pressure Boundary Bolted Flange Joint Assembly*. PCC-1 - 2010. ISBN: 9780791832745.

Areva (2010) .*Pebble Bed Reactor Technology Readiness Study*. Technical Data Record Document Number 12-9151714-000.

Baumer, R., Kalinowski, I. (1991) THTR commissioning and operating experience. *Energy*, 16 (1-2), 59-70.

Blau, B.J. (1994) Friction and wear of carbon-graphite materials against metal and ceramic interfaces. *Tribology International,* 27(6), 413-422.

Burchell, T.D. (2008) *Next Generation Nuclear Plant Phenomena Identification and Ranking Tables (PIRTs)*; Volume 5: Graphite PIRT. NUREG/CR-6944, Vol. 5.

China's nuclear fuel cycle. (2011). *World Nuclear Association*, Retrieved from www.world-nuclear.org/info/inf63b_china_nuclearfuelcycle.html

Cogliati, J. J. (2010). *Pebble bed pebble motion: Simulation and applications* (Doctoral dissertation). Pocatello, ID: Idaho State University.

Cogliati ,J., Ougouag, A.M. (2008). *Pebble Bed Dust Production Model*. Proceedings of the International Topical Meeting on High Temperature Reactor Technology HRT2008. Retrieved:www.nextgenerationnuclearplant.com/pressroom/ publications /d/CDocuments_ and_SettingsBenjmlDesktopHTR2008-58289.pdf. 2/2/2012.

Cogliati, J., Ougouag, A.M. (2011). *Pebble-bed pebble motion: simulation and applications*. Idaho National Laboratory technical publication, INL/EXT-11-23047. Retrieved: www.inl.gov/technicalpublications/Documents/5144350.pdf. 2/12/2012.

Cogliati, J., Ougouag, A.M.; Ortensi, J. (2011) Survey of dust production in pebble bed reactor cores. *Nuclear Engineering and Design*, 241, 2364–2369.

Barnert, H., Caspary, G., Fachinger, J., Koster, A., Kummer, A., Makumbe, M., Naicker, L., Seubert, M. (2008). *Examination of dust on AVR pipe components*. Proceedings of the 4th International Topical Meeting on High Temperature Reactor Technology HTR2008, Washington, DC USA.

Fu, Z.-Q., Tang, C.-H., Liang, T.-X., & Li, Z.-Q. (2005) Influence of SiC coating on the tribological behaviors of graphite for high temperature gas-cooled reactor. *Metal Heat Treatment*, 30(9), 13-16.

Gallardo, E. A. (2008) Twin disc assessment of wheel/rail adhesion. *Wear, 265,* 1309-1316.

Garnham, J.E., Davis, C.L. (2008) The role of deformed rail microstructure on rolling contact fatigue initiation. *Wear*, 265 (9-10). 1363-1372. ISSN 0043-1648.

Gouger, H., Ougouag, A.M., Terry, W.K. (2004). *Advanced core design and fuel management for pebble-bed reactors*. Idaho National Engineering and Environmental Laboratory, INEEL/EXT-04-02245. Retrieved: www.inl.gov/technicalpublications/Documents/3310868.pdf., 2/2/2012.

Gottaut,H., Krüger, K. (1990) Results of experiments at the AVR Reactor. *Nuclear Engineering and Design*, 121, 143-153.

Hiruta, M., *Experimental study of dust generation from nuclear grade graphite spheres in frictional contact under a pressurized inert atmosphere at elevated temperatures*, Master's Thesis, University of Idaho, Idaho Falls, ID (2013).

Howe, J., Rawn, C., Jones, L., Ow, H., *Powder Diffraction*, **18**, 159, (2003)

Hokao, M., Hironaka, S., Suda, Y., Tamamoto, Y. (2000) Friction and wear properties of graphite/ glassy carbon composites. *Wear*, 237, p. 54-62.

Houghton, J.E., Mitchell, L.A., Crawford, T.S. (1966). *Effect of Interface geometry on the wear of graphite sliding against stainless steel*. Proceedings of the Institution of Mechanical Engineers, 181(30), 11-15.

Hrovat, M., Grossem K.H. (2006). *Manufacture of high corrosion resistant fuel spheres (FS) for high temperature Pebble Bed Modular Reactors (PBMR).* 3rd International Topical Meeting on High Temperature Reactor Technology. Retrieved: www.nwu.ac.za/htr2006/static-content/downloads/final_download_papers/c/C00000059.pdf., 2/2/2012

Idaho National Laboratory. (2011). *Integration of high temperature gas-cooled reactors into selected industrial process applications*. INL/EXT-11-23008. Retrieved: https://inlportal.inl.gov/portal/server.pt/gateway/PTARGS_0_2_93202_0_0_18/Integration%20of%20High%20Temperature%20Gas-cooled%20Reactors%20into%20Selected%20Industrial%20Process%20Applications.pdf., 2/2/2012

Idaho National Laboratory. (2010). *Module 6d: Pebble bed HTGR refueling design. HTGR Technology Course for the Nuclear Regulatory Commission*. Retrieved: https://inlportal.inl.gov/portal/server.pt/gateway/PTARGS_0_2_74501_0_0_18/Module%206d%20-%20Pebble%20Bed%20HTGR%20Refueling%20Design.pdf., 2/2/2012

Inagaki, M. (1963) Lattice constant and crystalline size measurement method for artificial graphite . *Tanso*, 28-34.

International Atomic Energy Agency. (1997). *Fuel Performance and fission product behaviour in gas cooled reactors*. (IAEA-TECDOC-978). Vienna, Austria. Nuclear Power Technology Development Section.

International Atomic Energy Agency. (2011). *Status report 96 – High Temperature Gas Cooled Reactor – Pebble-Bed Module (HTR-PM)*. Vienna, Austria. Nuclear Power Technology Development Section.

Johnson, G. (2012). *Experimental study of nuclear graphite and graphite-steel wear in spherical frictional contact under gas-cooled reactor pressures and temperatures.* M.S. Thesis. Moscow, ID: University of Idaho.

Kadak, A.C., (2005) A future for nuclear energy: Pebble bed reactors*,* INT. *J.Critical Infrastructures,* 1(4), 330-345.

Kadak, A.C., Zhai, T. (2006) Air ingress benchmarking with computational fluid dynamics analysis*. Journal of Nuclear Engineering and Design*, 236, 587-602.

Kikuchi, K. (1984) Impurity gas effects on friction and wear of high temperature materials for VHTRs. *Nuclear Technology*, 66(2), 491-502.

Kissane, M.P. (2009) A review of radionuclide in the primary system of a very-high-temperature reactor. *Nuclear Engineering and Design*, 239, p. 2076-3091.

Koster, A. (2009, May 29) Pebble bed reactor – safety in perspective. *Nuclear Engineering International,* Retrieved: www.neimagazine.com/story.asp?storyCode=2053102., 2/2/2012

Lancaster, J.K. (1975) Transitions in the friction and wear of carbons and graphite sliding against themselves. *ASLE Trans*., 18(3), 187-201.

Lancaster, J.K. (1980) On the 'dusting' wear regime of graphite sliding against carbon. *J. Phys. D: Appl. Phys*., 13, p. 1551-1564.

Lancaster, J.K., Pritchard, J.R. (1981) The influence of environment and pressure on the transition to dusting wear of graphite. *Journal of Applied Physics*, 14, 747-762.

Li, C.C.; Sheehan, J.E. (1981). *Friction and wear studies of graphite and a carbon-carbon composite in air and in helium*. Proceedings: International conference on wear of materials, San Francisco, CA, USA. Retrieved: www.osti.gov/bridge/purl.cover.jsp?purl=/6676019-E351Uo/., 2/2/2012.

Liao, Y. (2009) *PSI project on HTR graphite dust generation and transport boundary conditions for aerosol transport in the heat transport system and into confinement.* Presentation given at Introduction Meeting on Planned PSI Research on HTR graphite dust issues, Paul Scherer Institute, Villigen, Switzerland. Retrieved from: www.sacre.web.psi.ch/HTR/PSI-Pres/boundary%20conditions.pdf., 2/2/2012

Lind, T. (2009). *Graphite aerosol generation: causes and unknown.* Presentation given at Introduction Meeting on Planned PSI Research on HTR graphite dust issues, Paul Scherer Institute, Villigen, Switzerland. Retrieved from www.sacre.web.psi.ch/HTR/PSI-Pres/Lind_dust_generation_191109.pdf., 2/2/2012

Lohnert, G.H., 1990, Technical design features and essential safety-related properties of the HTR-MODULE", *Nuclear Engineering and Design*, 121, 259-275.

Luo, X., Li, X., Yu, S. (2010) Nuclear graphite friction properties and the influence of friction properties on the pebble bed. *Nuclear Engineering and Design*, 240, 2674-2681.

Luo, X., Yu, S., Sheng, X., He, S. (2005). Temperature effect on IG-11 graphite wear performance. Nuclear *Engineering and Design*, 235, p. 2261-2274.

Luo, X., Yu, S., Xuanyu, S., Shuyan, H. (2006). The influence of roughness on tribological properties of nuclear grade graphite*. Journal of Nuclear Materials*, 350, 74-82.

Luo, X., Zhang, L.; Sutuan, Y. (2004). The wear properties of nuclear grade IG-11 under different loads, *International Journal of Nuclear Energy Science and Technology,* 1(1), 33-43.

Mehner, A.W., Heit, W., K. Röllig, Ragoss, K., Müller, H. (1990) Spherical Fuel Elements for advanced HTR manufacture and qualification by irradiation testing. *Journal of Nuclear Materials*, 171, 9-18.

Miller, G.K., Petti, D. A., and Maki, J. T. (2002) *Development of an integrated performance model for triso-coated gas reactor particle fuel.* High Temperature Reactor 2002 Conference, April 2002. Retrieved: www.inl.gov/technicalpublications/Documents/3169759.pdf. Chicago, Illinois, April 25-29, 2004, on CD-ROM, American Nuclear Society, Lagrange Park, IL.

Miyake, M. (1996)*. Introductory carbon material*. Tokyo, Japan: Realice Inc.,

Moormann, R. (2006) *Phenomology of graphite burning in massive air ingress accidents.* 3rd International Topical Meeting on High Temperature Reactor Technology. Retrieved: www.nwu.ac.za/htr2006/static-content/downloads/final_download_papers/f/F00000032.pdf., 2/12/2012

Moormann, R. (2008) Fission Product Transport and Source Terms in HTRs: Experience from AVR Pebble Bed Reactor. *Science and Technology of Nuclear Installations.* Vol. 2008, Article ID 597491.

Nabielek, et al. (1984) Fuel for Pebble-Bed HTGRs. *Nuclear Engineering and Design*, 78, 155-166.

NEUP proposal abstract. (2009, October). Retrieved August 5, 2013, from NEUP website: http://inlimages.inl.gov/imageserver/NEUP/docs/FY%202009%20RD%20Abstracts/Gen%20IV//NEUP_09-151_abstract.pdf

PBMR (Pty) Ltd. (2005) *General Overview of the Pebble Bed Modular Reactor*. 0311865rev(1).

Petti, D. (2013, May). *Current status of high temperature gas-cooled reactor activities in the united states.* Paper presented at VHTR R&D FY13 Technical Review Meeting, Idaho Falls, ID.

Poulsen, B. (2011). *Prediction of isochoric inert and reactive gas behavior during pyrotechnic initiator actuation.* (Doctoral dissertation). Moscow, ID: University of Idaho.

Powers, D. A., Trip Report, Travel by D. A. Powers to attend the High-Temperature Gas-Cooled Reactor Safety and Research Issues Workshop, Rockville, MD, Oct. 10-12, 2001 As of 12/03/08, at URL: www.nrc.gov/reactors/new-licening/new-licensing-files/ml020450645.pd

Qiu Xueliang, He Jun, Guo Guiju, Zuo Kaifer, & Zhang Shuangxi (1996) "*Development of the graphite matrix materials of the fuel elements for the 10 MW HTR test module "(IAEA-TECDOC--901).* International Atomic Energy Agency *(IAEA).* Retrieved: www.iaea.org/inis/collection/NCLCollectionStore/_Public/28/008/28008827.pdf., 2/2/2012.

Robert, F., Paulmier, D., Zaïdi, H., Schouller, E. (1995). Combined influence of inert gas environment and a mechanical action on a graphite surface. *Wear*, 181-183, 687-690.

Rostamian, M., Arifeen Sh., Potirniche P. G., Tokuhiro A. (2010). Initial analysis of pebble contact in pebble bed reactors. *Transactions of the American Nuclear Society*, 103, 1028-1031.

Rostamian, M., Arifeen Sh. Potirniche P. G., Tokuhiro A. (2011), Initial prediction of dust production in pebble bed reactors, *Journal o f Mechanical Sciences*, 2 189-195.

Rostamian, M., Potirniche P. G., Cogliati J. J., Ougouag A. M., Tokuhiro A. (2012), Computational prediction o f dust production in pebble bed reactors, *Nuclear Engineering and Design*, 243, 33-40.

Rostamian, M. (2012). *Computational prediction of dust production in graphite moderated pebble bed reactors*. Doctoral dissertation. Moscow, ID: University of Idaho.

Röllig, K. (1990) *Behaviour* of gas cooled reactor fuel under accident conditions. *Proceedings of a specialists meeting held in Oak Ridge, 5-8 November 1990. International Atomic Energy Agency*, Vienna (Austria). International Working Group on Gas-Cooled Reactors. IWGGCR, 25, 99-108.

Savage, R. (1948) Graphite Lubrication. *Journal of Applied Physics*, 19(1), 1-10.

Savage, R., Schaefer, D.L. (1955) Vapor Lubrication of Graphite Sliding Contacts, *Journal of Applied Physics*, 27 (2), 136-138.

Schlögl, B. (2009). Graphite Dust in AVR*, Presentation given at Introduction Meeting on Planned PSI Research on HTR graphite dust issues,* Paul Scherer Institute, Villigen, Switzerland. Retrieved: www.sacre.web.psi.ch/HTR/Part-Pres/Graphite%20Dust%20in%20AVR%20-%20PSI.pdf. , 2/2/2012

Sheng, X., Yu, S., Lou, X., S., He. (2003) Wear behavior of graphite studies in an air-conditioned environment *Nuclear Engineering and Design*, 223, 109-115.

Stansfield, O.M. (1969). Friction and wear of graphite in dry helium at 25, 400, and 800°C, *Nuclear Applications*, 6, 313-320.

Vasica, G.; Franklina,F. J.; Fletcher, D.I. (2010) Influence of partial slip and direction of traction on wear rate in wheel-rail contact, *Wear*, 270 (3-4), 163-171.

von der Decken, C.B. (1972) Mechanical Problems of a Pebble Reactor Core, *Nuclear Engineering and Design*, 18, 323-333.

Wagner, P. and Driesner, A.R. (1957) *The friction coefficients of graphite at extreme temperatures*, Los Alamos Scientific Laboratory Report LA-2146.

Wolf, L., Ballensiefen, G., Fröhling, W. (1975) Fuel elements of the high temperature pebble bed reactor, *Nuclear Engineering and Design*, 34, 93-108.

Wu Zongxin, , Dengcai, L., Daxin, Z. (2002) The design features of the HTR-10, *Nuclear Engineering and Design*, 218, 25-32.

Yen, B.K., Ishihara, T., Yamamoto, I. (1997) "Influence of environment and temperature on ''dusting'' wear transitions of carbon–carbon composites, *Journal of Material Science*, 32, 681-686.

Zaïdai, H., Robert, F., Paulmier, D., Néry, H. (1993) Correlation between the tribological behavior of graphite and its mechanical properties versus the inter-plane distance. *Applied Surface Science*, 70/71, 103-108.

Zaïdi, H, Paulmier, Lepage, J. (1990) The influence of the environment on the friction and wear of graphitic carbons: Part II. Gas coverage of wear debris, *Applied Surface Science*, 44, 221-233.

Zaïdi, H., Robert, F., Paulmier, D. (1995) Influence of adsorbed gases on the surface energy of graphite: consequences on friction behavior, *Thin Solid Films*, 264, 46-51.

Zhang, Z., Wu, Z., Wang, D., Xu, Y., Sun, ZY., Li, F., Dong, Y. (2009). Current status and technical description of Chinese 2 x250 MW_{th} HTR-PM demonstration plant, *Nuclear Engineering and Design*, 239, 1212-1219.

Zhao, H., Liang, T., Zhang, J., He, J., Zou. Y., Chunhe, T. (2006) Manufacture and characteristics of spherical fuel elements for HTR-10, *Nuclear Engineering and Design*, 236, 643-647.

Zhi-qiang, Fu; et. al. (2005) Influence of SiC coatings on tribological behavior of graphite for high temperature gas cooled reactor, *Institute of Nuclear Energy,* Tsinghua University, Beijing 100084,China. Retrieved: www.en.cnki.com.cn/Article_en/CJFDTOTAL-JSRC200509003.htm., 2/2/2012.

6.2 List of References for Computational Prediction Task

ABAQUS FEA v6.11, SIMULIA web site, Dassault Systèmes, www.simulia.com visited March, 2010 through October, 2012.

Albers T. L. (2009), High-Temperature Properties of Nuclear Graphite, Journal of Engineering for Gas Turbines and Power, 131 (6) 064501-1,2.

Archard J. F., Hirst W. (1956), The Wear of Materials under unlubricated Conditions, Proceedings of the Royal Society A-236 397-410.

Barlow, J. (1976), Optimal Stress Locations in Finite Element Models, International Journal for Numerical Methods in Engineering, 10 243–251.

Basini V., Bruguier F., Cellier F., Vitali M. P. (2006), Selection Criteria for Choosing Carbonaceous Matrix for HTR Block Type Design, HTR 2006, 3rd International Topical Meeting on High Temperature Reactor Technology.

Baxter A., Ellis, C. (2007), Preconceptual Engineering Services for the Next Generation Nuclear Plant (NGNP) with Hydrogen Production, NGNP Reactor Type Comparison Study, Prepared by General Atomics For the Battelle Energy Alliance, LLC.

Belytschko T., Black T. (1999), Elastic Crack Growth in Finite Elements with Minimal Remeshing, International Journal for Numerical Methods in Engineering, 45 (5) 601-620.

Berthe D., Dowson D., Godet M., Taylor C.M. (1989), Tribological Design of Machine Elements, Proceedings of the 15th Leeds-Lyon Symposium on Tribology, UK.

Bhushan B. (2000), Modern Tribology Handbook, CRC Press, Florida, USA.

Blau P. J. (1992), ASM Handbook Volume 18: Friction, Lubrication, and Wear Technology.

Burchell T. D. (1999), Carbon materials for advanced technologies, University of Virginia, Elsevier Ltd.

Burnham N. A., Kulik A. J. (1997), Surface Forces and Adhesion, Handbook of Micro/Nanotribology.

Cannon P. (1964), Mechanism of the Vapor Lubrication of Graphite, Joural of Applied Physics 35 2928-2929.

Carré F., Yvon P., Lee W. J., Dong Y., Tachibana Y., Petti D. (2009), VHTR – ONGOING INTERNATIONAL PROJECTS, GIF Symposium, France 9-10.

Cogliati J. J. , Ougouag A. M. (2008), Pebble Bed Reactor Dust Production Model, Proceedings of the 4th International Topical Meeting on High Temperature Reactor Technology, Washington, D. C., USA.

Cogliati J. J., Ougouag A. M. (2010), Dust Production Model for HTR-10.

Cogliati J. J., Ougouag A. M., Ortensi J. (2011), Survey of dust production in pebble bed reactor cores, Nuclear Engineering and Design, 241 (6) 2364-2369.

Cogliati J. J., Ougouag A. M. (2011), Pebble-Bed Pebble Motion: Simulation and Applications, Prepared for the U.S. Department of Energy Office of Nuclear Energy Under DOE Idaho Operations Office Contract DE-AC07-05ID14517.

Cox B. (1990), Pellet Clad Interaction (PCI) Failures of Zirconium Alloy Fuel Cladding–A Review, Journal of Nuclear Materials, 172 249–292.

Czichos H. (1978), Tribology: A System Approach to the Science and Technology of Friction, Lubrication and Wear, Elsevier Scientific Publishing Company.

du Toit C. G., van Antwerpen W., Rousseau P. G. (2009), Analysis of the Porous Structure of an Annular Pebble Bed Reactor, International Congress on Advances in Nuclear Power Plants (ICAPP'09), Shinjuku, Japan.

Engle G. B. (1974), Status of Graphite Technology and Requirements for HTGRs, American Nuclear Society Topical Meeting on HTGRs, Gatlinburg, Tennessee.

Eto M., Oku T., Konishi T. (1991), High Temperature Young's Modulus of a Fine-Grained Nuclear Graphite Oxidized or Prestressed to Various Levels, Carbon 29 (1) 11-21.

Evans A. G. (1980), Fatigue in Ceramics, International Journal of Fracture, 16 485-498.

Fachinger J. (2008) Examination of Dust on AVR Pipe Components, Proceedings of the 4th International Topical Meeting on High Temperature Reactor Technology HTR2008, Washington, D.C., USA.

Faulkner A., Arnell R. D. (2000), The Development of a Finite Element Model to Simulate the Sliding Interaction between Two, Three-Dimensional, Elastoplastic, Hemispherical Asperities, Wear 242 114–122.

Feneberger K. (1973), GRAPHITE: SOLID LUBRICANT, Industrial Lubrication and Tribology, 25 (5) 176 - 178.

Fu Z. (2005), Influence of SiC Coatings on Tribological Behavior of Graphite for High Temperature Gas-cooled Reactor. Institute of Nuclear Energy, Tsinghua University, Beijing, China.

Gougar, H. (2006), The Application of the PEBBLE Code Suite to the PBMR-400 Coupled Code Benchmark–FY 2006 Annual Report.

Greenstreet W. L. (1968), Mechanical Properties of Artificial Graphite - A Survey Report, Oak Ridge National Laboratory, Tennessee, USA.

Grigor'ev O. N. , Trefilov V. I., Shatokhin A. M. (1983), Influence of Temperature on the Failure of Brittle Materials in Concentrated Loading, Powder Metallurgy And Metal Ceramics 22 (12), 1028-1033.

Heard P.J., Wootton M.R., Moskovic R. Flewitt P.E.J. (2010), Crack initiation and propagation in pile grade A (PGA) reactor core graphite under a range of loading conditions, Journal of Nuclear Materials 401 71–77.

Ho F. H., Graphite Design Handbook, General Atomics, Department of Energy, DE-AC03-88SF17367.

Hrovat M., Grossem K. H. (2006), Manufacture of High Corrosion Resistant Fuel Spheres (FS) for High Temperature Pebble Bed Modular Reactors (PBMR), 3rd International Topical Meeting on High Temperature Reactor Technology.

HTGR Technology course for the Nuclear Regulatory Commission-Module 6d, 2010.

IAEA (2003), Evaluation of High Temperature Gas Cooled Reactor Performance: Benchmark Analysis Related to Initial Testing of the HTTR and HTR-10, IAEA-TECDOC-1382.

IAEA TECDOC 1249 (2009), Critical Experiments and Reactor Physics Calculations for Low-Enriched High Temperature Gas Cooled Reactors.

Ishiyama S. (1996), The Effect of High Fluence Neutron Irradiation on the Properties of a Fine-Grained Isotropic Nuclear Graphite, Int'l Journal of Nuclear Materials, 230 1-7.

Jenkins G. M. (1962), Analysis of the Stress-Strain Relationships in Reactor Grade Graphite, British Journal of Applied Physics 13 30-32

Johnson W. R., Engle G. B. (1976), "Properties of Unirradiated Fuel Element Graphites H-451 and TS-1240," ERDA Report GA-A13752.

Johnson, G. (2012), Experimental Study of Nuclear Graphite and Graphite-Steel Wear in Spherical Frictional Contact under Gas-Cooled Reactor Pressures and Temperatures, MS Thesis, Dept. of Mechanical Engineering, University of Idaho.

Joyce M. R. (2008), Observation of Microstructure Deformation and Damage in Nuclear Graphite, Engineering Fracture Mechanics 75 3633–3645.

JUN J. S., LIM H. S., LEE W. J. (2008), The Benchmark Calculations of the Gamma+ Code with the HTR-10 Safety Demonstration Experiments, Korea Atomic Energy Research Institute, 305-600.

Kadak A. C. (2004), Pebble Flow Experiments for Pebble Bed Reactors, High Temperature Reactor.

Kim E. S. (2007), Estimation of Graphite Density and Mechanical Strength of VHTR during Air-Ingress Accident, NURETH-12.

Kim E. S., Kim Y. W. (2010), Friction Coefficients Of Nuclear Grade Graphites For Very High Temperature Gas-cooled Reactor At Room Temperature, Nuclear Hydrogen Reactor Technology Division, Korea, Atomic Energy Research Institute, 305-353, Korea.

Kim J., Kang Y. H., Choi H. H., Hwang S. M., Kang B. S. (2002), Comparison of Implicit and Explicit Finite-Element Methods for the Hydroforming Process of an Automobile Lower Arm, International Journal of Advanced Manufacturing Technology, 20 (6) 407–413.

Kissane M. P. (2009), A Review of Radionuclide in the Primary System of a Very-High-Temperature Reactor, Nuclear Engineering and Design, 239 2076-3091.

Konishi T., Eto M., Oku T. (1986), High Temperature Young's Modulus of IG-110 Graphite. International Atomic Energy Agency, Vienna (Austria). International Working Group on Gas-Cooled Reactors, IWGGCR-11 133-137.

Koster A. (2009), Pebble Bed Reactor-Safety in Perspective, Nuclear Engineering International. Retrieved: www.neimagazine.com/story.asp?storyCode=2053102.

Kurumada A., Oku T. (1994), Influence of Burn-off on Strength and Toughness of Carbon Materials, Journal of the Faculty of Engineering, Ibaraki University, 42 45-55.

Lancaster J. K. (1975), Instabilities in the Frictional Behavior of Carbons and Graphite, Wear, 34 275-290.

Lancaster J. K. (1980), On the 'Dusting' Wear Regime of Graphite Sliding against Carbon, Journal of Physics D: Applied Physics, 13 1551-1564.

Lancaster, J. K., Pritchard, J. R. (1981), The Influence of Environment and Pressure on the Transition to Dusting Wear of Graphite. Journal of Applied Physics, 14 747-762.

Lemaitre J., Desmorat R. (2005), Engineering Damage Mechanics, Springer.

Lind, T. (2009). Graphite Aerosol Generation: Causes and Unknown, Introduction Meeting on Planned PSI Research On HTR Graphite Dust Issues, Paul Scherer Institute, Villigen, Switzerland.

Losty H. W., J. S. Orchard (1962), The Strength of Graphite, Proceedings of the 5th Conference on Carbon, MacMillan, New York, 519532.

Lou X., Suyaun Y., Zhen-sheng Z. , Shu-yan H. (2005), Estimation of Graphite Dust Quantity and Size Distribution of Graphite Particle in HTR-10, Nuclear Power Engineering 26 258-266.

Maruyama T. (1987), Elastic Modulus and Bend Strength of a Nuclear Graphite at High Temperature, Carbon 25 (6) 723-726.

Mitchell B. C. (2003), The Mechanical Testing of Nuclear Graphite, Int'l Journal of Nuclear Materials 322 126–137.

Moormann R. (2009), A Safety Re-Evaluation of the AVR Pebble Bed Reactor Operation and its Consequences for Future HTR Concepts, JUEL-4275.

NEUP-09151 (2009), Nuclear Engineering University Programs Research and Development, Experimental Study and Computational Simulations of Key Pebble Bed Thermomechanics Issues for Design and Safety.

Nelson L., Gandrik A., McKellar M., Patterson M., Robertson E. (2011), R. Wood, Integration of High Temperature Gas-Cooled Reactors into Selected Industrial Process Applications, Idaho National Laboratory Next Generation Nuclear Plant Project, Prepared for the U.S. Department of Energy Office of Nuclear Energy.

Next Generation Nuclear Plant Phenomena Identification and Ranking Tables (NGNP-PIRTs) (2008) (5) Graphite PIRTs.

Nuclear Regulatory Commission (2002), Advisory Committee on Reactor Safeguards Subcommittee on Future Plant Design [Advanced Reactor Designs], Rockville, Maryland, USA.

Oku T. (1993), Relation between Static and Dynamic Young's Modulus of Nuclear Graphite and Carbon, Nuclear Engineering and Design 143 239-243.

Peng W., Yang X., Wang J., Yu S. (2012), Preliminary Study of Graphite Dust Deposition in Steam Generator of HTR-10, Particuology, In Press.

Play D., Godet M. (1977), Self-Protection of High Wear Materials, American Society of Lubrication Engineers, 22 (1) 56-64.

Poulsen, B., Rink, K. K. (2010), Modeling the Energy Release Characteristics of THPP-Based Initiators. Proceedings of 48th AIAA Aerospace Sciences Meeting, American Institute of Aeronautics and Astronautics, Orlando, FL.

Poulsen B. (2011), prediction of isochoric Inert and Reactive Gas Behavior during Pyrotechnic Initiator Actuation, PhD Thesis, University of Idaho.

Ritchie R. O. (1990), Cyclic Fatigue-Crack Propagation, Stress-Corrosion, and Fracture-Toughness Behavior in Pyrolytic Carbon-Coated Graphite for Prosthetic Heart Valve Applications, Journal of Biomedical Materials Research, 24 189-206.

Robert F., Paulmier D., Zaïdi H, Schouller E. (1995), Combined Influence of an Inert Gas Environment and a Mechanical Action on a Graphite Surface, Wear 181–183 (2) 687-690.

Rollins F. R. (1961), Use of Graphite Whiskers in a Study of the Atmosphere Dependence of Graphite Friction, Journal of Applied Physics, 32 (8) 1454-1458.

Roselman I. C., Tabor D. (1976), The friction of Carbon Fibers, Journal of Physics D: Applied Physics 9 (17) 2517.

Rostamian M., Arifeen Sh., Potirniche P. G., Tokuhiro A. (2010), Initial Analysis of Pebble Contact in Pebble Bed Reactors, Transactions of the American Nuclear Society, 103 1028-1031.

Rostamian M., Arifeen Sh., Potirniche P. G., Tokuhiro A. (2011), Initial prediction of dust production in pebble bed reactors, Journal of Mechanical Sciences, 2 189-195.

Rostamian M., Potirniche P. G., Cogliati J. J., Ougouag A. M., Tokuhiro A. (2012), Computational prediction of dust production in pebble bed reactors, Nuclear Engineering and Design, 243, 33-40.

Rostamian M., Potirniche P. G., Ougouag A. M., Cogliati J. J., Tokuhiro A. (2012), Computational and Experimental Prediction of Dust Production in Pebble Bed Reactors, Part I, Nuclear Engineering and Design, Submitted.

Rostamian M., Potirniche P. G., Ougouag A. M., Cogliati J. J., Tokuhiro A. (2012), Computational and Experimental Prediction of Dust Production in Pebble Bed Reactors, Part II, Nuclear Engineering and Design, Submitted.

Rycroft C., Grest G. S., Landry J. W., Bazant M. Z. (2006), Analysis of Granular Flow in a Pebble-Bed Nuclear Reactor, Physical Review E, 74 1-18.

Schlögl B. (2009). Graphite Dust in AVR. Introduction Meeting on Planned PSI Research on HTR Graphite Dust Issues, Paul Scherer Institute, Villigen, Switzerland.

Schroeder B., Schenk W., Alkan Z., Conrad R. (1998), Ceramic Coatings for HTR Graphite Structures: Tests and Experiments with SiC-Coated Graphite Specified. KERNTECHNIK 63 (3) 98-106.

Seldin E. J., Nezbeda C. W. (1970), Elastic Constants and Electron-Microscope Observations of Neutron-Irradiated Compression-Annealed Pyrolytic and Single-Crystal Graphite, Journal of Applied Physics 41 3389-3400.

Sheng X. , Yu S., Luo X., He S. (2003), Wear behavior of graphite studies in an air-conditioned environment, Nuclear Engineering and Design, 223 109–115.

Shibata T. (2008), Non-Destructive Evaluation Methods for Degradation of IG-110 and IG-430 Graphite, Int'l Journal of Nuclear Materials 381 165–170.

Skinner J. (1971) PhD Dissertation, University of Cambridge, Cambridge, UK.

Smith M. C. (1964), Effects of temperature and strain rate on transverse tensile properties of H4LM graphite tested in helium and in vacuum, Carbon 1 (2) 147–152.

Stansfield O. M. (1969), Friction and Wear of Graphite in Dry Helium at 25, 400, and 800 Degrees C, Nuclear Applications 6 313-320.

Stempniewicz M. M., Winters L., Caspersson S. A. (2012), Analysis of dust and fission products in a pebble bed NGNP. Nuclear Engineering and Design 251 433-442.

Swank D., Lord J., Rohrbaugh D. Windes W. (2010), AGC-2 Graphite Pre-irradiation Data Package, INL Report, August 2010.
Terry W. K. (2001), Modular Pebble-bed Reactor Project, INEEL/EXT-01-01623, 46-47, INEEL and MIT.
Tokuhiro A. (2010), Private Communication, Draft submitted to Nuclear Regulatory Commission: Jolicoeur J., Bajorek S., Tokuhiro A. (2008), Knowledge base needs and gaps on graphite dust transport and interaction with fission products of a MHTGR.
Toyo Tanso USA, Inc.: Grade IG–11, EDM Isotropic Graphite, Special Graphite and Compound Materials Products.
Tsang D. K. L. (2007), Effects of Dimensional Change Strain in Nuclear Graphite Component Stress Analysis, Nuclear Engineering and Design 237 897–904.
Venter P. J. (2005), PBMR Reactor Design and Development, SMiRT (18) (2005) 4452-4466.
Virgil'ev Y. S. (2007), Graphite for The GT-MGR High-Temperature Gas-Cooled Reactor, Atomic Energy, 103 (4) 780-782.
Warren B. E. (1990), X-Ray Diffraction, Dover Publications, Inc. Mineola, N.Y., U.S.
Weil J. (2001), Pebble Bed Design Returns. IEEE Spectrum, 37–40.
Wolf L., Ballensiefen G., Fröhling W. (1975), Fuel Elements of The High Temperature Pebble Bed Reactor, Nuclear Engineering and Design, 34, 93-108.
Wu Z., Lin D., Zhong D. (2002), The Design Features of the HTR-10. Nuclear Engineering and Design, 218 25-32.
Xueliang Q., He J., Guo G., Zuo K., Zhang S. (1996), Development of the Graphite Matrix Materials of the Fuel Elements for the 10MW HTR Test, Int'l Atomic Energy Agency (IAEA).
Yen B. K., Ishihara T. (1996), On Temperature-Dependent Tribological Regimes and Oxidation of Carbon-Carbon Composites up to 1800°C, Wear 196 254-262.
Yoda S. Eto M. (1983), The Tensile Deformation Behavior of Nuclear Grade Isotropic Graphite Posterior to Hydrostatic Loading, In't Journal of Nuclear Materials, 118 (2-3) 214-219.
Yokoyama T. (2008), Compressive Stress-Strain Characteristics of Nuclear-Grade Graphite IG-11: Effects of Specimen Size and Strain Rate, Transactions of the Atomic Energy Society of Japan, 7 (1) 66-73.
Zhang Z., Wu Z., Wang D., Xu Y., Sun Z., Li F., Dong Y. (2009), Current Status and Technical Description of Chinese 2x250 MWt HTR-PM Demonstration Plant. Nuclear Engineering and Design, 239 1212-1219.
Zhao H., Liang T., Zhang J., He J., Zou Y., Chunhe T. (2006), Manufacture and Characteristics of Spherical Fuel Elements for HTR-10, Nuclear Engineering and Design, 236 643-647.

6.3 List of References for Combustion Prediction Task

Air Bag Inflation Gas Generation via a Decomposing Material, U.S. Patent 5,669,629 September 23, 1997.
Allen, M. T., Yetter, R. A., Dryer, F. L., "The Decomposition of Nitrous Oxide at $1.5 \leq P \leq 10.5$ Atm and $1103 \leq T \leq 1173$ K," International Journal of Chemical Kinetics, Vol. 27, pp. 883-909, 1995.
Bell, T. N., Robinson, P. L., Trenwith, A. B., "The Thermal Decomposition of Nitrous Oxide. The Effect of Foreign Molecules," Journal of Chemical Society, pp. 1474-1480, 1957.
Belyaev, A. F., Bobolev, V. K., Korotkov, A. I., Sulimov, A. A., Chuiko, S. V., "Transition from Deflagration to Detonation in Condensed Phases," edited by P. Greenberg, Keter Publishing, Jerusalem, 1975.
Berger, B., "Parameters Influencing the Pyrotechnic Reaction," Propellants, Explosives, Pyrotechnics, No. 1, 30, 2005.
Davenport, D. E., "Temperature coefficient of Resistivity Effects on 1A/1W NO-Fire initiators," Proceedings of the 5th Symposium On Electroexplosive Devices, Philadelphia, PA., June 1967.
DuBuisson, A. C., "Design and Fabrication of Closed Vessels For Ballistic Testing," Master's Thesis, University of Idaho Department of Mechanical Engineering. June, 2005.

Fogler, S. H., "Elements of Chemical Reaction Engineering," 4th ed., Upper Saddle River, NJ, 2006.
Forman, D., "Automotive Initiator Technology," 35th AIAA/ASME/SAE/ASEE Joint
Gill, K. E., Laidler, J. K., "Theoretical Aspects of the Unimolecular Decomposition of Nitrous Oxide," Journal of Chemistry Vol. 36, 1958.
Propulsion Conference and Exhibit, AIAA, Washington DC, 1999.
Gardiner, W. C., Olson, D. B., "Chemical Kinetics of High Temperature Combustion," Journal of Physical Chemistry Vol. 21, pp. 377-399, 1980.
Gillard, P., Roux, M., "Study of the Radiation Emitted During the Combustion of Pyrotechnic Charges. Part I: Non Stationary Measurement of the Temperature by Means of a Two-Color Pyrometer," Propellants, Explosives, Pyrotechnics Vol. 27, pp. 72-79, 2002.
Gordon, G. S., McBride, B. J., NASA RP-1311, Oct. 1994.
Green, D. J., Johnson, M. S., Richardson, W. B., Rink, K. K. "P-v-T Behavior of Non-Ideal, Multi-Component Gas Mixtures Used for Automotive Airbag Inflator Applications," proceedings of the Western States Section of the Combustion Institute 2002 spring meeting, San Diego, California, March 25-26, 2002.Kinney, G. F., "Explosive Shocks in Air," Springer publications, Verlag, N. Y., 1985.
Green, D. J., Johnson, M. S., Richardson, W. B., Rink, K. K., "An Experimental Apparatus for Determination of the Energy Released during Combustion of Pyrotechnic Initiators Used for Automotive Airbag Applications," proceedings of the Western States Section of the Combustion Institute 2002 spring meeting, San Diego, California, March 25-26, 2002.
Gunter, D. V., "Instrument of a Closed Vessel Ballistic Test Fixture for the Determination of Apparent Energy Release by Pyrotechnic Initiators," Master's Thesis, University of Idaho Department of Mechanical Engineering. August, 2004.
Helmy, A. K., "Prediction of Arrhenius Kinetic constants for Zirconium Potassium Perchlorate," International Annual Conference- Fraunhofer Institut Fur Chemische Technologie, Conference 35, 2004.
Hohman, C., Tipton, B. Jr., Dutton, M., "Propellant for the NASA Standard Initiator," Lyndon B. Johnson Space Center, Houston, Texas 77058, Oct., 2000. Kent, R., "Air Bag Development and Performance New Perspectives from Industry, Government and Academia", 2003.
Hunter, E., "The Thermal Decomposition of Nitrous Oxide at Pressures up to Forty Atmospheres," Proceedings of the Royal Society, Vol. 144, pg 386, 1934.
Johnston, H., "Interpretation of the Data on the Thermal Decomposition of Nitrous Oxide," The Journal of Chemical Physics Vol. 19, No. 6, June 1951.
Kalbak, W. M., Sliepcavich, C. M., "Kinetics of Decomposition of Nitrous Oxide," Reviewed Feb. 28, 1977, Accepted Feb. 16, 1978. Presented at the Division of Industrial and Engineering Chemistry, 173rd National Meeting of the American Chemical Society, New Orleans, La, March 1977.
Kaufman, F., Gerri, J. N., Bowman, E. R., "Role of Nitric Oxide in the Thermal Decomposition of Nitrous Oxide," the Journal of Chemical Physics Vol. 25, No. 1, July 1956.
Krisjansons, J., Bollinger, L. E., Edse, R., "Explosion Limit Studies of Nitrous Oxide and Nitrous Oxide-Nitrogen-Air Mixtures to 200 atm and 1800 R," Sept. 1962.
Lee, J. S., Lin, L. K., Lin, C. H., Chen, P. J., Huang, C. W., Chang, S. S., "A Study of Zirconium/Potassium Perchlorate Primer Mixtures," Thermochimica Acta, Vol. 173, pp. 211-218, 1990.
Lewis, R. M., Hinshelwood, C. N., "The Thermal Decomposition of Nitrous Oxide," Nov. 25, 1938.
Li, J., Zhao, Z., Kazakov, A., Dreyer, F., "An Updated Comprehensive Kinetic Model of Hydrogen Combustion," Department of Mechanical and Aerospace Engineering, Princeton University, Princeton NJ, Published online in Wiley InterScience, Received 8 Jan. 2004, revised 2 May 2004, accepted 11 May 2004.
Lindars, F. J., Hinshelwood, C., "The Thermal Decomposition of Nitrous Oxide II. Influence of Added Gases and a Theory of the Kinetic Mechanism," Proceedings of the Royal Society, London, 1955.

NIST chemical web book, available online at: http://webbook.nist.gov/chemistry/, Last checked April 10, 2009.

Nyer, B. T., "Bridgewire Heating," Proceedings of the 16th Explosives and Pyrotechnics Conference, Philadelphia, PA, April, 1997.

Richardson, W. B., Rink, K. K., "Dissociation of Nitrous Oxide in High Pressure Environments Using ZPP and THPP Based Pyrotechnic Initiators," Proceedings of the Third Joint Meeting of the U.S. Sections of The Combustion Institute.

Richardson, W. B., Rink K. K., "The Thermally-Induced Decomposition of High Pressure Nitrous Oxide, Argon, and Helium Mixtures in a Closed Vessel," proceedings of the 19th International Colloquium on the Dynamics of Explosions and Reactive Systems, Hakone, Japan, July 27-August 1, 2003.

Rink, K. K., Unpublished Data, University of Idaho, 2009.

Rink, K. K., "Fundamental Considerations Concerning the Detection of Gross Leaks in Bridge-Wire Initiators," International Journal of Vehicle Safety, Vol. 1, No. 4, pp. 253-266, 2006.

Sirdeshpande, A. R., Ierapetritou, M., Androulakis, I., "Design of Flexible Reduced kinetic Mechanisms," AIChE Journal, Vol. 47, No. 11, Nov. 2001.

Smith, J. M., Van Ness, H. C., Abbott, M. M., "Introduction to Chemical Engineering Thermodynamics," 7th ed., New York, New York, 2005.

Sonntag, R. E., Borgakke, C., "Introduction to Engineering Thermodynamics," John Wiley & Sons Inc., 2001.

Thompson, L. M., Maughan, M. R., Rink, K. K., Blackketter, D. M., Stephens, R. R., "Thermally Induced Stresses in Bridge-Wire Initiator Glass-to-Metal Seals," Journal of Electronic Packaging, Vol. 129, pp. 300-306, September 2007.

Turns, R. S., "An Introduction to Combustion Concepts and Applications," 2nd ed., McGraw-Hill, 2000.

USCAR 24 "Inflator Technical Requirements and Validation," Society of Automotive Engineers, June 2004USCAR "Initiator Technical Requirements and Validation," Society of Automotive Engineers, June 2004.

Welty, J. R., Wicks, C. E., Wilson, R. E., Rorrer, G., "Fundamentals of Momentum, Heat, and Mass Transfer," 4th ed., New York, NY, 2001

Williams, F. A., "Reduced Kinetic Schemes in Combustion" Ch 4. Propulsion Combustion: Fuels to Emissions, pp. 93-128, Washington DC, 1998.

Williams, F. A., "Detailed and Reduced Chemistry for Hydrogen Autoignition", Journal of Loss Prevention in the Process Industries, Vol. 21, pp. 131-135, 2008.